THERMOSCIENCES DIVISION

MECHANISMS OF IONIZATIONAL NONEQUILIBRIUM IN AIR PLASMAS

Final Technical Report for the Period:
May 1, 1997 – September 30, 2002
Submitted to
Dr. Robert J. Barker
Air Force Office of Scientific Research
Multidisciplinary Research Program of the University Research Initiative

Grant No. F49620-97-1-0316

Submitted by
Professor Charles H. Kruger
Principal Investigator

October 2002

Mechanical Engineering Department
Stanford University
Stanford, California 94305

REPORT DOCUMENTATION PAGE

AFRL-SR-AR-TR-02-

0418

1. AGENCY USE ONLY *(Leave blank)*

2. REPORT DATE

3. REPORT TYPE AND DATES COVERED
01 May 97 to 30 Sep 02 Final

4. TITLE AND SUBTITLE
MURI 97 Mechanisms of Ionizational Nonequilibrium in Air Plasmas

5. FUNDING NUMBERS
61103D
3484/RS

6. AUTHOR(S)
Dr Kruger

7. PERFORMING ORGANIZATION NAME(S) AND ADDRESS(ES)
Stanford University
651 Serra Street
Room 260
Stanford CA 94305-4125

8. PERFORMING ORGANIZATION REPORT NUMBER

9. SPONSORING/MONITORING AGENCY NAME(S) AND ADDRESS(ES)
Department of the Air Force
Air Force Office of Scentific Research
801 N. Randolph St Rm 732
Arlington. VA 22203-1977

10. SPONSORING/MONITORING AGENCY REPORT NUMBER
F49620-97-1-0316

11. SUPPLEMENTARY NOTES

12a. DISTRIBUTION AVAILABILITY STATEMENT
Distribution Statement A. Approved for public release; distribution is unlimited.

12b. DISTRIBUTION CODE

13. ABSTRACT *(Maximum 200 words)*
The goal of this MURI program was to discover physical mechanisms for significantly reducing the power budget required to create and sustain large volume atmospheric air plasmas at temperature below 2000K with electron number densities of the order of 10 13 cm -3. The Stanford consortim Experimentally demonstrated the generation of over 10 12 electrons/cm 3 in atmospheric pressure air at 2000K, with an average power of 12 W/cm 3, i.e. 250 times smaller than a DC discharge at 10 12/cm3.

14. SUBJECT TERMS

15. NUMBER OF PAGES

16. PRICE CODE

17. SECURITY CLASSIFICATION OF REPORT	18. SECURITY CLASSIFICATION OF THIS PAGE	19. SECURITY CLASSIFICATION OF ABSTRACT	20. LIMITATION OF ABSTRACT
Unclassified	Unclassified	Unclassified	UL

MECHANISMS OF IONIZATIONAL NONEQUILIBRIUM IN AIR PLASMAS

Final Technical Report for the Period:
May 1, 1997 – September 30, 2002
Submitted to
Dr. Robert J. Barker
Air Force Office of Scientific Research
Multidisciplinary Research Program of the University Research Initiative

Grant No. F49620-97-1-0316

Submitted by
Professor Charles H. Kruger
Principal Investigator

October 2002

Contents

Section **Page**

1. Abstract

The present report describes the accomplishments of the Stanford Consortium during the Air Plasma Rampart MURI program (May 1997-September 2002). The Stanford consortium includes the groups of Profs. Kruger and Zare at Stanford University, Prof. Candler at the University of Minnesota, and Dr. Kelley, at Boeing until April 2001 and then with the Stanford group until September 2002. The goal of this MURI program was to discover physical mechanisms for significantly reducing the power budget required to create and sustain large volume atmospheric air plasmas at temperature below 2000 K with electron number densities of the order of 10^{13} cm^{-3}. The Stanford consortium has achieved the following results:

- Experimentally determined the power requirements of thermal air plasmas with electron densities higher than 10^{13} cm^{-3}.
- Determined the chemical reaction pathways that control ionization and recombination in two-temperature atmospheric air and nitrogen plasmas produced by DC and pulsed discharges.
- Experimentally demonstrated the production of stable diffuse glow discharges in low temperature (<2000 K) atmospheric pressure air and nitrogen plasmas with electron number densities in excess of 10^{12} cm^{-3}, more than six orders of magnitude higher than in thermally heated air at 2000 K. The measured discharge characteristics compare well with the predictions of a two-temperature kinetic model. Experimental and modeling results show that the steady-state electron number density exhibits an S-shaped dependence on the electron temperature, a behavior resulting from competition between ionization and charge transfer reactions. Non-Maxwellian effects are shown to be unimportant for the prediction of steady-state electron number densities at least for nitrogen plasmas.
- Experimentally demonstrated the generation of over 10^{12} electrons/cm^3 in atmospheric pressure air at 2000 K, with an average power of 12 W/cm^3, i.e. 250 times smaller than a DC discharge at 10^{12}/cm^3. This result was achieved with short repetitive high-voltage pulses (100 kHz, 12 kV, 10 ns) following a technique originally proposed in our 1999 Annual Technical report. Plasma volumes of about 1 cm^3 were achieved using a multi-electrode configuration.
- Developed spatially and temporally resolved diagnostics of N_2^+ ion concentrations in DC and pulsed atmospheric pressure nitrogen discharges by means of Cavity Ring-Down Spectroscopy (CRDS). Spatial resolutions of the order of 0.5 millimeter and temporal resolutions of 1 microsecond were achieved. We have also conducted preliminary CRDS experiments to measure the NO^+ ion concentration in air plasmas via its infrared transitions at 4.1 micron. Interpretation of the measurements is found to be limited at present by a poor knowledge of the NO^+ ion spectroscopy.

- Developed a self-consistent computational fluid dynamics model with nonequilibrium thermo-chemistry of the two-temperature discharge experiments. The simulations examined two-dimensional effects associated with the practical realization of low temperature air plasmas with high electron concentrations.

2. Introduction

Nonequilibrium discharges in air and nitrogen plasmas at atmospheric pressure present considerable interest for a wide range of applications. Desirable conditions are electron densities of the order of 10^{13} cm^{-3} at gas temperatures less than 2000 K. The equilibrium concentration of electrons in low temperature atmospheric pressure air is extremely small. At 2000 K, for instance, it is approximately equal to 3.3×10^{6} cm^{-3}. To produce and sustain electron number densities of 10^{13} electron/cm^3 in air while maintaining the gas temperature below 2000 K, energy must be added to the plasma in a targeted fashion. One method is to apply the energy addition to the free electrons by means of an electrical discharge. Under certain conditions, the energetic electrons produced by the discharge can catalyze plasma ionization reactions and inhibit electron recombination channels without significantly heating the gas. Power budget reduction strategies can then be designed by enhancing ionization channels or by exploiting electron recombination processes. It is therefore important to understand the chemical mechanisms of ionization and recombination in air plasmas with energetic electrons. Such plasmas are sometimes referred to as two-temperature plasmas, with the kinetic temperature of the free-electrons (T_e) being higher than the kinetic temperature of heavy species (T_g).

Section 3 of this report describes a baseline experiment to determine the power required to produce 10^{13} electrons/cm^3 with a thermal plasma. In this case, the plasma is close to equilibrium and the gas temperature, about 4500 K, is higher than the targeted range. Nevertheless, measurements of the power requirements provide a useful point of comparison for power reduction strategies.

Section 4 describes experiments and theoretical analyses of nonequilibrium DC discharges in atmospheric pressure air plasmas at temperatures around 2000 K. We present first our efforts to develop a two-temperature chemical kinetic model of air plasma discharges. We then discuss our DC discharge experiments in atmospheric pressure air and nitrogen. We conclude this section with measurements and predictions of electrical discharge characteristics (electric field vs. current density) and power requirements (product of the electric field and current density). The influence of departures from a Maxwellian distribution of the free-electrons are examined by means of a simplified collisional-radiative model coupled with a Boltzmann solver for a nitrogen plasma.

Section 5 describes results from pulsed discharge experiments in which electron number densities of more than 10^{12} cm^{-3} in air are produced with approximately 12 W/cm^3, more than two orders of magnitude lower than the power required for a DC discharge. The basis of the technique

is to apply short (ten nanosecond), high voltage (~10 kV) electric pulses with a repetition frequency tailored to match the recombination time of electrons.

Section 6 presents a computational methodology to analyze the DC and pulsed discharge experiments. A complete axisymmetric simulation including an 11-species finite-rate air kinetics model and a three-temperature energy formulation was used. The three-temperature model is used to allow separate heavy-particle, vibrational and electron translation temperatures of the plasma. A self-consistent effective binary diffusion model is used for the molecular transport properties. The discharge is modeled as a conducting channel, allowing a direct enforcement of total current conservation.

Section 7 describes experiments conducted to measure spatial and temporal profiles of N_2^+ ion concentrations in DC and pulsed atmospheric pressure nitrogen glow discharges by Cavity Ring-Down Spectroscopy. Using a collisional-radiative model we infer electron number densities from the measured ion profiles. The values of electron number density found in this way are consistent with those found from spatially integrated electrical measurements. The spectroscopic technique is clearly favorable, because it offers spatial resolution and does not require knowledge of other discharge parameters. The measurements also demonstrate the feasibility of repetitively pulsing the discharge as a means to elevate the time-averaged ionization fraction. Measurements of the NO^+ ion in air plasmas have also been demonstrated. The accessible spectral features of NO^+ are vibrational transitions, are considerably weaker than the UV electronic transitions used to probe N_2^+. Nevertheless, CRDS data from air plasmas was obtained, and spectral features attributed to NO^+ were observed. More precise knowledge of the spectroscopic constants of NO^+ is needed to match the experimental data with modeled spectra.

Section 8 provides conclusions and summary of this report.

3. Thermal Baseline Experiments

Thermal plasma processes represent a convenient method for producing atmospheric pressure air plasma volumes of dimensions greater than 5 cm in all directions with the desired electron number densities. Although the plasmas generated with thermal processes are in a state of Local Thermodynamic Equilibrium (LTE), which implies that the gas temperature ($\geq$~4500 K) is higher than the targeted range for applications of interest, it is interesting to establish the power budget required for generating such plasmas. This section of the report describes the thermal baseline experiments conducted at the High Temperature Gasdynamics Laboratory of Stanford University. In this work, the generation of steady-state, atmospheric pressure air plasma volumes greater than 5 cm in all directions, with electron number densities greater than 10^{13} cm^{-3}, was demonstrated and the power budget requirements were measured.

3.1. Plasma Torch Facility

Atmospheric pressure, thermal air plasmas were generated by a 50 kW inductively-coupled plasma torch (TAFA Model 66) powered by a radio-frequency LEPEL Model T-50-3 power supply operating at 4 MHz. The power supply delivers up to 120 kVA of line power to the oscillator plates with a maximum of 12 kV DC and 7.5 A. The oscillator plates have a maximum RF power output of 50 kW. A schematic drawing of the plasma torch head is shown in Figure 1. The feed gas is injected at the bottom of a quartz tube (inner diameter 7.6 cm, thickness 3 mm) surrounded by a coaxial 5-turn copper induction coil (mean diameter 8.6 cm) traversed by a radio frequency current. The outer Teflon body acts as an electrical insulator and electromagnetic screen. The coil is cooled with de-ionized water to prevent arcing between its turns. The rf current produces an oscillating axial magnetic field that forces the free-electrons to spin in a radial plane and thereby generates eddy currents. The oscillating magnetic field induces an oscillating electric field and the induced electromagnetic force accelerates the free electrons, which then transfer their kinetic energy to heavy particles through collisions.

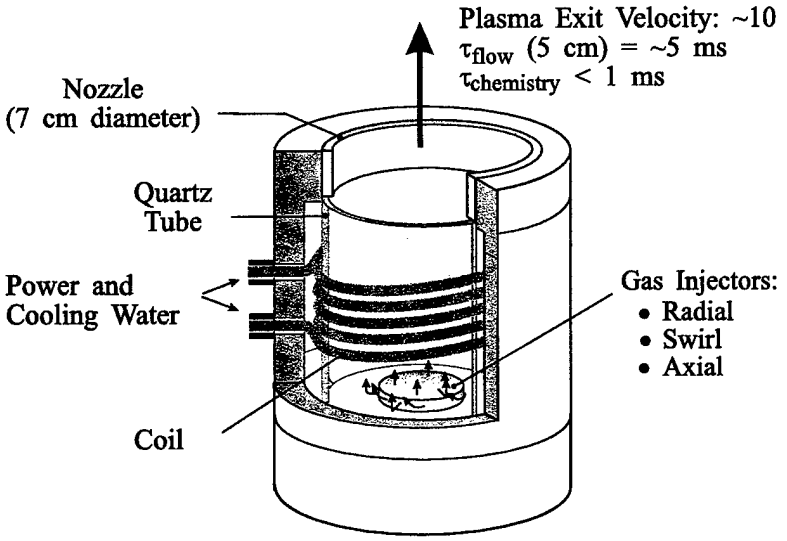

Figure 1. Schematic cross-section of torch head with 7 cm diameter nozzle.

The plasma torch can operate with a variety of gases (air, hydrogen, nitrogen, methane, argon, or mixtures thereof). For the baseline experiments reported here, the feed gas was primarily air with a small amount of hydrogen (less than 2% mole fraction) for purposes of electron number density measurements. The feed gas can be injected in axial, radial or swirl modes through the manifold located at the bottom of the torch. Axial injection provides bulk movement to the gas during the start-up phase. In normal operation, only swirl and radial injectors are used. As will be seen below, the swirl-to-radial feed ratio has a large impact on the temperature and concentration profiles of the plasmas produced by the torch.

The plasma generated in the coil region expands into ambient air through a converging copper nozzle. Different nozzle diameters from a few millimeters to 7 cm can be mounted on the torch; for the present work, a 7 cm nozzle was used. At the nozzle exit plane the maximum axial velocity is estimated to be ~10 m/s, the maximum temperature ~7000 K, the density $\rho \cong 5.04\times 10^{-2}$ kgm^{-3} and the dynamic viscosity $\mu \cong 1.6\times10^{-4}$ kg.m^{-1}s^{-1}. Based on the nozzle diameter of 7 cm, the Reynolds number at the nozzle exit is about 220. The plasma jet is therefore laminar at locations of 1 and 5 cm downstream of the nozzle exit where the measurements presented below were made. Downstream of the nozzle exit at a distance equal to a few nozzle diameters, the plasma plume becomes turbulent as a result of mixing with ambient air.

The temperature and electron number density measurements presented in the following section were made by means of optical emission spectroscopy. The experimental set-up, shown in Figure 2, includes a SPEX model 750M, 3/4 meter, scanning monochromator fitted with a

1200 lines/mm grating blazed at 500 nm and a backthinned, UV-coated SPEX Model TE-2000 Spectrum One thermoelectrically cooled CCD camera. The CCD chip measures 30×12 mm and contains 2000×800 square pixels of dimension 15×15 μm. Absolute intensity calibrations were obtained with an Optronics model OL550 radiance standard traceable to NIST standards.

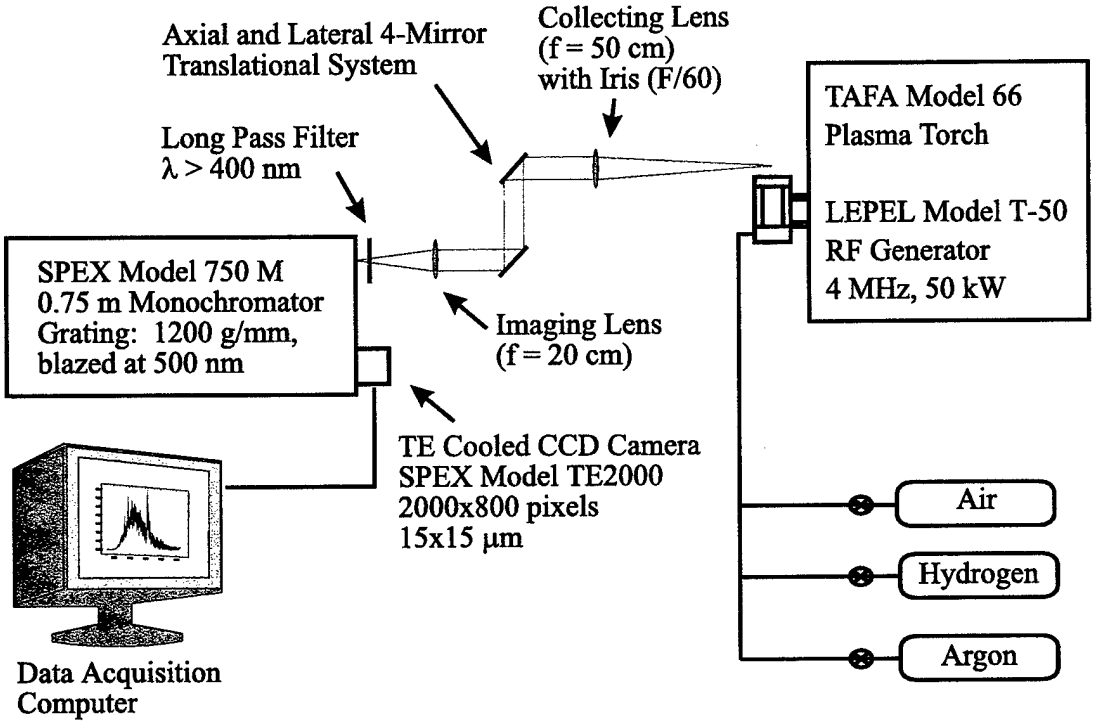

Figure 2. Experimental Set-up for Emission Diagnostics.

3.2. Plasma Characterization

Figure 3 shows photographs of the plasma plume downstream of the nozzle exit for three different conditions of swirl/radial ratio. In the "low swirl case", the flow rates were 67 slpm (standard liter per minute) in radial mode and 33 slpm in swirl mode. The "medium" and "high" swirl cases correspond to radial/swirl flow rates of 67/50 and 67/67, respectively. In all three cases, the plate power was approximately 41.2 kW and a small quantity of hydrogen (~2.3 slpm) was premixed prior to injection into the torch. To a good approximation the flow injected into the torch is thermodynamically equivalent to humid air with ~2.3 slpm of water vapor.

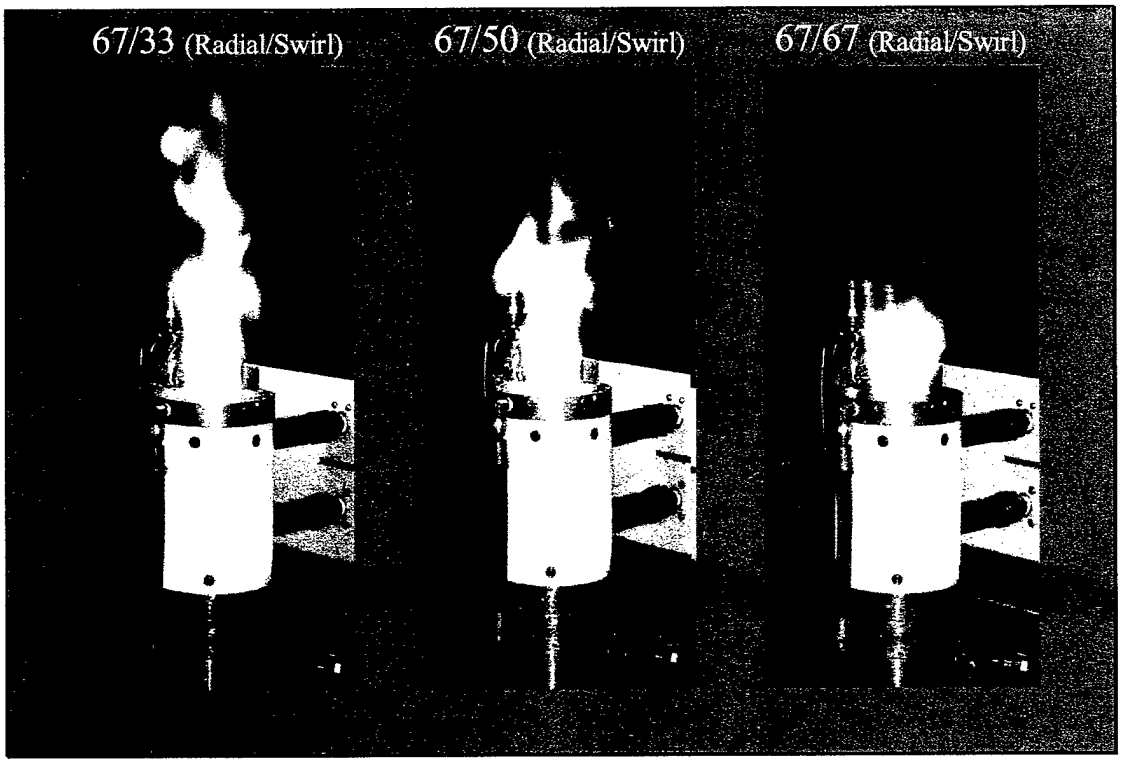

Figure 3. Air Plasma Plume for three Conditions of Radial/Swirl Flow.

As can be seen from Figure 3, the swirl/radial injection ratio has a noticeable influence on the physical aspect of the plasma. The length of the plume is approximately 35 cm, 20 cm, and 10 cm for the low (67/33), medium (67/50) and high (67/67) swirl cases, respectively. The plasma luminosity exhibits a strong radial gradient in the low swirl case, but in contrast it is almost radially uniform in the high swirl case (it is not possible to observe radial variations of the luminosity in Figure 3 as the photographs are intensity-saturated). It thus appears that the plasma properties (temperature, electron number density) are likely to be more uniform radially in the case with highest swirl injection.

Measurements were made of temperature and electron number density radial profiles at locations 1 and 5 cm downstream of the nozzle exit. Temperature profiles were determined from the absolute intensity of the atomic line of oxygen at 777.3 nm. The temperature profiles measured at the location 1 and 5 cm downstream of the nozzle exit for a plate power of 41.2 kW are shown in Figure 4 and Figure 5 for both the low and high swirl cases. As can be seen from these figures, radial profiles are flatter in the high swirl case (67/67) than in the low swirl case (67/33), in accordance with the visual aspect of the plasma plume.

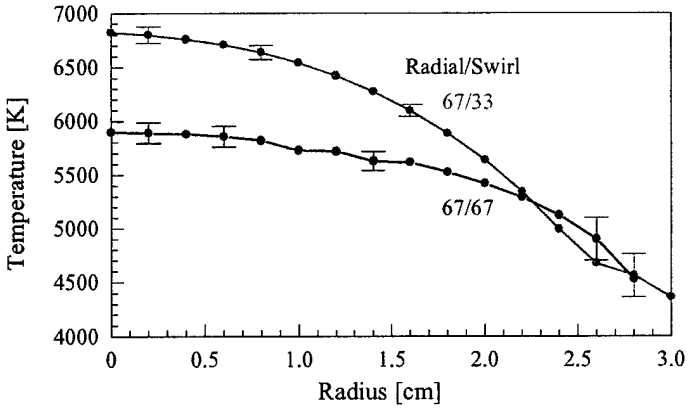

Figure 4. 1 cm downstream of the nozzle exit. Measured temperature profiles from Abel-inverted absolute intensity profiles of the atomic oxygen triplet at 777.3 nm. Plate power = 41.2 kW. Gas: Air+2.3 slpm H_2.

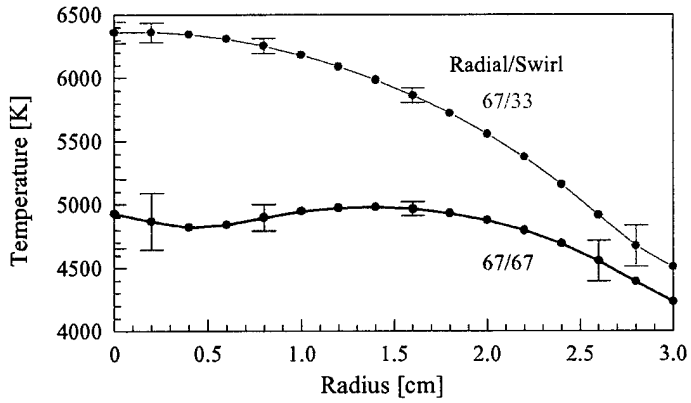

Figure 5. 5 cm downstream of the nozzle exit. Measured temperature profiles from Abel-inverted absolute intensity profiles of the atomic oxygen triplet at 777.3 nm. Plate power = 41.2 kW. Gas: Air+2.3 slpm H_2.

In previous studies conducted in our laboratory, we had found that air plasmas generated by the torch under similar conditions of temperature and velocity were close to Local Thermodynamic Equilibrium (LTE) [1]. This observation reflects the fact that characteristic chemical relaxation times are typically 10 times longer than the characteristic flow time for a 7 cm diameter nozzle (smaller diameter nozzles produce faster flowing plasmas for which characteristic flow times may become smaller than chemical times). It is thus expected that the relatively slow plasmas flowing through the 7 cm diameter nozzle are close to LTE both at 1 and 5 cm downstream of the nozzle exit. Under LTE conditions, electron number densities can be determined from the knowledge of the plasma temperature using chemical equilibrium relations (Saha equation). Figure 6 and Figure 7 show the equilibrium electron number density profiles corresponding to the temperature profiles of Figure 4 and Figure 5. In order to verify the LTE, we also made direct electron number density measurements from the Stark-broadened atomic hydrogen Balmer β line at 486 nm.

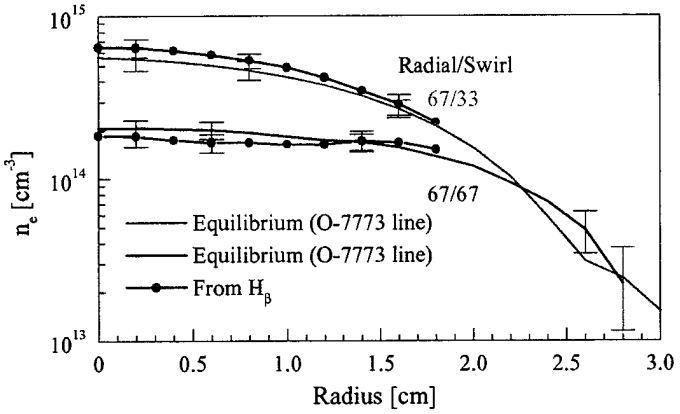

Figure 6. 1 cm downstream of the nozzle exit. Measured electron number density profiles from Abel-inverted H_β lineshapes and equilibrium electron number density profiles based on the temperature profiles of Figure 4. Plate power = 41.2 kW. Gas: Air+2.3 slpm H_2.

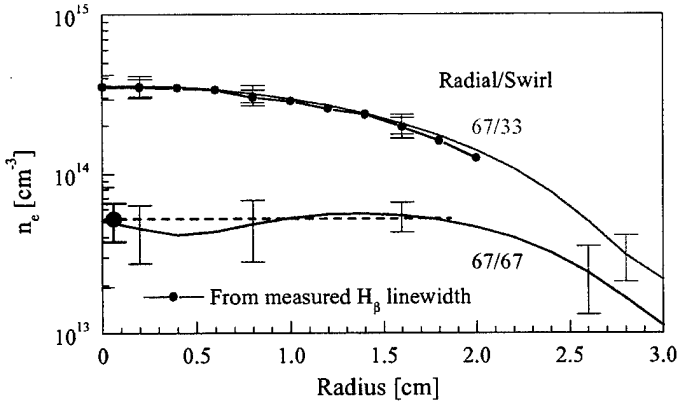

Figure 7. 5 cm downstream of the nozzle exit. Measured electron number density profiles from Abel-inverted H_β lineshapes and equilibrium electron number density profiles based on the temperature profiles of Figure 5. Plate power = 41.2 kW. Gas: Air+2.3 slpm H_2.

In air plasmas, the H_β line sits on top of an intense emission background that is mainly comprised of bands of molecular nitrogen (second positive system). In order to extract the H_β lineshape, spectral measurements were made both with the mixture of air/hydrogen (spectrum labeled "H_β + background" in Figure 8) and with pure air (spectrum labeled "Background"). Spectra measured at several lateral locations along chords of the plasma were then Abel-inverted to provide local emission spectra as a function of the radial location. At each radial location, the H_β lineshapes were recovered by subtracting the background from the total signal. The H_β lineshapes were then fitted with Voigt profiles, which represent the convolution of several broadening mechanisms including pressure (van der Waals, resonance), Doppler, instrumental, and Stark broadening (see Figure 9). Pressure and Doppler broadening widths only depend on the pressure and temperature of the gas. Instrumental broadening was minimized by using a very small en-

trance slit on the monochromator (30 μm). Radial electron number density profiles were determined with the aid of the curves of Figure 9. Results are shown in Figure 6 and Figure 7.

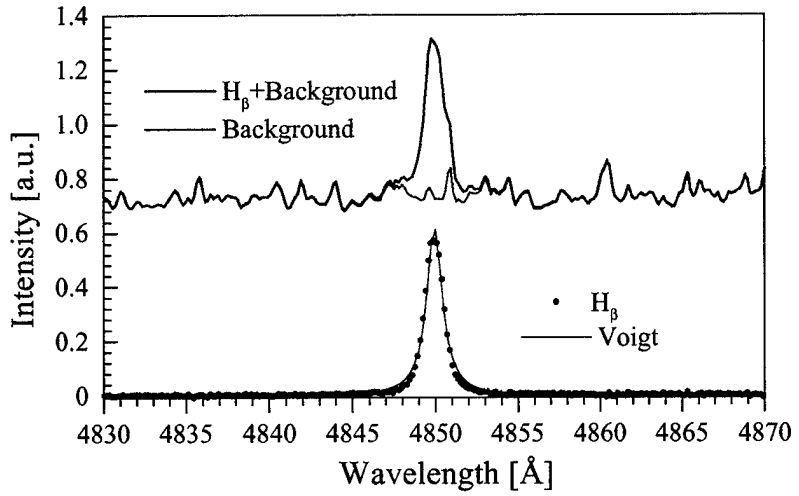

Figure 8. H_β lineshape extraction procedure. 1 cm downstream of the nozzle exit. Low swirl case (67/33 Radial/Swirl). Plate power = 41.2 kW. Gas: Air+2.3 slpm H_2. The two spectra in the figure are those obtained after Abel-inversion at r = 10 mm from the plasma centerline.

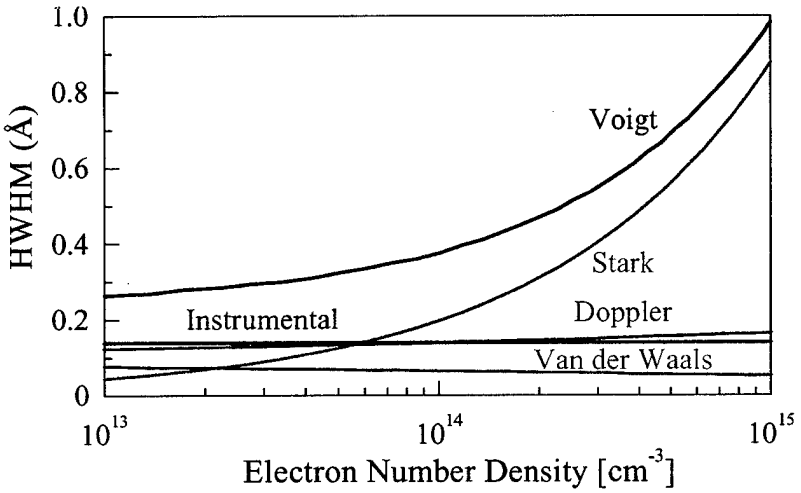

Figure 9. H_β line broadening in atmospheric pressure, equilibrium air. Instrumental broadening is well approximated by a Gaussian of half width at half maximum of 0.14 Å. 1 cm downstream of the nozzle exit. Low swirl case (67/33 Radial/Swirl). Plate power = 41.2 kW. Gas: Air+2.3 slpm H_2. The two spectra in the figure are those obtained by the Abel-inversion procedure at radial location r = 10 mm.

For the high swirl case shown in Figure 7, the H_β line intensity was so weak relative to the nitrogen background (see Figure 10) that it was not possible to obtain a reliable series of Abel-inverted H_β lineshapes. For this case, the lines were not Abel-inverted. Nevertheless, since the plasma temperature does not vary significantly over the central part of the plasma, the electron

number density determined from the H_β lineshape measured along the diameter of the plasma provides an estimate of the average electron number density in the central region. As can be seen from Figure 7, the measured line-of-sight averaged electron density agrees well with the expected equilibrium value in the central region of the plasma.

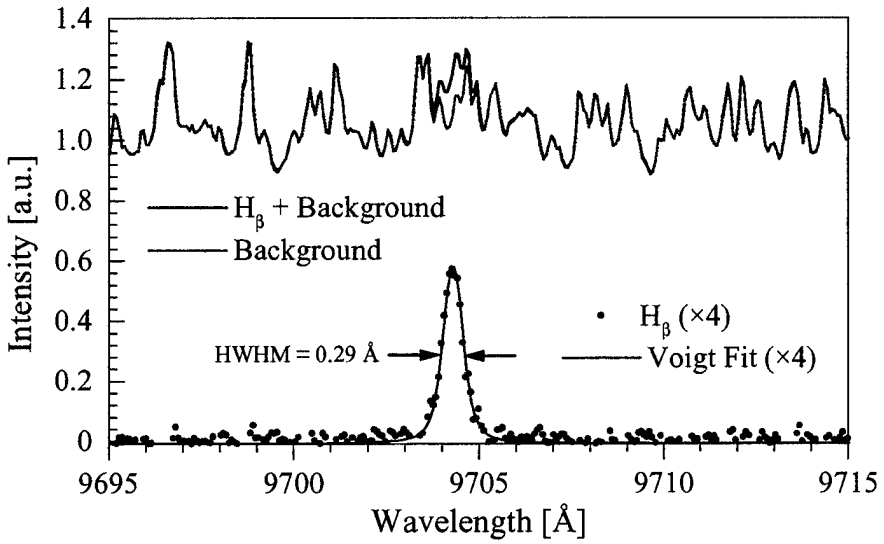

Figure 10. H_β lineshape extraction procedure. Line-of-sight H_β lineshape at location 5 cm downstream of the nozzle exit. High swirl case (67/67 Radial/Swirl). Plate power = 41.2 kW. Gas: Air+2.3 slpm H_2. Here the H_β lineshape was measured in second order so as to reduce instrumental broadening to approximately 0.07 Å.

The foregoing measurements show that the RF plasma torch can generate steady-state air plasmas with electron number densities greater than 10^{13} cm^{-3} over volumes with dimensions greater than 5 cm in all directions. The measurements also indicate that the shape of electron number density profiles can be controlled by modifying the ratio of radial-to-swirl injection. The measurements presented here were obtained with a mixture of air and hydrogen. Measurements were also made for dry air, in which case the electron number density could only be determined by assuming chemical equilibrium at the local temperature measured from the oxygen triplet at 777.3 nm. Results of this series of experiments are shown in Figure 11 and Figure 12 where it can be seen that similar conclusions can be drawn as for the case of humid air.

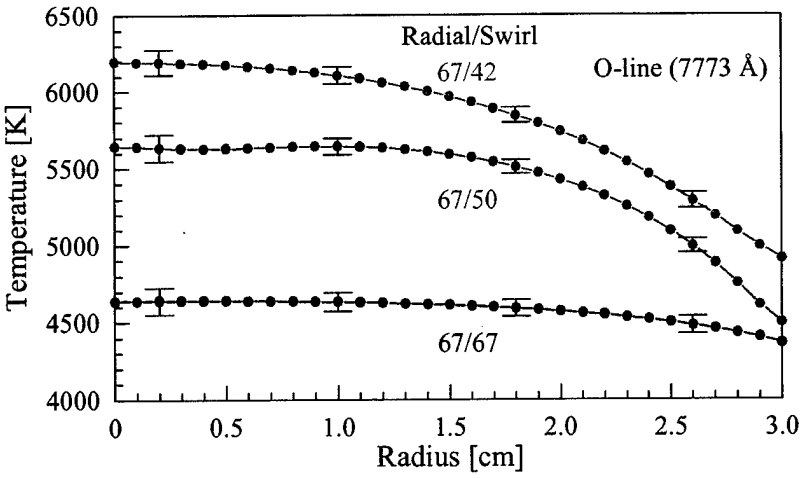

Figure 11. Dry air. Temperature profiles at location 5 cm downstream of the nozzle exit as a function of radial/swirl injection ratio. Plate power = 40.1 kW.

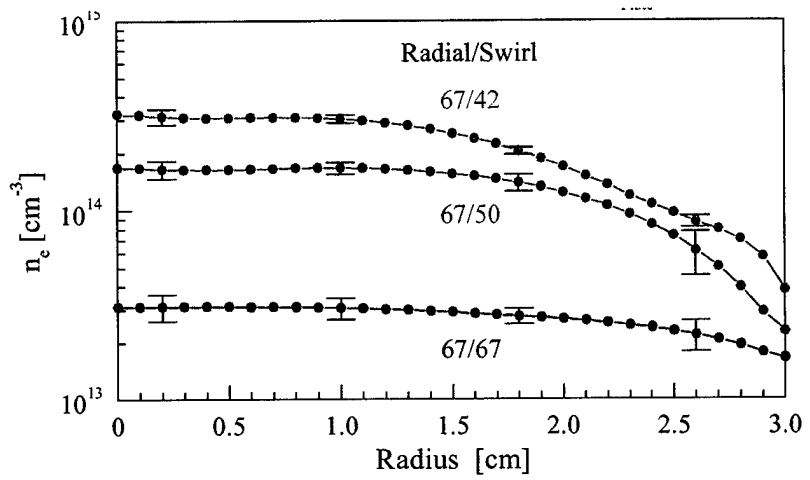

Figure 12. Dry air. LTE electron number density profiles at location 5 cm downstream of the nozzle exit as a function of radial/swirl injection ratio. Plate power = 40.1 kW.

3.3. Power Budget

The main objective of the Air Plasma Rampart program is to significantly reduce the power budget required to generate large volume air plasmas. Budget requirements can be defined in two ways, either as the total wall plug power (which depends on the efficiency of the specific device utilized to generate the plasma) or as the net power deposited into the plasma. In this work, both measurements were made and are described next.

The total wall power was determined by measuring the current in each power lead of the 440 V, triphase power supply, by means of a Fluke Model 33 ampmeter. The average measured rms current was ~72 A (70, 72, and 74 A in each phase, respectively). The total wall power is then given by the following expression:

$$P_{wall} = \sqrt{3}\, I_{rms} V_{rms} \cos\phi \cong \mathbf{48\,kW}$$

where cosϕ, the power factor, is equal to ~0.9 for this type of power supply according to the manufacturer's specifications, and where V_{rms} = 440 V. As the plasma probed in the present experiments was approximately cylindrical of diameter 6 cm and length 5 cm (~140 cm^3), the total volumetric power is ~**340 MW/m^3**.

Additional measurements were made to determine the torch efficiency and the power deposited into the plasma. All power losses can be determined by calorimetry measurements on the cooling water circuit. To this end, the cooling circuit was instrumented with a combination of thermocouples at the inlet and outlet of the generator and turbine flowmeters in the flow lines. The total power removed by the cooling water was measured to be:

$$P_{cooling\ water} = \dot{m}\, C_p\, \Delta T \cong \mathbf{33\ kW}$$

The power deposited into the plasma is given by:

$$P_{plasma} = P_{wall} - P_{cooling\ water} \cong \mathbf{15\ kW}$$

The torch efficiency, defined as $\eta = P_{plasma} / P_{wall}$ is approximately equal to 31 %. Thus, the minimum power required to sustain the thermal plasma volume is ~**105 MW/m^3**.

The total volume of plasma generated in the low swirl case (67/33) depicted in Figure 3 is actually much larger than the probed volume of ~140 cm^3. We estimate that the total volume with electron number densities greater than 10^{13} cm^{-3} was ~1000 cm^3. This estimate includes the volume of plasma generated inside the torch head and the volume extending 10 cm downstream of the nozzle exit. The total volumetric wall power is then ~**48 MW/m^3**, and the minimum volumetric power for an ideal generator is ~**15 MW/m^3**.

3.4. Conclusions on Baseline Experiments

Steady-state air plasmas with electron number densities greater than 10^{13} cm^{-3} and volumes with dimensions greater than 5 cm in all directions were generated in both dry and humid air. The shape of the electron number density profile can be controlled by modifying the ratio of radial-to-swirl injection. The total power required to sustain open volumes of thermal air plasma is measured to be about 340 MW/m^3, or 105/η MW/m3, where η represents the efficiency of the specific device used to produce the plasma. It is important to emphasize again that the plasmas generated in this work are thermal plasmas, i.e. in a state of LTE, and accordingly that the plasma temperature was always greater than ~4500 K. Efforts to reduce the plasma temperature require the use of nonequilibrium plasmas. This motivates the work presented in the rest of this report.

4. DC glow discharges in atmospheric pressure air

4.1. Introduction

This section presents experimental and numerical investigations to determine whether and to what extent the electron number density can be increased in air plasmas by means of DC discharges. The strategy is to elevate the electron temperature, T_e, relative to the gas temperature, T_g, with an applied DC electric field.

Section 4.2 describes our numerical investigations of two-temperature air plasma chemical kinetics. We present first the two-temperature kinetic mechanism that we have developed to predict electron number density in air at a given gas temperature, as a function of the electron temperature. We have paid close attention to the influence of the electron temperature on the rate coefficients, because collisions with energetic electrons can affect the vibrational population distribution of molecules, thereby the rates of ionization and dissociation.

Section 4.3 discusses the implications of this analysis for the generation of nonequilibrium air plasmas by means of electrical discharges. We first determine in Section 4.3.1 the relation between electron number density and current density, and between electron temperature and electric field. This is accomplished with Ohm's law and the electron energy equation, as discussed in Section 4.3.2. A key quantity in the electron energy equation is the rate of electron energy lost by inelastic collisions. To predict inelastic losses in air plasmas, we have developed a detailed collisional-radiative model. This model is presented in Section 4.3.3.

Section 4.4 describes our experiments with DC glow discharges in air. We demonstrate that stable diffuse glow discharges with electron densities of up to $\sim 2 \times 10^{12}$ cm^{-3} can be sustained in flowing preheated atmospheric pressure air. The electrical characteristics and thermodynamic parameters of the glow discharges are measured and compared determined.

Section 4.5 compares the measured electrical characteristics of DC glow discharges in air with those obtained with the two-temperature and collisional-radiative model. This comparison validates the two-temperature model theoretical predictions. In addition, it enables us to establish the power requirements of DC discharges in air plasmas. This fundamental understanding forms the basis for the power budget reduction strategy presented in Section 5 of this report.

4.2. Two-temperature kinetic simulations

This section presents results of numerical investigations to determine whether and to what extent electron number densities can be increased in air plasmas by elevating the electron temperature, T_e, relative to the gas temperature, T_g. The two-temperature kinetic mechanism and rates used for this work are presented in Section 4.2.1. In Section 4.2.2, the kinetic model is used to predict the temporal evolution and steady-state species concentrations in an atmospheric pressure air plasma with constant gas temperature of 2000 K and with electron temperatures varied from 4000 K to 18,000 K. In Section 4.2.3, the key reactions controlling ionization and recombination processes are identified. An analytical model based on the set of controlling reactions is then used to predict steady-state species concentrations in two-temperature air. As will be seen, the analytical model not only reproduces the CHEMKIN solution but also predicts an additional range of steady-state electron number densities.

4.2.1. Two-temperature kinetic model

The rate coefficients required for the two-temperature kinetic model depend on the relative velocities of collision partners (related to T_g for reactions between heavy particles and to T_e for electron-impact reactions) and on the population distributions over internal energy levels of atoms and molecules. Thus, these rate coefficients correspond to the weighted average of elementary rates over internal energy states of atoms and molecules. This forms the basis of the Weighted Rate Coefficient (WRC) method described in Refs [2-5]. With this method, for instance, the total rate coefficient of ionization of atomic nitrogen is calculated as:

$$K_N^{\text{ion.}} = \frac{1}{Q_N}\sum_Y g_Y \exp\left(-\frac{E_Y}{kT_{el}}\right) K_Y^{\text{ion.}}(T_e) \qquad (1)$$

and the rate coefficient of electron-impact dissociation of N_2 as:

$$K_{N_2}^{\text{dis}} = \frac{1}{Q_{N_2}}\sum_Y g_Y e^{\frac{E_Y}{kT_{el}}} \sum_{\text{v}} e^{\frac{G_Y(\text{v})}{kT_{\text{v}}}} \sum_J (2J+1) e^{\frac{F_{Y,\text{v}}(J)}{kT_r}} K_{Y,\text{v},J}^{\text{dis}}(T_e) \qquad (2)$$

where Q_N and Q_{N2} are the total partition functions of N and N_2, E_Y and g_Y the energy and degeneracy of electronic state Y of N or N_2, $G_Y(\text{v})$ and $F_{Y,\text{v}}(J)$ the vibrational and rotational energies of level v and J, and K_Y^{ion} and $K_{Y,\text{v},J}^{\text{dis}}$ the elementary ionization and dissociation rate coefficients, respectively.

As can be seen from Eqns (1) and (2), we assume that the internal energy levels of atoms and molecules are populated according to Boltzmann distributions at the electronic temperature T_{el}, the vibrational temperature T_v, and the rotational temperature T_r. Elementary rate coefficients are

calculated from cross-section data assuming Maxwellian velocity distribution functions for electrons and heavy-particles at T_e and T_g, respectively. We further assume that $T_{el} = T_e$ and $T_r = T_g$. The remaining parameter, T_v, can only be determined in the general case by solution of the master equation for all vibrational levels by means of a collisional-radiative (CR) model that incorporates vibrationally-specific state-to-state kinetics. We have recently developed such a model for nitrogen plasmas [2, 5] that provides insight into the relation between T_v and T_g and T_e in atmospheric pressure plasmas. The nitrogen CR model accounts for electron and heavy-particle impact ionization (atoms and molecules) and dissociation (molecules), electron-impact vibrational excitation, V-T and V-V transfer, radiation, and predissociation. Through comparisons between the results of the CR model and of a two-temperature kinetic model of nitrogen that assumed either $T_v = T_g$ or $T_v = T_e$, we have shown [5, 6] for the case of a nitrogen plasma at $T_g = 2000$ K that the steady-state species concentrations determined with the two-temperature kinetic model are in close agreement with the CR model predictions if one assumes (1) that $T_v = T_g$ for electron temperatures $T_e \leq 9500$ K and electron number densities $n_e \leq \sim 10^{11}$ cm^{-3}, and (2) that $T_v = T_e$ or $T_v = T_g$ for $T_e > 9500$ K and $n_e \geq \sim 10^{15}$ cm^{-3} (in the latter range, best agreement is obtained with $T_v = T_e$ but assuming $T_v = T_g$ leads to electron number densities that are underestimated by at worse a factor of 5). It should be noted that the often-used assumption $T_v = T_e$ produces steady-state electron number densities that are several orders of magnitude greater than those obtained with the CR model for electron temperatures $T_e \leq 9500$ K and electron number densities $n_e \leq \sim 10^{11}$ cm^{-3}. We extend these results to atmospheric pressure air by calculating all WRC rate coefficients with the assumption $T_v = T_g$.

The full 11-species (O_2, N_2, NO, O, N, O_2^+, N_2^+, NO^+, N^+, O^+, and electrons), 40-reaction mechanism and rate coefficients for the case $T_g = 2000$ K are summarized in Table 1. Electron attachment reactions can be neglected in atmospheric pressure air at temperature >1500 K because the equilibrium concentrations of O_2^- or O^- are negligibly small relative to the concentration of electrons above ~1500 K (Figure 13). For reactions between nitrogen species, the rate coefficients are taken from Yu et al. [6]. This set is supplemented by two-temperature rate coefficients determined using the WRC method for electron impact dissociation and ionization of O_2 and NO. For electron-impact ionization of O, we adopt the two-temperature rate of Lieberman and Lichtenberg [7]. Rate coefficients for $O^+ + N_2 \Leftrightarrow NO^+ + N$ and $O^+ + O_2 \Leftrightarrow O_2^+ + O$ are taken from Hierl et al. [8], and the rate coefficient of the charge transfer reaction between O^+ and NO is calculated using the experimental cross-section reported by Dotan and Viggiano [9]. The remaining reactions involve collisions between heavy particles and thus mostly depend on the gas kinetic temperature (as we assume $T_r = T_v = T_g$). For these reactions, the rate coefficients of Park [10, 11] are employed.

The two-temperature kinetic calculations presented in the rest of this section were made with the CHEMKIN solver [12] modified [13] so as to allow a different temperature (T_e) to be specified for the rates of particular reactions. The extended code functions in similar manner as CHEMKIN. For thermal reactions, reverse rates are computed from equilibrium thermodynamic functions (detailed balance). For reaction rates that depend on T_e, a flag is entered in the CHEMKIN reaction mechanism file after the particular reaction considered and the electron temperature is specified. When reverse rates also depend on T_e, the reverse rate coefficient must be entered explicitly. Otherwise the reverse rate is always calculated at the gas temperature. Reverse rates with a dependence on T_e were determined with the WRC model by detailed balance.

Table 1. Two-temperature kinetic model of air plasmas. The temperature entering the Arrhenius-type expressions is either the gas (T_g) or the electron (T_e) temperature, as indicated in columns k_f (forward rate) and k_r (reverse rate). The present mechanism if valid at gas temperatures greater than 1500 K.

Reaction	Temperature dependence		Rate coefficient, $k = A\,T^b \exp(-E/RT)$			Ref.
	K_f	k_r	A (mole,cm,s)	b	E/R (K)	
O_2 Dissociation/Recombination						
1. $O_2 + O_2 = 2O + O_2$	Tg	Tg	2.00E+21	−1.5	59500	a
2. $O_2 + NO = O + O + NO$	Tg	Tg	2.00E+21	−1.5	59500	a
3. $O_2 + N_2 = O + O + N_2$	Tg	Tg	2.00E+21	−1.5	59500	a
4. $O_2 + O = O + O + O$	Tg	Tg	1.00E+22	−1.5	59500	a
5. $O_2 + N = O + O + N$	Tg	Tg	1.00E+22	−1.5	59500	a
6f. $O_2 + E => O + O + E$	Te		2.85E+17	−0.6	59500	b
6b. $O + O + E => O_2 + E$	Te		4.03E+18	−0.4	0	b
NO Dissociation/Recombination						
7. $NO + O_2 = N + O + O_2$	Tg	Tg	5.00E+15	0.0	75500	a
8. $NO + NO = N + O + NO$	Tg	Tg	1.10E+17	0.0	75500	a
9. $NO + N_2 = N + O + N_2$	Tg	Tg	5.00E+15	0.0	75500	a
10. $NO + O = N + O + O$	Tg	Tg	1.10E+17	0.0	75500	a
11. $NO + N = N + O + N$	Tg	Tg	1.10E+17	0.0	75500	a
12f. $NO + E => N + O + E$	Te		3.54E+16	−0.2	75500	b
12b. $N + O + E => NO + E$	Te		8.42E+21	−1.1	0	b
N_2 Dissociation/Recombination						
13. $N_2 + O_2 = N + N + O_2$	Tg	Tg	7.00E+21	−1.6	113200	a
14. $N_2 + NO = N + N + NO$	Tg	Tg	7.00E+21	−1.6	113200	a
15. $N_2 + N_2 = N + N + N_2$	Tg	Tg	7.00E+21	−1.6	113200	a
16. $N_2 + O = N + N + O$	Tg	Tg	3.00E+22	−1.6	113200	a
17. $N_2 + N = N + N + N$	Tg	Tg	3.00E+22	−1.6	113200	a
18f. $N_2 + E => N + N + E$	Te		1.18E+18	−0.7	113200	b
18b. $N + N + E => N_2 + E$	Te		1.36E+23	−1.3	0	b
Zeldovich reactions						
19. $N_2 + O = NO + N$	Tg	Tg	6.40E+17	−1.0	38400	a
20. $NO + O = O_2 + N$	Tg	Tg	8.40E+12	0.0	19400	a
Associative ionization/Dissociative recombination						
21f. $N + O => NO^+ + E$	Tg		8.80E+08	1.0	31900	a
21b. $NO^+ + E => N + O$	Te		9.00E+18	−0.7	0	c
22f. $N + N => N_2^+ + E$	Tg		6.00E+07	1.5	67500	b
22b. $N_2^+ + E => N + N$	Te		1.53E+18	−0.5	0	b
23f. $O + O => O_2^+ + E$	Tg		7.10E+02	2.7	80600	a
23b. $O_2^+ + E => O + O$	Te		1.50E+18	−0.5	0	c
Electron impact ionization/Three-body recombination						
24f. $O + E => O^+ + E + E$	Te		7.74E+12	0.7	157760	d
24b. $O^+ + E + E => O + E$	Te		2.19E+21	−0.8	0	e
25f. $N + E => N^+ + E + E$	Te		5.06E+19	0.0	168200	b
25b. $N^+ + E + E => N + E$	Te		5.75E+26	−1.3	0	b
26f. $O_2 + E => O_2^+ + E + E$	Te		5.03E+12	0.5	146160	b

26b.	$O_2^+ + E + E \Rightarrow O_2 + E$	Te		8.49E+23	−1.9	0	b
27f.	$N_2 + E \Rightarrow N_2^+ + E + E$	Te		2.70E+17	−0.3	181000	b
27b.	$N_2^+ + E + E \Rightarrow N_2 + E$	Te		2.05E+21	−0.8	0	b
28f.	$NO + E \Rightarrow NO^+ + E + E$	Te		2.20E+16	−0.3	107400	b
28b.	$NO^+ + E + E \Rightarrow NO + E$	Te		2.06E+25	−2.0	0	b
Charge exchange/Charge transfer							
29f.	$N^+ + N_2 \Rightarrow N_2^+ + N$	Tg		4.60E+11	0.5	12200	b
29b.	$N_2^+ + N \Rightarrow N_2 + N^+$	Tg=2000K		1.93E+13	0.0	0	b
30.	$NO^+ + O = N^+ + O2$	Tg	Tg	1.00E+12	0.5	77200	a
31.	$NO + O^+ = N^+ + O2$	Tg	Tg	1.40E+05	1.9	15300	a
32.	$O^+ + N_2 = NO^+ + N$	Tg	Tg	4.40E+13	0.0	5664	f
33.	$O^+ + N_2 = N_2^+ + O$	Tg	Tg	9.00E+11	0.4	22800	a
34.	$NO^+ + N = N_2^+ + O$	Tg	Tg	7.20E+13	0.0	35500	a
35.	$O_2^+ + N = N^+ + O_2$	Tg	Tg	8.70E+13	0.1	28600	c
36.	$O_2^+ + N_2 = N_2^+ + O_2$	Tg	Tg	9.90E+12	0.0	40700	c
37.	$NO^+ + O_2 = O_2^+ + NO$	Tg	Tg	2.40E+13	0.4	32600	c
38.	$NO^+ + O = O_2^+ + N$	Tg	Tg	7.20E+12	0.3	48600	c
39.	$O^+ + O_2 = O_2^+ + O$	Tg	Tg	3.26E+13	0.0	2064	f
40.	$O^+ + NO = NO^+ + O$	Tg	Tg	2.42E+13	0.0	902	g

a. Park [11]

b. WRC [4, 5]. These rates were calculated at T_g=T_v=2000 K. The present fitting formulas are valid for $6000 \le T_e \le 20{,}000$ K

c. Park [10]

d. Lieberman [7]

e. Detailed Balance

f. Hierl et al. [8]

g. Dotan and Viggiano [9]

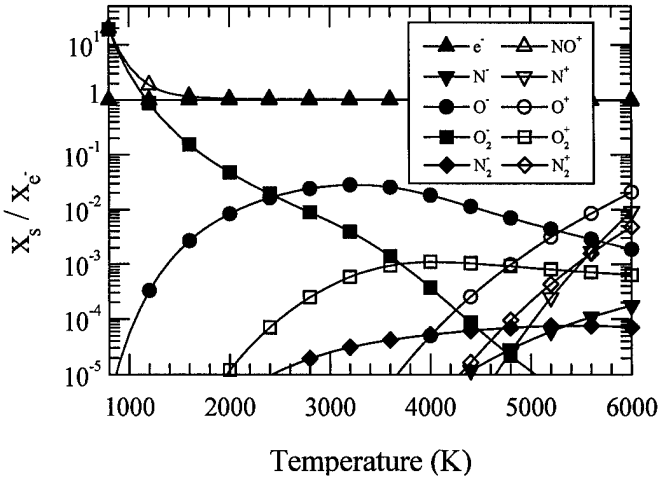

Figure 13. Ion concentrations relative to the electron concentration in equilibrium air (P = 1 atm).

4.2.2. Results

We consider first the case of an air plasma taken to be in equilibrium ($T_g^0 = T_e^0 = 2000$ K, P = 1 atm) at time zero when an elevated electron temperature is instantaneously prescribed, in an idealized way modeling an electrical glow discharge in a reactor section. In the example shown in Figure 14, the gas temperature is held constant at 2000 K and the electron temperature is increased to 13,000 K at time zero. The time evolution of species concentrations computed with the two-

shown in Figure 14, the gas temperature is held constant at 2000 K and the electron temperature is increased to 13,000 K at time zero. The time evolution of species concentrations computed with the two-temperature CHEMKIN solver is shown in Figure 14. The electron number density rises from its initially low value of 3.3×10^{6} cm^{-3} to a steady-state value of $\sim4\times10^{12}$ cm^{-3} in about 0.1 ms. The dissociation fraction of oxygen atoms increases from ~0.03% at time zero to ~1% at steady-state. NO^{+} is the dominant ion at all times.

Additional calculations were made for various electron temperatures while keeping the gas temperature constant at 2000 K. The predicted temporal evolutions of the electron number density are shown in Figure 15. Practically no increase in the electron number density is observed for electron temperatures below a threshold value of $T_e \cong 6000$ K, which corresponds to the temperature where electron-impact ionization reactions begin to dominate over heavy particle-impact dissociation. As the electron temperature is further increased, the steady-state electron concentration increases significantly, with a very abrupt change at $T_e \cong 16800$ K.

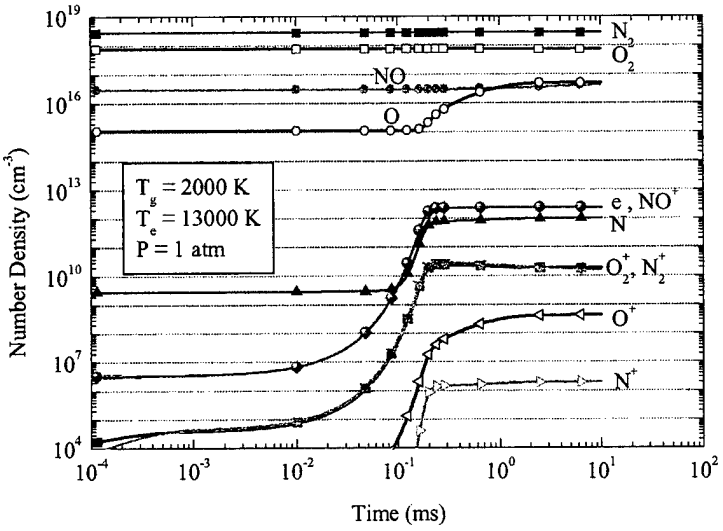

Figure 14. Temporal evolution of species concentrations in atmospheric pressure air at constant gas temperature (2000 K) and constant electron temperature (13000 K).

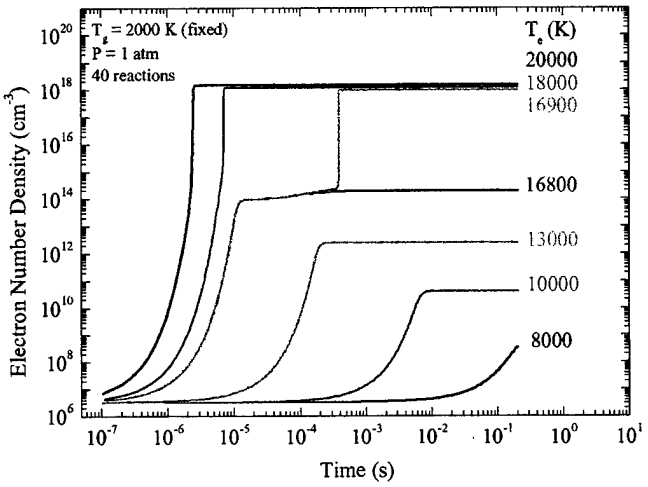

Figure 15. Temporal evolution of the electron number density in a two-temperature air plasma. Initial conditions are equilibrium air at 2000 K ($n_e^{(t=0)} = 3.3\times10^6$ cm^{-3}).

Figure 16 shows the steady-state electron number densities predicted with CHEMKIN as a function of the electron temperature. The abrupt change in electron number density values occurs for an electron temperature of ~16,800 K where the predicted steady-state electron number density suddenly increases from ~1.0×10^{14} to ~1×10^{18} cm^{-3} over a few Kelvin. It is interesting to examine the reverse case where steady-state electron concentrations are calculated for an initial composition given by the steady-state solution corresponding to T_g = 2000 K and T_e = 20,000 K (corresponding to $n_e^{(t=0)} = 1.7\times10^{18}$ cm^{-3}). As can be seen from Figure 17, in this case the predicted steady-state electron number densities start by decreasing along the same curve as in Figure 16, but instead of the abrupt decrease at 16,800 K, continue their slow decrease until the electron temperature reaches ~14,300 K. When the electron temperature is further decreased below ~14,300 K, the steady-state electron number density abruptly decreases to the level of the curve of Figure 16. Thus a hysteresis occurs as the electron temperature is increased and decreased in a cyclical fashion.

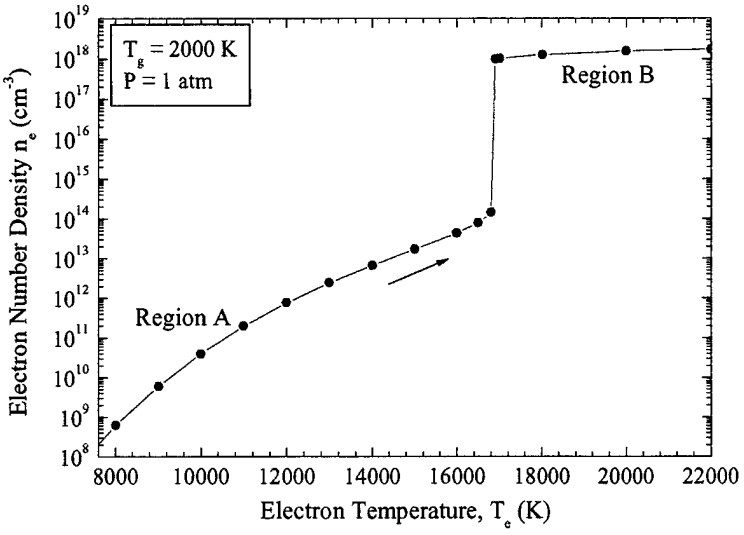

Figure 16. Steady-state electron number density predicted by CHEMKIN for air at T_g = 2000 K, as a function of T_e. For each steady-state calculation, initial conditions are equilibrium air at 2000 K.

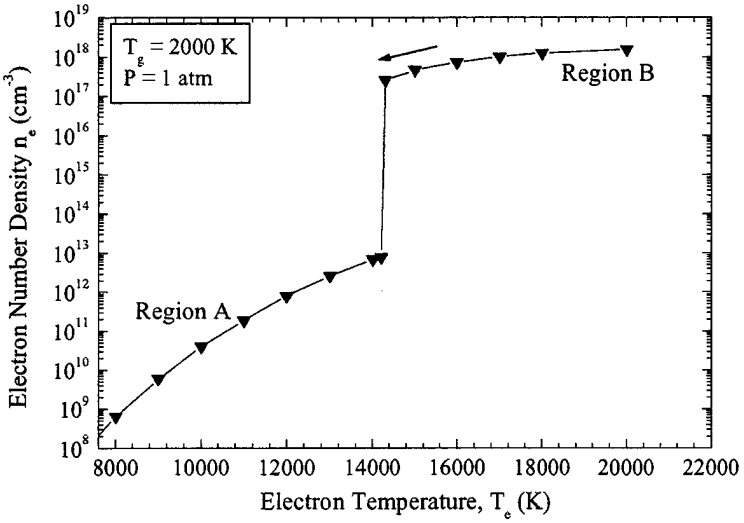

Figure 17. Steady-state electron number density predicted by CHEMKIN for air at T_g = 2000 K, as a function of T_e. For each steady-state calculation, the initial condition corresponds to the steady-state composition predicted by CHEMKIN at T_g = 2000 K and T_e = 20,000 K ($n_e^{(t=0)} = 1.7 \times 10^{18}$ cm^{-3}).

4.2.3. Analysis of the ionization mechanisms

Through detailed examinations of the reactions and rates, we found that the behavior in each of the two regions A and B of the curve in Figure 16 can be explained in terms of the following simplified reaction mechanisms:

4.2.3.a. Ionization mechanism in Region A

In region A, the initial rapid electron concentration rise (see Figure 14 for the case T_e = 13,000 K) is the result of electron-impact ionization of N_2 and O_2 via three-body reactions:

$$O_2 + e \Rightarrow O_2^+ + e + e$$
$$N_2 + e \Rightarrow N_2^+ + e + e$$

and via electron-impact dissociation of O_2 followed by electron-impact ionization of O:

$$O_2 + e \Rightarrow O + O + e$$
$$O + e \Rightarrow O^+ + e + e$$

The charged species produced by these processes undergo rapid charge transfer to NO^+, via

$$O^+ + N_2 \Rightarrow NO^+ + N$$
$$N_2^+ + O_2 \Rightarrow N_2 + O_2^+$$
$$O_2^+ + NO \Rightarrow NO^+ + O_2$$

The main path for electron recombination is the two-body dissociative recombination reaction:

$$NO^+ + e \Rightarrow N + O$$

When the concentration of NO^+ becomes sufficiently large, the rate of dissociative recombination balances the rate of electron production and the plasma reaches steady-state. Thus, in Region A, the termination step for the ionization process is the two-body recombination of a molecular ion.

4.2.3.b. Ionization mechanism in Region B

An example of the temporal evolution of species concentrations in Region B is shown in Figure 18 where the electron temperature is fixed at T_e=18,000 K. As in region A, the electron number density initially increases by electron-impact ionization of N_2 and O_2 via :

$$O_2 + e \Rightarrow O_2^+ + e + e$$
$$N_2 + e \Rightarrow N_2^+ + e + e$$

and via electron-impact dissociation of O_2 followed by electron-impact ionization of O:

$$O_2 + e \Rightarrow O + O + e$$
$$O + e \Rightarrow O^+ + e + e$$

The difference with Region A is that the charge transfer reactions are not fast enough to produce NO^+ at a high enough rate. This is because these reactions are controlled by the gas temperature, whereas electron impact ionization reactions are controlled by T_e. The critical electron temperature that defines the limit between Regions A and B corresponds approximately to the electron temperature for which the rate of the transfer reaction $O^+ + N_2 \Rightarrow NO^+ + N$ is comparable with the rate of avalanche ionization by electron impact. Above this critical electron temperature, the avalanche ionization process continues until all molecular species are dissociated. Eventually the

Eventually the rates of three-body electron recombination reactions balance the rate of ionization, and steady-state is reached.

It is noted that in Region A, electron impact dissociation of N_2 (or NO) is negligible because the dissociation energy of N_2 (9.76 eV) is much larger than that of O_2 (5.11 eV), and the concentration of NO is small relative to the concentration of O_2. It is only above the critical temperature that electron impact dissociation of N_2 starts having a noticeable effect.

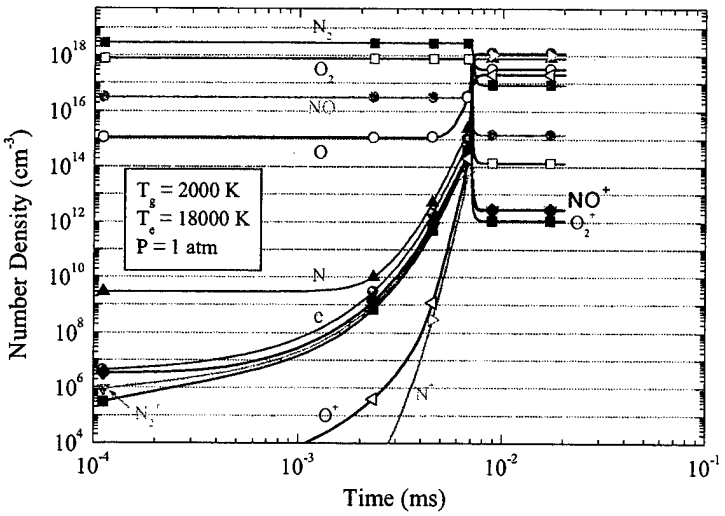

Figure 18. Temporal evolution of species concentrations in atmospheric pressure air at constant gas temperature (2000 K) and constant electron temperature (18,000 K).

4.2.3.c. Analytical solution

The kinetics in Regions A and B can be described with a simplified subset of reactions that takes into account the dominant channels discussed in the foregoing section. With this simplified mechanism, the steady-state concentrations of major species are obtained by solving the following system of equations:

- Steady-state for e^-:
  $O_2 + e \Rightarrow O_2^+ + e + e$
  $N_2 + e \Rightarrow N_2^+ + e + e$
  $O + e \Leftrightarrow O^+ + e + e$
  $NO^+ + e \Rightarrow N + O$
- Steady-state for O_2:
  $O_2 + e \Rightarrow O + O + e$
  $O + O + M \Rightarrow O_2 + M$, with $M = O_2, N_2, O$
- Steady-state for NO^+:

$NO^+ + e \Rightarrow N + O$
$O^+ + N_2 \Rightarrow NO^+ + N$
$O_2^+ + NO \Rightarrow NO^+ + O_2$

- Steady-state for O^+:
  $O + e \Leftrightarrow O^+ + e + e$
  $O^+ + N_2 \Rightarrow NO^+ + N$
  $O^+ + O_2 \Rightarrow O_2^+ + O$
- Steady-state for O_2^+:
  $O_2 + e \Rightarrow O_2^+ + e + e$
  $N_2^+ + O_2 \Rightarrow O_2^+ + N_2$
  $O_2^+ + NO \Rightarrow NO^+ + O_2$
- Steady-state for N_2^+:
  $N_2 + e \Rightarrow N_2^+ + e + e$
  $N_2^+ + O_2 \Rightarrow O_2^+ + N_2$

In writing the corresponding steady-state relations, we make the approximation that the change of plasma volume due to the increase of the total number of moles at constant T and P is negligible, and that the concentration of N_2 remains constant and equal to its initial value. Furthermore, we consider that the dominant neutral species in the plasma are O_2, O, and N_2.

By elimination of n_O, n_{O_2}, n_{O+}, n_{O_2+}, n_{N_2+} and n_{NO+}, we obtain a tenth-degree polynomial in n_e with coefficients that only depend on T_g, T_e, $n_{O2}^{(0)}$, $n_{N2}^{(0)}$ and the rate coefficients. The roots of this polynomial were extracted with the mathematical package MATLAB. The roots that give negative values for n_O are omitted from the solution. The remaining roots of the polynomial are plotted in Figure 19 along with the CHEMKIN predictions corresponding to the full mechanism of Table 1. As can be seen from Figure 19, the approximate solution obtained with the simplified mechanism is in very good agreement with the CHEMKIN predictions in regions A and B. The small discrepancy in Region B is due to the neglecting in our simplified model of nitrogen dissociation. Furthermore, the tenth-degree polynomial exhibits an extra solution that could not be attained with CHEMKIN (Region C). The limits of Region C are the turning points labeled (α) and (β) in Figure 19. If we initialize CHEMKIN with the plasma composition corresponding to a point in Region C of Figure 19, CHEMKIN produces a new steady-state electron number density located on either the lower (Region A) or upper (Region B) limb of the steady-state curves. Thus Region C of Figure 19 cannot be obtained by fixing the electron temperature.

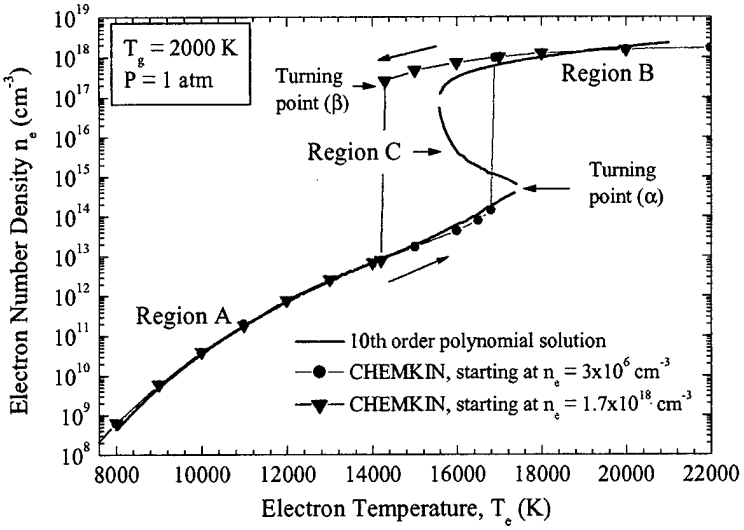

Figure 19. Steady-state electron number densities predicted by CHEMKIN and by the tenth-order polynomial analytical solution.

Figure 20 shows the concentrations of dominant species as predicted by the analytical model. We see that the concentration of NO^+ increases up to turning point (α), and then stays approximately constant as charge transfer becomes slower than oxygen ionization. The concentration of oxygen atoms steadily increases throughout Regions (A) and (C). Beyond turning point (β), molecular oxygen is nearly fully dissociated. The electron concentration is approximately equal to the concentration of NO^+ in Region (A) and to the concentration of O^+ in Regions (B) and (C).

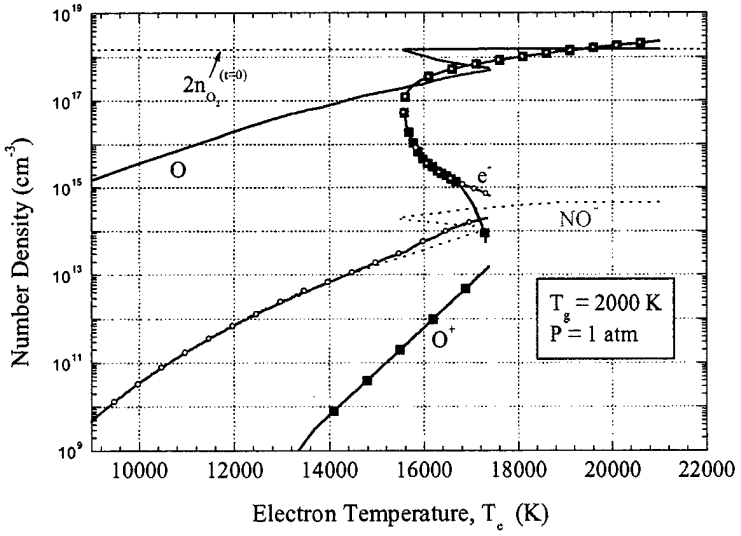

Figure 20. Steady-state species concentrations at T_g = 2000 K, as predicted by the analytical solution.

4.3. Predicted Electric Discharge Characteristics

The electron number density and electron temperature can be related to the current density and electric field, respectively, by means of Ohm's law and the electron energy equation. These relations provide guidance for the design of nonequilibrium DC discharges, as well as an estimate of the power requirements of such discharges.

4.3.1. Ohm's law

Ohm's law relates the current density j to the electric field E:

$$j = \sigma E = \frac{n_e e^2}{m_e \sum_h \bar{\nu}_{eh}} E \tag{3}$$

where σ is the electrical conductivity of the plasma, m_e the electron mass, and $\bar{\nu}_{eh}$ the average frequency of collisions between electrons and heavy particles. The total collision frequency is the sum of the collision frequencies of electrons with neutrals, n, and ions, i:

$$\bar{\nu}_{eh} = \bar{\nu}_{en} + \bar{\nu}_{ei} \tag{4}$$

The electron-neutral collision frequency $\bar{\nu}_{en}$ can be expressed in terms of the number densities of neutral species, n_n, the electron velocity, $g_e = \sqrt{8kT_e/\pi m_e}$, and the energy-averaged momentum transfer cross-sections $\overline{Q_{en}}$ as:

$$\bar{\nu}_{en} \cong n_n \, g_e \, \overline{Q_{en}}$$

The energy-averaged electron-neutral momentum transfer collision cross-sections $\bar{Q}_{eh}$ are calculated by:

$$\bar{Q}_{eh} = \frac{2}{3}\frac{1}{T_e^3}\int_0^\infty \varepsilon^2 \exp\left(-\frac{\varepsilon}{T_e}\right) Q_{eh}(\varepsilon)\, d\varepsilon \tag{5}$$

where T_e is the electron temperature, ε is the electron impact energy, and $Q_{eh}(\varepsilon)$ is the momentum collision cross-section. For N_2, O_2 and O, these cross-sections have been taken from Brown [14], Shkarofsky *et al.* [15], and Tsang *et al.* [16]. The resulting average energy cross-sections $\bar{Q}_{eh}$ are presented in Figure 21.

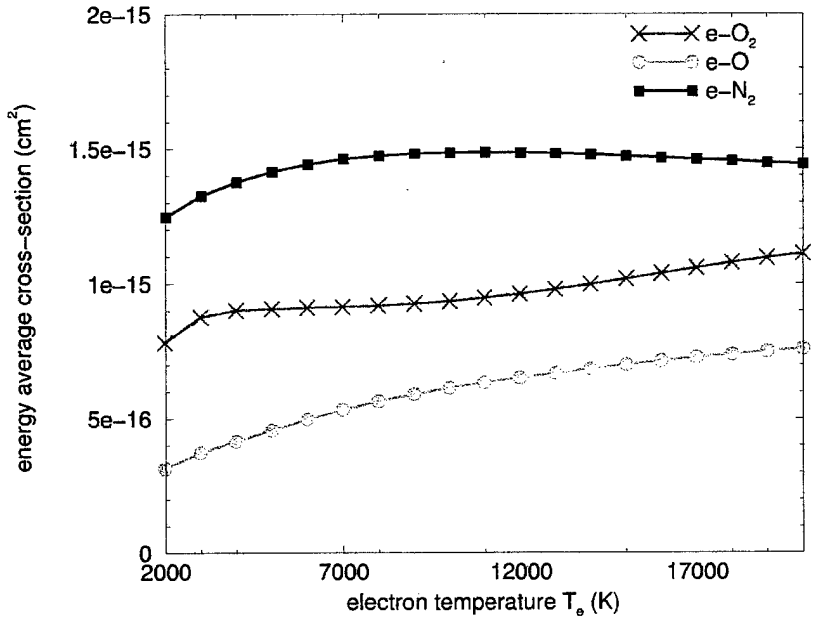

Figure 21: Energy-averaged momentum transfer cross sections for collisions between electrons and N_2, O_2, O.

In Region A, where the dominant neutral species are N_2 and O_2, and where ions have negligible concentrations, the total collision frequency is well approximated by the electron-neutral collision frequency.

In Region B, where the plasma is almost fully ionized, the total collision cross section is approximately equal to the electron-ion collision frequency, which can be expressed as [17]:

$$\bar{\nu}_{ei} = 3.64\times10^{-6} n_i \frac{\ln\Lambda}{T_e^{3/2}} \quad \sec^{-1}, \tag{6}$$

where Λ represents the ratio of the Debye length to the impact parameter for 90° scattering and is approximately equal to 2.5 for electron number densities of 10^{18} cm^{-3} (Mitchner and Kruger [17]).

4.3.2. Electron energy equation

4.3.2.a. Introduction

For a stationary plasma in a DC electric field, the electron energy equation can be written:

$$\sigma E^2 = n_e \sum_h \frac{3}{2} k (T_e - T_h) \frac{2m_e}{m_h} \bar{\nu}_{eh} + \sum_j \varepsilon_j \dot{n}_j + \dot{R} \tag{7}$$

In Eqn. (7), k is the Boltzmann constant and T_h the kinetic temperatures of heavy species (assumed to be the same for all heavy species and thus equal to T_g). The term on the left hand side

second terms on the RHS represent the volumetric power lost by free electrons through elastic and inelastic collisions, respectively, and the last term on the RHS stands for volumetric radiative losses.

In Region A of the S-shaped curve, inelastic energy losses dominate the elastic and radiation losses by at least two orders of magnitude. In Region B, however, inelastic losses are negligible relative to elastic and radiation losses. In the rest of this analysis, we limit ourselves to the lower limb of the S-shaped curve (Region A), and therefore we neglect radiation losses in the rest of this work.

The basis for calculations of inelastic losses in atmospheric pressure air plasmas is summarized below. Electrons lose energy through the following inelastic processes: vibrational excitation of molecular species (VE transfer), ionization, electronic excitation, dissociation of molecules, electronic excitation and ionization of atoms. At electron temperatures below about 17,000 K, the main channel for inelastic electron energy loss in air is via electron impact vibrational excitation of nitrogen. This process is particularly important for the ground state of molecular nitrogen because vibrational excitation by electron impact of this state occurs via resonant transitions to the ground state of the unstable negative ion N_2^-:

$$N_2(X,v'')+e \rightarrow N_2^-(X,v) \rightarrow N_2(X,v')+e$$

The net rate of energy lost by this process is:

$$\dot{\varepsilon}_{v''v'} = \left(K_{v''v'}[N_2(X,v'')][e] - K_{v'v''}[N_2(X,v')][e]\right)\Delta E_{v''v'}$$

where $K_{v''v'}$ and $K_{v'v''}$ are the rate coefficients of electron-impact vibrational excitation and de-excitation, and $\Delta E_{v''v'}$ stands for the difference of energy between the two vibrational levels. The net rate of inelastic losses is a function of the gas and electron temperatures, the electron number density, and the vibrational population distribution of the ground state of N_2. In the limiting case where the vibrational level populations follow a Boltzmann distribution at the electron temperature, the net rate of energy loss by VE transfer is equal to zero because the energy lost by VE excitation reactions is exactly balanced by the energy gained from de-excitation. In the other limiting case where the vibrational levels follow a Boltzmann distribution at the gas temperature, the rate of excitation is much larger than the rate of de-excitation. In the general case, the vibrational population distribution is intermediate between the two previous cases. The vibrational population distribution is then governed by the relative importance of the rates of vibrational excitation by electron impact, and the rates of de-excitation which are mostly determined by collisions with heavy species. The dominant de-excitation processes are vibrational-vibrational transfer between two N_2 molecules (V-

V transfer), vibrational-vibrational transfer between one N_2 molecule and other molecular species such as O_2 and NO (V-V' transfer), and vibrational-translation (V-T) relaxation by collisions of N_2 with other heavy species (N_2, O_2, NO, N and O). Here the main relaxation processes are V-T relaxation by O and N_2. To calculate inelastic energy losses in air, we must therefore predict the vibrational population distribution of the nitrogen ground state by taking into account the aforementioned processes. This is a complex calculation that requires the use of a vibrationally specific Collisional-Radiative (CR) model. We have developed such a model for pure nitrogen plasmas [2, 3, 5, 18] and have recently extended it to air plasmas [19].

4.3.2.b. Rate coefficients controlling the vibrational distribution of N_2 levels

The rate coefficients for VE transfer are calculated [5] using the cross section calculation method of Kazansky and Yelets [20]. This method reproduces available experimental cross-sections relative to the low-lying vibrational levels within about 10%.

For electron temperatures up to 17000K (turning point α in the S-shaped curve), the dominant N_2 V-T, V-V and V-V' relaxation processes are:

$$N_2(Y,v+1)+M \leftrightarrow N_2(Y,v)+M \quad (8)$$

$$N_2(X,v_1+1)+AB(X,v_2) \leftrightarrow N_2(X,v_1)+AB(X,v_2+1) \quad (9)$$

In Eqn. (8), M represents the heavy particle collision partner $M=N_2$, O_2, NO or O and in Eqn. (9), AB is the diatomic molecule N_2, O_2 or NO.

To our knowledge, no experimental data have been reported for the V-T relaxation of N_2 by collisions with N. However Kozlov et al. [21] experimentally determined an upper limit value of the V-T relaxation rate for transition $v=1 \rightarrow v=0$. They showed that for temperatures between 2500K and 4500K, this rate is about one order of magnitude lower than the rate of V-T relaxation of N_2 by collisions with O atoms. Since for our conditions the concentration of N atoms is at least four orders of magnitude lower than the concentration of O atoms, we neglect the V-T relaxation of N_2 by collisions with N atoms.

Most measured vibrational relaxation rate coefficients are for transitions between vibrational levels $v=0$ and 1. When available, experimental rates have been preferred over theoretical ones. The existing experimental rates have been compared and critically selected. Rates for transitions between higher levels have been calculated using scaling functions derived from SSH theory, which is a reasonable approximation when the gas temperature is below 3000K. The reverse rates have been determined by application of the detailed balance method.

For each V-T transfer process, the rates $k_{1,0}$ corresponding to transition $v=1 \rightarrow v=0$ have been calculated with the following analytical expression:

$$k_{1,0} = AT_g^{\,n} \exp\left(-\frac{B}{T_g^{1/3}} + \frac{C}{T_g^{\,m}}\right)\left[1 - D\exp\left(-\frac{E_{10}}{T_g}\right)\right]^{-1} \qquad (10)$$

where $k_{1,0}$ is expressed in $cm^3 s^{-1}$, and T_g and E_{10} (energy of the N_2 transition $v=1 \rightarrow v=0$) are expressed in Kelvin. The parameters *A, B, C, D, m* and *n* are listed in Table 2.

V-T relaxation of N_2 by collision with *O* atoms has been studied experimentally between 300K and 4500K by Breshears and Bird [22], McNeal et al. [23] and Eckstrom [24]. These three sets of experimental data can be well fitted by the Landau-Teller expression of Taylor [25], which reproduces the experimental results within a factor less than two for temperatures lower than 3000K. The parameters of Taylor's expression are reported in Table 2.

V-T relaxation of N_2 by collision with N_2 molecules has been investigated by Lukasik and Young [26], Henderson [27], Millikan and White [28], Hurle [29, 30], Appleton [31], Kovacs and Mack [32] and Kozlov et al. [21]. The analytical expression proposed by Nikitin [33] agrees within a factor less than two with the experimental values for temperatures between 1500K and 3000K. The parameters of Nikitin's expression are reported in Table 2.

No experimental data have been found for V-T relaxation of N_2 by collision with O_2 and *NO* molecules. Since these collision partners have about the same mass as N_2, we have used the same parameters *A, B, C, D, m* and *n* to describe $k_{1,0}$.

Table 2: parameters for the V-T rates $k_{1,0}$

M=	A	B	C	D	m	n
O	1.07×10^{-10}	69.9	0	0	0	0
N_2, O_2, NO	7.8×10^{-12}	218	690	1	1	1

The rate coefficients $k_{v+1,v}$ for transitions $v + 1 \rightarrow v$ between upper vibrational levels have been calculated using appropriate scaling laws from the measured k_{10} rates:

$$k_{v+1,v} = k_{1,0} G(v+1) \qquad (11)$$

Using SSH theory [34] and some approximations for the Morse oscillator model [35], $G(v+1)$ can be expressed as:

$$G(v+1) \approx \frac{(v+1)(1-x_e)}{1-x_e(v+1)} \frac{F(y_{v+1,v})}{F(y_{1,0})} \tag{12}$$

where x_e is the anharmonicity of the N_2 molecule, and $y_{v+1,v}$ is given by:

$$y_{v+1,v} = 0.32 E_{v+1,v} L \sqrt{\frac{\mu}{T_g}}, \tag{13}$$

where $E_{v+1,v}$ is the energy of the $v+1 \rightarrow v$ transition in K, L is the characteristic parameter of the short range repulsive potential in Å, μ is the reduced mass of the two colliding particles in a.u., and T_g is the gas temperature in K. We have taken $L=0.25$ Å for all V-T processes.

The function F in Eqn. (12) is given by [34]:

$$\begin{cases} F(y) = \frac{1}{2}\left[3 - \exp\left(-\frac{2y}{3}\right)\right]\exp\left(-\frac{2y}{3}\right) & \text{for } 0 \le y \le 20 \\ F(y) = 8\left(\frac{\pi}{3}\right)^{1/2} y^{7/3} \exp\left(-3y^{2/3}\right) & \text{for } y > 20 \end{cases} \tag{14}$$

The calculated forward and reverse rates are plotted in Figure 22. The rates for V-T relaxation of $N_2(v)$ by collision with O atoms are between two and three orders of magnitude higher than the rates of V-T relaxation of $N_2(v)$ by collision with N_2.

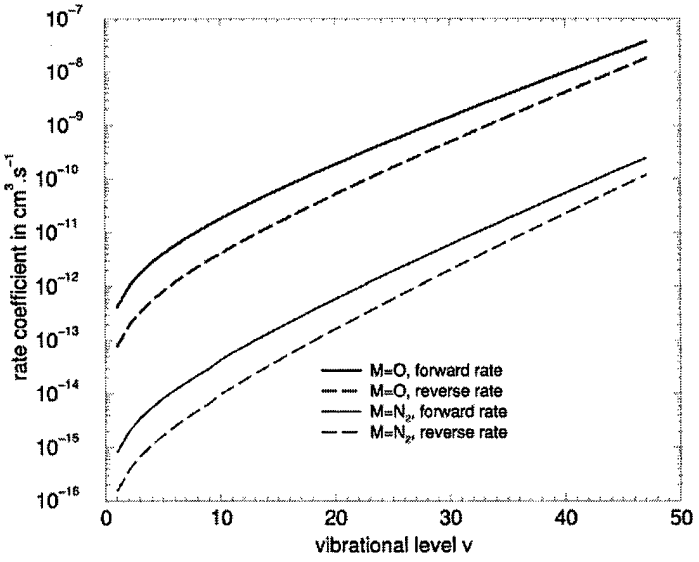

Figure 22. Rate coefficient for V-T relaxation: $N_2(X,v) + M \rightarrow N_2(X,v-1) + M$, with $M=O$, N_2 at T_g=2000K

The rates $k_{1,0}^{0,1}$ corresponding to the V-V and V-V' processes (9) with $v_1=0$ and $v_2=0$, are calculated using the following expression:

$$k_{1,0}^{0,1} = AT_g^{\,n} \exp\left(-\frac{B}{T_g^{1/3}}\right) \tag{15}$$

where the gas temperature T_g is expressed in K and the parameters A, B, n are listed in Table 3.

Table 3. Parameters for the V-V and V-V' rates $k_{1,0}^{0,1}$

V-V or V-V' process	*A*	*B*	*n*
N_2-N_2	1.27E-17	0	1.483
N_2-O_2	1.23E-14	104	1
N_2-NO	4.22E-10	86.35	0

The N_2-N_2 V-V exchange process has been studied experimentally at 300K by [36-41] and theoretically by semiclassical trajectory methods [42, 43] and SSH theory [44, 45]. These results are plotted in Figure 23.

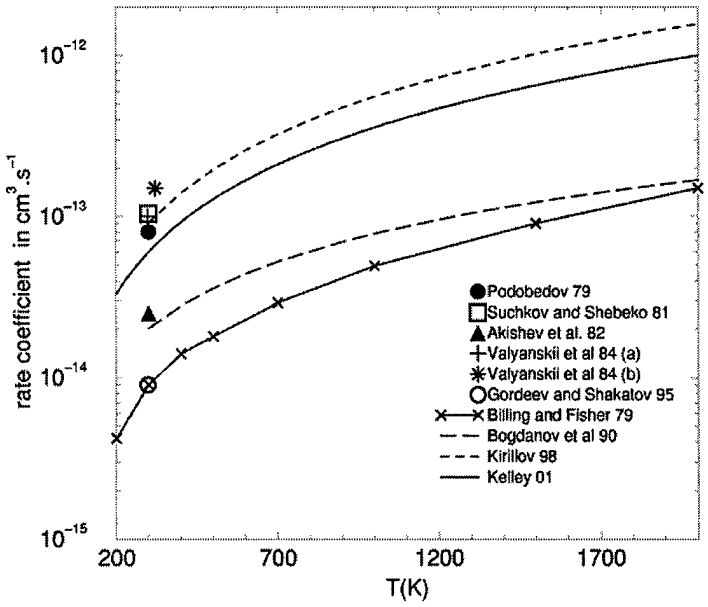

Figure 23. Rate coefficients for V-V relaxation: $N_2(X,1) + N_2(X,0) \rightarrow N_2(X,0) + N_2(X,1)$

There is a disagreement of about one decade among the different results, and the reason for the discrepancy remains unclear. The theoretical models are not exact and contain assumptions that can easily change the calculated rates by up to a factor of 5. On the other hand, measuring V-V probabilities for nitrogen is difficult because of the very weak absorption vibrational spectrum. Podobedov [36], Valyanskii et al [37, 38], Suchkov and Shebeko [39] and Gordeev and Shakatov [41] monitored the relaxation of nitrogen vibrational levels using Raman methods. They obtained the rate constant $k^{0,1}_{v,v-1}$ by fitting their experimental results with solutions of the coupled kinetic equations describing the relaxation process. The uncertainties of the rate constants obtained depend on the accuracy of all parameters implemented in the kinetic equations. However accurate V-V values for CO are available and have been satisfactorily modeled theoretically by Jeffers and Kelley [46]. CO and N_2 are similar in that they have the same number of electrons, the same molecular weight and nearly the same fundamental vibrational frequency. The most significant difference between V-V exchange in CO and N_2 is the long-range dipole-dipole interaction in the former system. If this interaction is absent, as it is for N_2, the short-range repulsive interaction dominates the V-V process. The contribution of the short-range repulsive interaction to the V-V transfer probabilities should be much the same in N_2 as in CO. We have done a calculation for N_2 based on the short-range repulsive interaction model presented in [46]. This calculation leads to rate constants of about 6×10^{-14} cm^3/s at 300 K and about 1×10^{-12} cm^3/s at 2000 K. These rate constants has been fitted with an analytical expression of the form given by Eqn. (15), with the parameters reported in Table 3.

The N_2-O_2 V-V' energy exchange has been studied experimentally for temperatures between 100 and 4500 K by White and Millikan [47, 48], Bauer and Roesler [49], Breashears and Bird [22], Kozlov et al. [21], and Wilson et al. [50]. The different sets of experimental data are in good agreement with one another and are well fitted by the analytical expression of Kozlov [21] which reproduces the experimental results within a factor of 2 for temperatures between 1000 and 3000 K. The parameters of this expression are reported in Table 3.

The N_2-NO V-V' energy exchange has been studied experimentally for temperatures between 300 and 3500 K by Callear [51], Taylor et al. [52], Stephenson [53] and Doyennette and Margotin-Maclou [54]. The analytical expression of Taylor [25], with parameters reported in Table 3, reproduces very well the low temperature (300-400 K) experimental data of Refs. [51, 53, 54]. It also reproduces the high temperature (1500-3400 K) data of Ref. [25] within a factor of three.

The rate coefficients $k_{v_1+1,v_1}^{v_2,v_2+1}$ for exothermic transitions between upper vibrational levels have been calculated using the relation:

$$k_{v_1+1,v_1}^{v_2,v_2+1} = k_{1,0}^{0,1}\, G(v_1+1, v_2+1) \tag{16}$$

where $G(v_1+1,v_2+1)$ is an appropriate function which can be expressed using SSH theory [34] and some approximations for the Morse oscillator model as:

$$G(v_1+1, v_2+1) \approx \frac{(v_1+1)(1-x_{e1})}{1-x_{e1}(v_1+1)} \frac{(v_2+1)(1-x_{e2})}{1-x_{e2}(v_2+1)} \frac{F\left(y_{v_1+1,v_1}^{v_2,v_2+1}\right)}{F\left(y_{1,0}^{0,1}\right)} \tag{17}$$

where x_{e1} and x_{e2} are the anharmonicities of the two molecules involved. $F(y)$ is given by Eqn. (14) with $y_{v_1+1,v_1}^{v_2,v_2+1}$ defined as:

$$y_{v_1+1,v_1}^{v_2,v_2+1} = 0.32\left[E_{v_1+1} - E_{v_1} + E_{v_2} - E_{v_2+1}\right] L\sqrt{\frac{\mu}{T_g}} \tag{18}$$

where E_{v_i} are the energies of the initial and final levels in K. We have taken L=0.25 Å for all V-V and V-V' processes. Note that $y_{v_1+1,v_1}^{v_2,v_2+1}$ must be always positive since we are considering the reaction in the exothermic direction.

The calculated forward and reverse rates are plotted in Figure 24 as a function of the vibrational number v_1 for $v_2=0$. For the N_2-O_2 process, the rates increase up to the resonance point at v_1=27, and decrease after this value. We observe the same behavior for the N_2-NO process but the resonance appears at a lower value of v_1 (v_1=16) because the spacing between NO levels is larger than between O_2 levels. For the N_2-N_2 process, the rates increase until $v_1=5$ and then decrease because of the increasing vibrational energy gap between the two N_2 molecules.

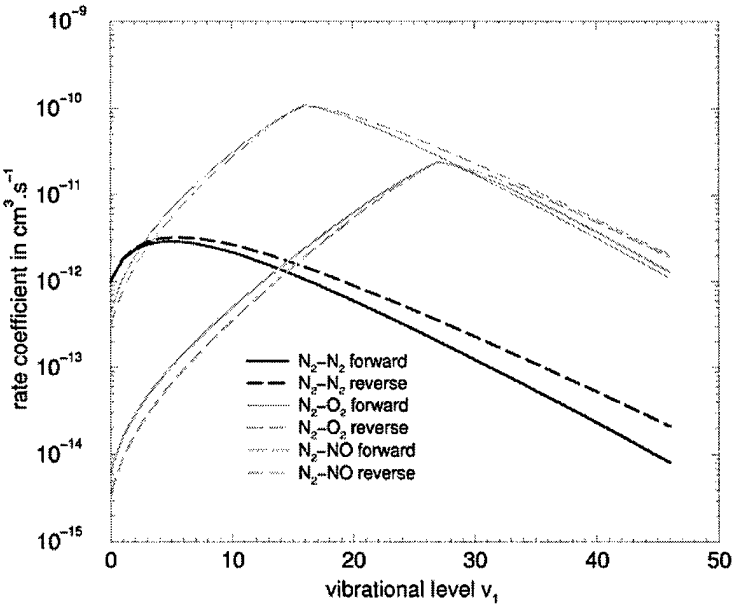

Figure 24. Rate coefficients for V-V and V-V' exchange : $N_2(X,v_1+1) + AB(X,0) \rightarrow N_2(X,v_1) + AB(X,1)$, with $AB = N_2, O_2$ and NO, at T_g=2000K.

4.3.2.c. Vibrational distribution of N_2 ground state

The V-T, V-V and V-V' rates of the foregoing section were implemented in the model and the vibrational distribution of the N_2 ground and excited electronic states was determined by solving a system of kinetic equations at steady state in which the vibrational levels of the N_2 ground and excited electronic states are the unknowns.

The total concentration of N_2 was determined with the two-temperature kinetic model [13] and fixed by replacing the vibrational level $v=0$ of ground electronic state by the mass conservation equation.

The total populations of the other species were fixed and determined with the two-temperature kinetic model, and their internal distribution was calculated according to a Boltzmann distribution at the vibrational temperature $T_v=T_g$ and at the electronic temperature $T_{el}=T_e$. We now present our calculations of the vibrational distribution of the N_2 ground state at T_g=2000K and for different electron temperatures.

For electron temperatures T_e lower than 6000K, the vibrational distribution is very close to a Boltzmann distribution at the gas temperature T_g=2000K. Figure 25 and Figure 26 show the calcu-

lated vibrational distributions for a gas temperature of 2000K and an electron temperature of 9000K and 16000K respectively. The Boltzmann distributions at $T_v=T_g$ and $T_v=T_e$ are also shown on these figures.

For T_e=9000K, the vibrational excitation introduced by VE transfer is mainly redistributed via V-T relaxation of N_2 by collision with N_2, and via N_2-N_2 V-V exchange. The N_2-O_2 and N_2-NO V-V' processes do not significantly affect the populations of N_2 levels. We checked that this conclusion remains valid if we assume a different internal distribution for the O_2 and NO molecules. Indeed, the rates of N_2-NO exchange are faster than those of N_2-N_2 exchange above v=3 (see Figure 24) but the total concentration of NO is two orders of magnitude lower than the concentration of N_2 and the rates for N_2-O_2 V-V exchange are fast for v>20 but the population of those levels is mainly governed by V-T transfer processes. The vibrational distribution at T_e=9000K lies between the Boltzmann distributions at $T_v=T_g$ and $T_v=T_e$, but remains closer to a distribution at $T_v=T_g$.

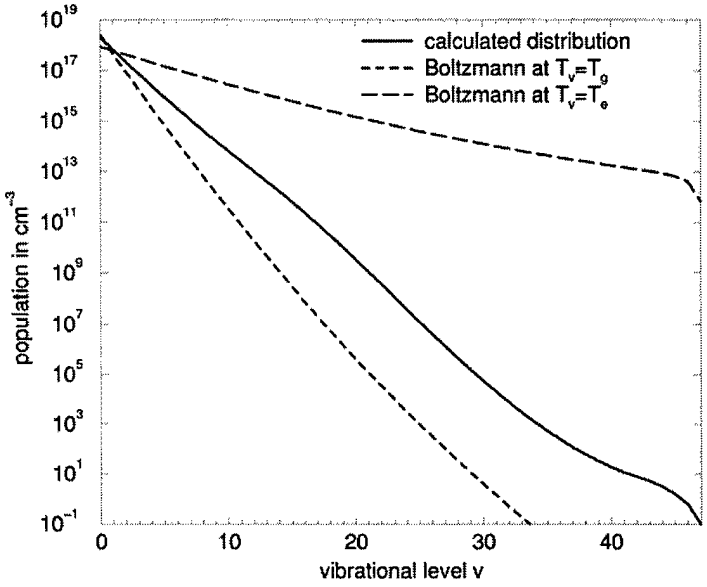

Figure 25. N_2(X,v) vibrational distribution function at T_g=2000K and T_e=9000K, P=1atm

For T_e=16000K, almost 25% of the O_2 molecules are dissociated and the vibrational excitation is mainly redistributed by V-T relaxation of N_2 by collision with O atoms and by N_2-N_2 V-V exchange. At this electron temperature, the vibrational distribution of the first 15 levels is close to the Boltzmann distribution at $T_v=T_e$.

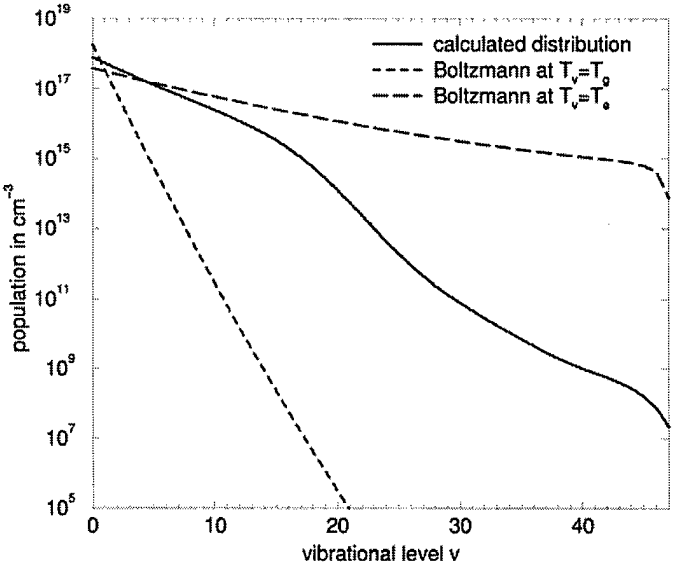

Figure 26. N_2(X,v) vibrational distribution function at T_g=2000K and T_e=16000K, P=1atm.

4.3.2.d. Inelastic electron energy losses in air plasmas

Electron inelastic energy losses can now be calculated by summing the contributions of all electron impact collisional processes:

$$\dot{Q}_{inel} = \sum_{processes}\left[\sum_i\sum_f \frac{dn_f}{dt}\left(E_f - E_i\right)\right] \tag{19}$$

where E_f–E_i represents the internal energy gained by heavy species during the collision (E_f must be greater than E_i) and dn_f/dt is the net volumetric rate of production of heavy species in the final energy level f. In an atmospheric pressure air plasma characterized by a gas temperature between 1000 and 3000 K and electron temperatures up to 17000 K, the dominant contribution to electron inelastic energy losses is the electron-impact vibrational excitation of N_2 ground state. The electron impact vibrational excitation cross-sections of O_2 and NO ground states are two orders of magnitude lower than those of N_2, and therefore the contribution of these molecules is negligible.

The total rate of energy loss can be expressed as:

$$\dot{Q}_{e\text{-}V} = \sum_{v_1}\sum_{v_2>v_1}\dot{Q}_{v_1v_2} \tag{20}$$

where v_1 and v_2 are the initial and final vibrational levels of the transition, and where the elementary rate $\dot{Q}_{v_1v_2}$ is written as:

$$\dot{Q}_{v_1v_2} = \left(k_{v_1v_2}\left[N_2(X,v_1)\right] - k_{v_2v_1}\left[N_2(X,v_2)\right]\right)n_e\Delta E_{v_2v_1} \tag{21}$$

In Eqn. (21), n_e is the concentration of electrons, $k_{v_1v_2}$ and $k_{v_2v_1}$ are the excitation and deexcitation rate coefficients and $\Delta E_{v_2v_1}$ stands for the difference of energy between the two vibrational levels v_2 and v_1.

$\dot{Q}_{v_1v_2}$ depends strongly on the N_2 ground state internal distribution. Vibrational population distributions calculated with the method presented in the foregoing section are used in Eqn. (21) to determine the electron inelastic energy losses. The predicted inelastic power losses are shown in Figure 27. At low electron temperatures and densities, the vibrational levels of N_2 ground state are close to a Boltzmann distribution at T_v=T_g. The excited vibrational levels have low population. Therefore, the power lost by e-V excitation is not balanced by the power regained from V-e superelastic de-excitation. As the electron temperature increases, the electron density also increases and eventually the vibrational population distribution tends toward T_v=T_e. The net power losses do not increase as rapidly because of the increased importance of superelastic collisions.

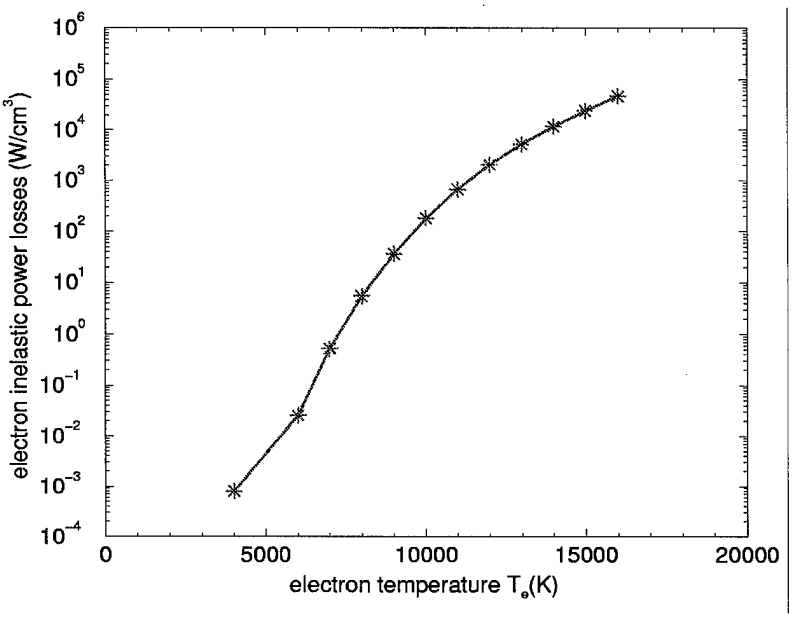

Figure 27. Predicted inelastic electron power losses in atmospheric pressure air at 2000 K.

It is sometimes convenient to define an electron "energy loss factor" as the ratio of total (elastic + inelastic) energy losses to the elastic energy losses:

$$\delta_e = \frac{\dot{Q}_{el} + \dot{Q}_{inel}}{\dot{Q}_{el}} \tag{22}$$

$$\delta_e = \frac{\dot{Q}_{el} + \dot{Q}_{inel}}{\dot{Q}_{el}} \tag{22}$$

where $\dot{Q}_{el}$ is the volumetric power lost by free electrons through elastic collisions, and $\dot{Q}_{el}$ is the sum of contributions of collisions between electrons and heavy species h=N_2, O_2 and O:

$$\dot{Q}_{el} = n_e \sum_h 3k(T_e - T_h)\frac{m_e}{m_h}\bar{\nu}_{eh} \tag{23}$$

In Eqn. (23), k is the Boltzmann constant, m_e and m_h are the masses of electron and heavy species respectively, T_h is the kinetic temperature of the heavy species (equal to T_g), and $\bar{\nu}_{eh}$ represents the average frequency of collisions between the electrons and heavy particle h. $\bar{\nu}_{eh}$ can be expressed in terms of the number density of neutral species n_h, the electron velocity $g_e = \sqrt{8kT_e/\pi m_e}$ and the average elastic collision cross-section $\bar{Q}_{eh}^{el}$:

$$\bar{\nu}_{eh} \cong n_h g_e \bar{Q}_{eh}^{el} \tag{24}$$

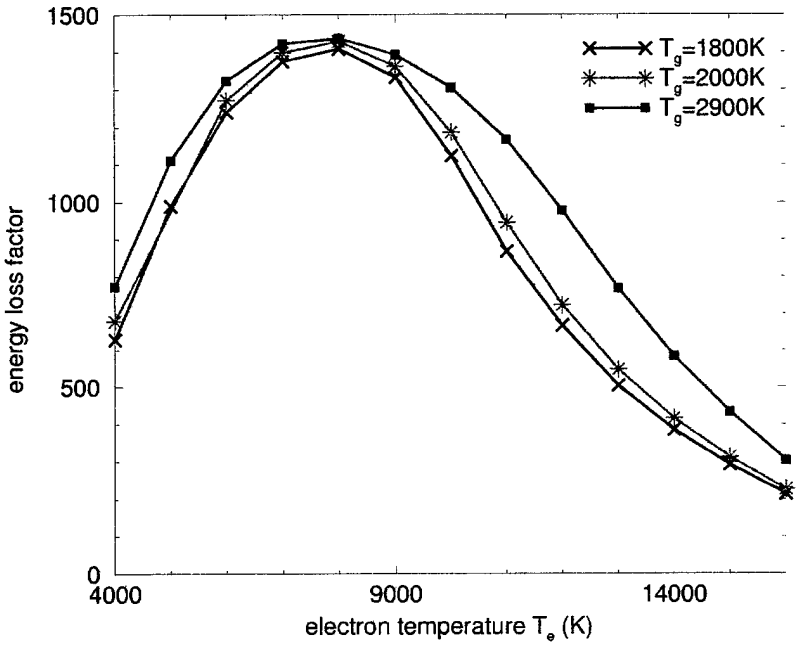

Figure 28. Energy loss factor δ_e at T_g=1800K, 2000, and 2900K, as a function of T_e

Figure 28 shows the calculated electron energy loss factor as a function of the electron temperature for two values of the gas temperature, T_g =1800 and 2900 K. As can be seen from this figure, the inelastic loss factor is a relatively weak function of the gas temperature. It increases up to T_e=8000 K as the net rate of production of N_2 molecules in vibrational level $v_2 > v_1$ increases with T_e, and then decreases due to the transition $T_v \cong T_g$ to $T_v \cong T_e$. When T_v becomes close to T_e, the forward and reverse rates are practically balanced and the net rate of energy lost by VE transfer approaches zero.

4.3.2.e. Predicted DC Discharge Characteristics in Atmospheric Pressure Air

The results of the previous subsections enable us to convert the "S-shaped" curve of n_e vs. T_e into electric field vs. current density discharge characteristics. This result is obtained by combining Ohm's law and the electron energy equation. The latter incorporates the results of the collisional-radiative model to account for non-elastic energy losses from the free electrons to the molecular species. The predicted discharge characteristics for atmospheric pressure air at 2000 K are shown in Figure 29. These discharge characteristics exhibit variations that reflect both the S-shaped dependence of electron number density versus T_e, and the dependence of the inelastic energy loss factor on the electron temperature and number density. We have used these predicted characteristics as a starting point to design the DC glow discharge experiments presented in Section 4.4. If these predictions are correct, the production of 10^{13} electron/cm^3 requires an electric field of ~1.35kV/cm, and a current density of ~10.4A/cm^2. Thus the power required to produce 10^{13} electrons/cc in air at 2000 K is approximately 14kW/cm^3.

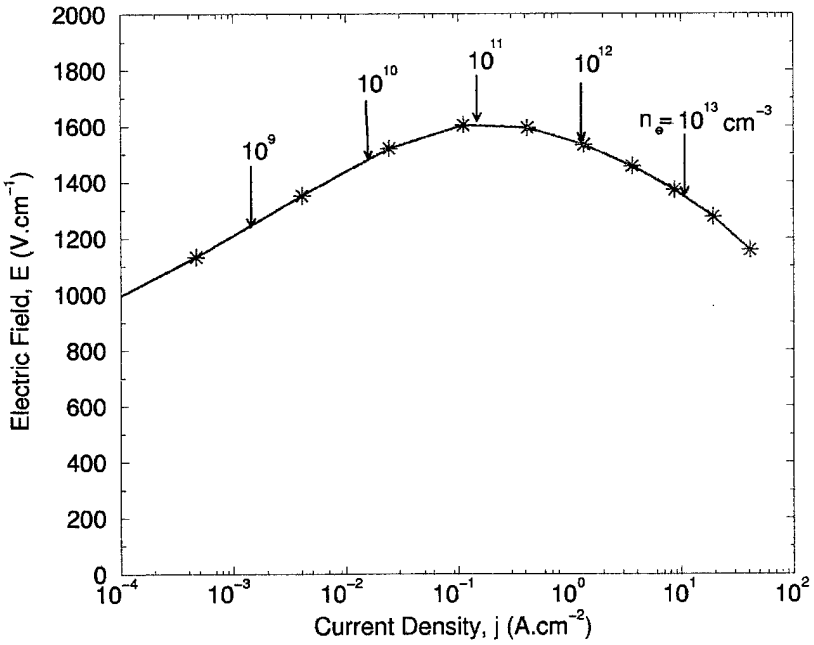

Figure 29. Predicted discharge characteristics for atmospheric pressure air at 2000 K.

density versus electric field, direct-current (DC) glow discharged have been produced in flowing low temperature, atmospheric pressure air plasmas. The flow velocity is around 400 m/s, and the gas temperature is varied between 1800 and 2900 K. These experiments show that it is feasible to create stable diffuse glow discharges with electron number densities in excess of 10^{12} cm^{-3} in atmospheric pressure air plasmas. Electrical characteristics were measured and the thermodynamic parameters of the discharge were obtained by spectroscopic measurements. The measured gas temperature is not noticeably affected by whether or not the DC discharge is applied. The discharge area was determined from spatially resolved optical measurements of plasma emission during discharge excitation. The measured discharge characteristics are compared in Section 4.5 with the predicted electrical characteristics.

4.4.2. DC discharge experimental setup

The ionization process in the discharge region is accompanied by energy transfer to the gas through collisions between electrons and heavy particles. Electrons lose more than 99.9% of the energy gained from the electric field to molecular N_2 through vibrational excitation, and the vibrationally excited N_2 transfers energy to translational modes through vibrational relaxation. Thus the degree of gas heating (ΔT_g) is a function of the volumetric power, jE, deposited into the plasma by the discharge and the competition of the vibrational relaxation time and the residence time τ of the plasma in the discharge region. To limit gas heating to acceptable levels for given volumetric power, it is desirable to flow the plasma at high velocity through the discharge region.

The experimental set-up is shown schematically in Figure 30. Atmospheric pressure air is heated with a 50 kW radio-frequency inductively-coupled plasma torch operating at a frequency of 4 MHz. A 2 cm exit diameter nozzle is mounted at the exit of the torch head. The flow rate injected in the torch was approximately 96 standard liters per minute (slpm) (64 slpm radial and 32 slpm swirl) and the plate power settings were 8.9 kV × 4.1 A, with approximately 14 kW of power deposited into the plasma. Under these conditions, the temperature of the plasma at the exit of the 2 cm diameter nozzle is about 5000 K and its velocity is ~ 100 m/s.

power deposited into the plasma. Under these conditions, the temperature of the plasma at the exit of the 2 cm diameter nozzle is about 5000 K and its velocity is ~ 100 m/s.

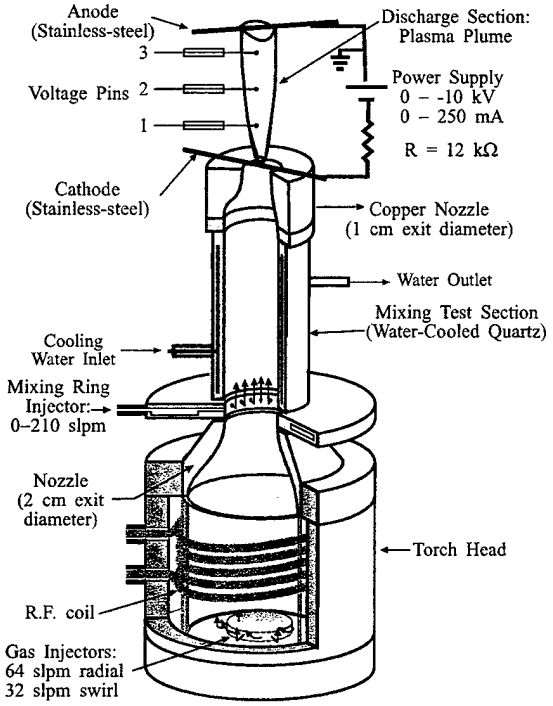

Figure 30. Set-up (not to scale) for discharge experiments showing the torch head, the injection ring, the 2-cm diameter, 18-cm long water-cooled quartz mixing test-section, the 2 → 1 cm converging nozzle, electrodes, voltage pins, and electrical circuit.

The plasma then enters a quartz test-section where it is cooled to the desired temperature by mixing with an adjustable amount of cold air injected into the plasma stream through a radial mixing ring. The quartz test-section length of 18 cm ensures that the flow residence time (approximately 1.6 ms here) is greater than the characteristic time for chemical and thermal equilibration of the plasma (< 1ms). Thus at the exit of the quartz test-section the air flow is close to Local Thermodynamic Equilibrium (LTE) conditions. Finally, a 1 cm exit diameter converging water-cooled copper nozzle is mounted at the exit of the mixing test-section. This nozzle is used to control the velocity, hence the residence time, of the flow within the discharge region. Two-dimensional computational fluid dynamics (CFD) calculations performed at the University of Minnesota show that the axial velocity at the entrance of the discharge region is approximately 445 m/s [55]. The discharge itself is produced between two platinum pin electrodes of 0.5 mm diameter held along the axis of the air stream by two water-cooled 1/16" stainless-steel tubes placed crosswise to the plasma flow. The bottom electrode is mounted on the copper nozzle and

The discharge was driven by a Del Electronics Model RHSV10-2500R power supply with reversible polarities, capable of operation in control current or control voltage mode, with current and voltage outputs in the ranges of 0 – 250 mA and 0 – 10 kV, respectively. For the present experiments, the cathode (bottom electrode) was biased to negative potentials with respect to ground.

The electric field within the discharge region is measured from the potential on a high purity platinum wire (0.02 inch diameter) that extends to the center of the discharge region. The platinum wire is held by a small ceramic tube installed on a two-way (horizontal and vertical) translation stage. Horizontal translation moves the pin into the discharge region for electric field measurements, and out of the discharge during spectral emission measurements. Vertical translation moves the pin along the discharge axis to determine the electric field from potential measurements. Although pure platinum melts at ~ 2045 K, radiation cooling prevents melting of the platinum wires for plasma temperatures up to at least 3000 K. The voltage measurements reported here were made with a Tektronix Model P6015A high voltage (20 kV DC, 40 kV peak pulse) probe and a Hewlett Packard Model 54510A, digitizing oscilloscope. The current was measured from the voltage drop across the 12 kΩ ballast resistor of the DC circuit.

The setup for optical emission spectroscopy diagnostics includes a SPEX model 750M, 3/4 meter monochromator fitted with a 1200 lines/mm grating blazed at 200 nm and a backthinned Spectrum One thermoelectrically cooled charge-coupled device (CCD) camera. The 30 × 12 mm CCD chip contains 2000 × 800 pixels of dimension 15 × 15 μm. The dispersion of the optical system is ~ 1.1 nm/mm. The monochromator entrance slit width was set at 200 μm, and 26 columns of 800 pixels were binned to produce an equivalent exit slit width of 390 μm. The spatial resolution was ~ 0.5 mm as determined by the monochromator entrance slit width and the magnification of the optical train (2.5 for two lenses of focal length 50 and 20 cm). Absolute spectral intensity calibrations were obtained with an Optronics model OL550 tungsten filament lamp and a 1 kW argon arcjet, with radiance calibrations traceable to National Institute of Standards and Technology (NIST) standards.

4.4.3. Spectroscopic Measurements

4.4.3.a. Measurements without DC discharge applied

The gas temperature (rotational temperature) without DC discharge applied was measured by emission spectroscopy of the OH ($A \rightarrow X$) transition. The OH ($A \rightarrow X$) transition is one of most intense emission systems in low temperature ($T \leq 4000$ K) air plasmas containing even a small

4.4.3. Spectroscopic Measurements

4.4.3.a. Measurements without DC discharge applied

The gas temperature (rotational temperature) without DC discharge applied was measured by emission spectroscopy of the OH ($A \rightarrow X$) transition. The OH ($A \rightarrow X$) transition is one of most intense emission systems in low temperature ($T \leq 4000$ K) air plasmas containing even a small amount (~ 1%) of H_2 or H_2O. In the present experiments, the water content of the air injected into the torch was sufficient to produce intense OH radiation. Rotational temperatures can be obtained from the relative intensities of two groups of rotational lines , corresponding to the R (R_1 and R_2) and P (P_1 and P_2) branches of the (0,0) vibrational band, that form distinct peaks at 306.8 and 309.2 nm, respectively. Figure 31 shows a simulation of the OH $A \rightarrow X$ bands obtained with the NEQAIR2 radiation code [1] which incorporates an accurate model for this transition [56]. One advantage of this rotational temperature measurement technique is that it does not require the measured signal to be corrected for the spectral intensity response of the detection system because the response of the detection system used is nearly constant over the less than 3 nm spectral range of interest. The relative intensity of the two peaks is fairly sensitive to the rotational temperature, as can be seen from Figure 32.

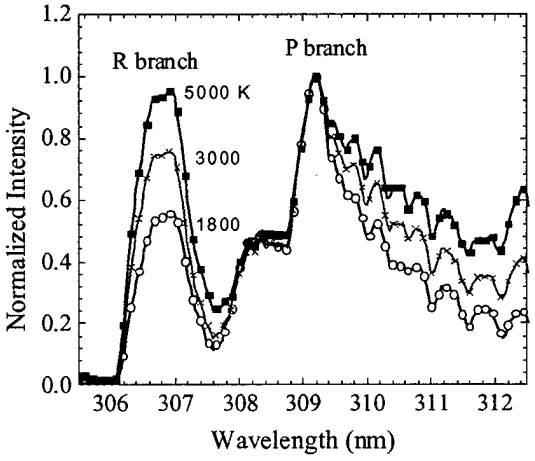

Figure 31. NEQAIR2 simulations of the OH $A \rightarrow X$ emission spectrum as a function of temperature in LTE air, normalized to the peak of the P branch.

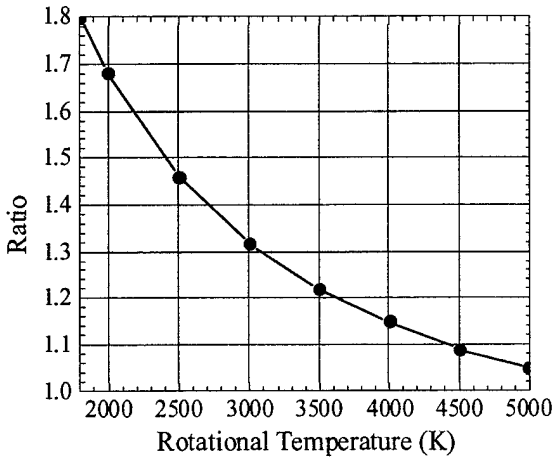

Figure 32. Intensity ratio of the P/R band head as a function of the rotational temperature (NEQAIR2 simulations for an instrumental slit function of of HWHM=0.21 nm).

Line-of-sight OH emission spectra were recorded with the discharge off. The amount of cold air mixing was adjusted to vary the temperature of the preheated air. The measured OH spectra were later fitted with NEQAIR2. As shown in Figure 33, the gas temperature can be varied from 1800 to 2900 K by adjusting the amount of cold air mixing.

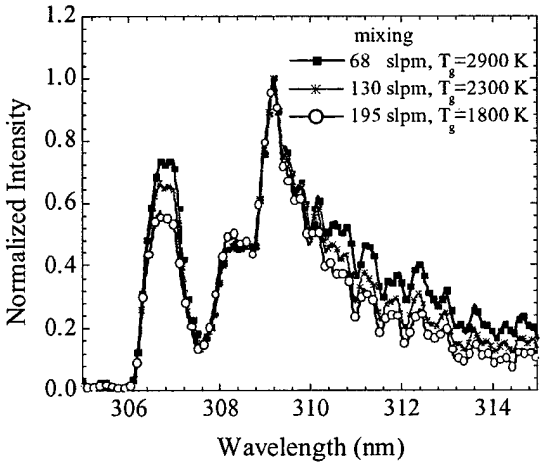

Figure 33. Measured OH $A \rightarrow X$ emission spectra without discharge applied as a function of the amount of cold air mixing.

Absolute spectral measurements were made of plasma emission between 200 and 400 nm in order to verify that the preheated air is chemical or thermal equilibrium. Comparisons are shown in Figure 34 with spectral simulations made with the NEQAIR2 code, assuming LTE conditions, and using the measured temperature profile and corresponding equilibrium concentrations for the case of 145 slpm mixing cold air. As can be seen from Figure 34, the numerical LTE simulations reproduce the experimental spectrum both in shape and absolute

duce the experimental spectrum both in shape and absolute intensity, thus indicating that the pre-heated air (with no discharge applied) is close to LTE. Thus the electron number density should be close to the equilibrium value when the discharge is not applied. At 2000 K for instance, this equilibrium value is ~3×10^6 cm^{-3}.

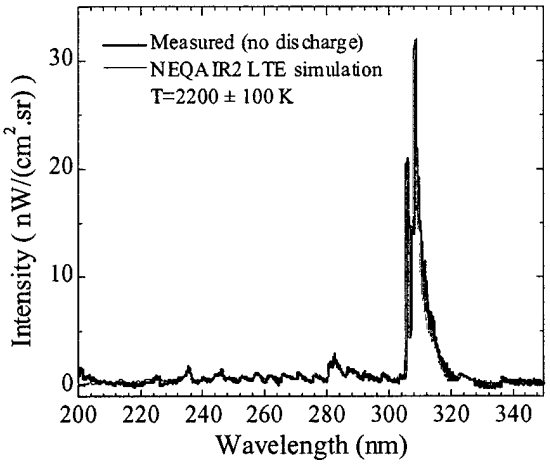

Figure 34. Measured emission spectra without discharge applied, and comparisons with NEQAIR2 spectral simulations assuming LTE.

4.4.3.b. Measurements with DC discharge applied

Emission spectra were also measured with the discharge applied (discharge current of 150 mA), and results are shown in Figure 35. As can be seen in the figure, a factor of ~ 10^4 enhancement of the emission due to NO gamma ($A \rightarrow X$) and a factor of ~ 10^5 enhancement of the emission due to N_2 ($C \rightarrow B$) bands were observed. Figure 35 also shows that the N_2 second positive system ($C \rightarrow B$) bands overlap the OH ($A \rightarrow X$) feature around 308 nm. This overlap precludes the accurate measurements of the rotational temperature from the OH ($A \rightarrow X$) transition. Therefore the gas temperature (rotational temperature) was measured by means of emission spectroscopy of the (0,0) band of the N_2 second positive system – the N_2 ($C \rightarrow B$) transition. Line-of-sight N_2 emission spectra were recorded along lateral chords of the plasma. The spectra were fitted with NEQAIR2 to obtain a rotational temperature T_r. Figure 36 shows a typical experimental spectrum and NEQAIR2 fit for 150 mA discharge current and 145 slpm of cold air mixing.

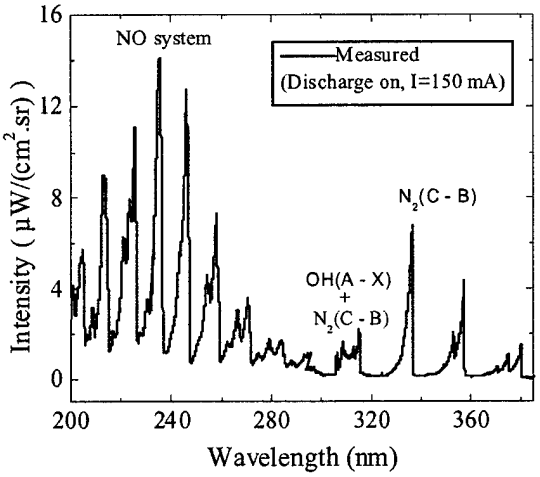

Figure 35. Line-of-sight emission spectra measured at a discharge current I = 150 mA.

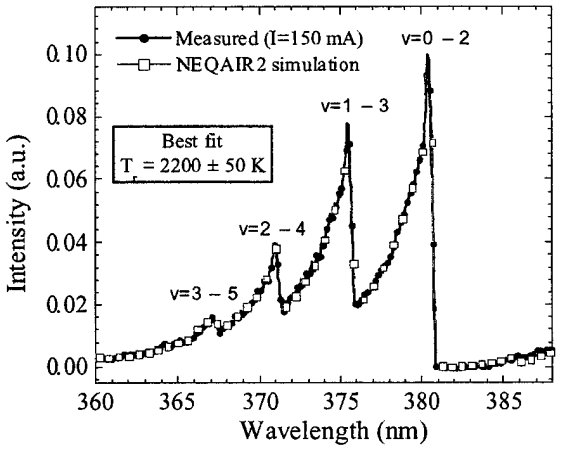

Figure 36. Emission Spectrum of N_2 second positive($C \rightarrow B$) bands and comparisons with NEQAIR2 spectral simulations.

The vibrational structure of the N_2 second positive ($C \rightarrow B$) system can be used to determine the vibrational temperature of the C state. As shown in Figure 36, the (0,2), (1,3), (2,4) and (3,5) vibrational sequences were utilized here. By matching NEQAIR2 spectra (calculated with $T_r = T_{r,measured}$) to the shape of the measured (0,2), (1,3), (2,4) and (3,5) bands spectra, the N_2 C state vibrational temperature $T_{v,measured}$ was obtained.

The absolute intensity of the spectrum can then be used to determine the population of the N_2 C electronic state. As discussed in Ref. [1], the integrated intensity of a spectral line is defined as

$$I\left[\mathrm{W/cm^3/sr}\right] = \frac{n_u A_{ul} \Delta E_{ul}}{4\pi}, \qquad (25)$$

where A_{ul} (s^{-1}) is the Einstein A coefficient representing the probability of a radiative transition from level u to level l, ΔE_{ul} is the energy difference between the level u and l, and n_u is the population of electronic level u. The intensity of the transition gives a measurement of the number density of the upper electronic energy level, which can then be used to determine an electronic temperature T_{el} defined by the Boltzmann relation:

$$\frac{n_u}{n_0} = \frac{g_u}{g_0} \exp\left(\frac{-\varepsilon_u}{k_B T_{el}}\right), \tag{26}$$

where ε_u is the electronic energy of level u; k_B is Boltzmann's constant; n_0 is the population of the ground state; g_u and g_0 are the degeneracies of the upper and ground level, respectively.

The absolute (0,0) bandhead intensity I_{model} can be obtained from NEQAIR2 by assuming $T_r = T_{r,measured}$, $T_v = T_{v,measured}$, and $T_{el} = T_r$. Thus from equations (25) and (26) we obtain the measured N_2 C state electronic temperature $T_{el,N2(C)}$ via

$$\frac{I_{exp.}}{I_{model}} = \exp\left(\frac{-\varepsilon_u}{k_B}\left(\frac{1}{T_{el,N_2(C)}} - \frac{1}{T_r}\right)\right). \tag{27}$$

Additional discharge experiments were conducted with different gas temperatures. Figure 37 shows the measured N_2 second positive system spectra and their rotational and vibrational temperatures at a discharge current of 150 mA, as a function of the amount of mixing air. It can be seen in the figure that both the rotational and vibrational temperatures are lower with higher amount of mixing cold air. Figure 38 shows the measured spectrum as a function of the discharge current for 145 slpm of mixing air. As can be seen from the figure, the rotational temperature remains the same at all currents, but the vibrational temperature increases with increasing discharge current.

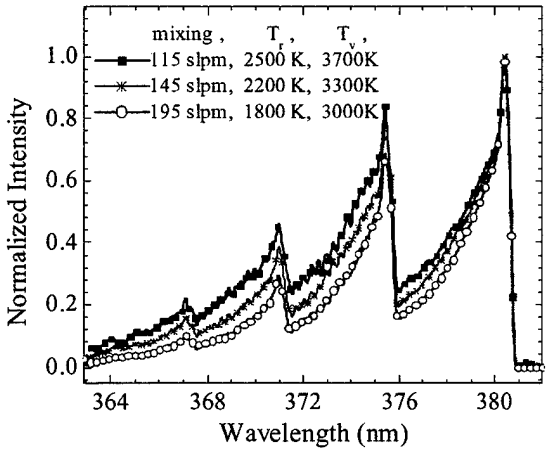

Figure 37. Measured N_2 second positive($C \rightarrow B$) bands with discharge on as a function of the amount of cold air mixing (I = 150 mA).

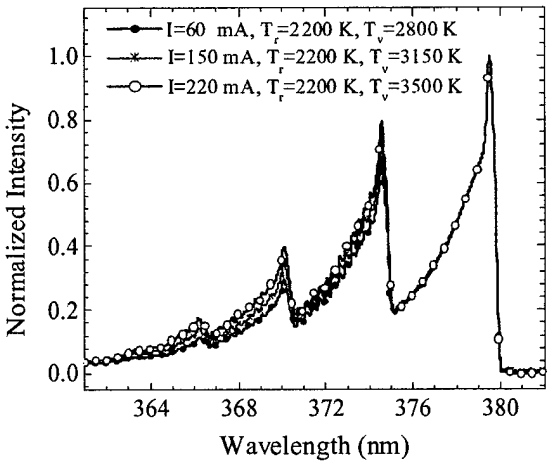

Figure 38. Measured N_2 second positive($C \rightarrow B$) bands with discharge on as a function of discharge current for the case of 145 slpm cold air mixing.

Radial rotational temperature profiles with and without the discharge applied were measured along chords of the plasma from Abel-inverted N_2 second positive system emission spectra and OH emission spectrum, respectively. Figure 39 shows the measured radial temperature profiles at a distance of 1.5 cm downstream of the cathode(i.e. along midway between the two electrodes). As can be seen from the figure, the applied discharge does not noticeably increase the rotational temperature of the plasma at this location. Figure 40 shows the radial N_2 C state electronic and vibrational temperature profiles. On the axis of the discharge, the electronic temperature of the N_2 C state reaches about 5000 K, and the vibrational temperature is about 3000 K.

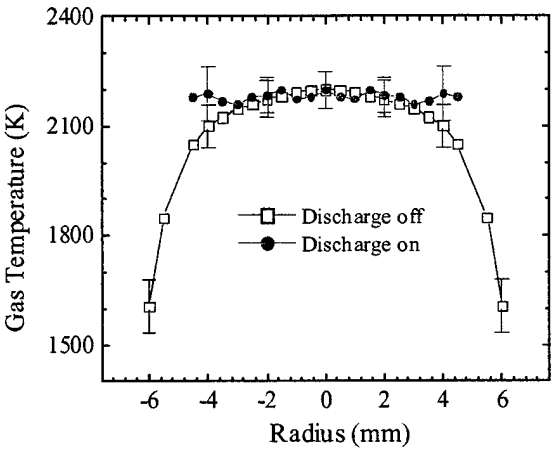

Figure 39. Rotational temperature profiles with and without the applied DC discharge at 1.5 cm downstream of the bottom electrode. The temperature profile without the discharge was measured from rotational lines of the OH ($A \rightarrow X$) transition. With the discharge applied, the rotational temperature was measured from lines of the N_2 ($C \rightarrow B$) transition in the ultraviolet.

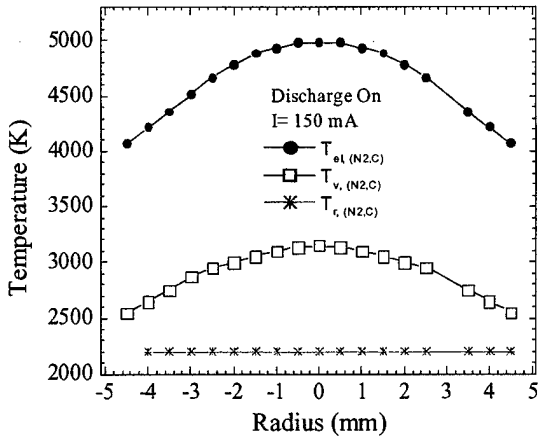

Figure 40. Electronic, vibrational and rotational temperature profiles of N_2 *C* state with an applied discharge current of *I* = 150 mA.

Figure 41a shows a photograph of the air plasma plume at a temperature of approximately 2200 K in the region between the two electrodes without the discharge applied. Figure 41b shows the same region when a DC discharge of 5.2 kV and 200 mA is applied between the two electrodes. In these experiments, the distance between electrodes is 3.5 cm. The bright region in Figure 41b corresponds to the discharge-excited plasma. Thus the plasma plume without discharge applied appears to be homogeneous over a larger diameter than the plasma plume with the discharge applied. However, Figure 39 showed that the gas temperature profile is practically the same as in the discharge applied case. The increased brightness in Figure 41b is due to the emission of excited electronic states of molecular NO and N_2 (see Figure 40). Thus the applied discharge increases excited state populations without significantly increasing the gas temperature.

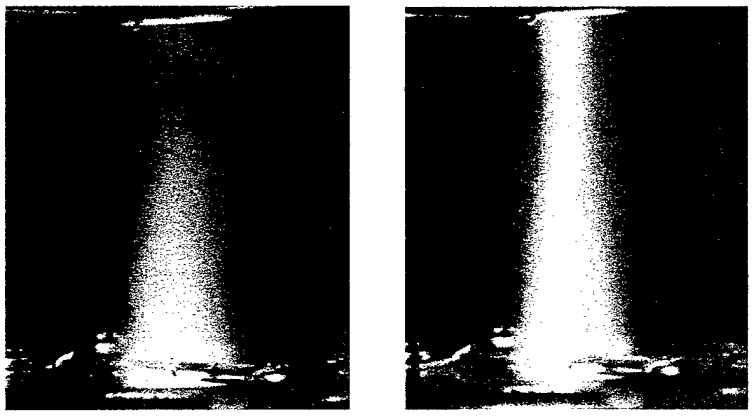

(a) (b)

Figure 41. (a) Air plasma at 2000 K without electrical discharge. (b) Air plasma at 2000 K with applied discharge (1.4 kV/cm, 200 mA). Interelectrode distance = 3.5 cm. The measured electron number density in the bright discharge region is around 10^{12} cm^{-3}.

4.4.4. Current Density Measurements

The current density at the center of the plasma was determined by dividing the measured current by the effective discharge area A^*, i.e. $j(r=0) = I/A^*$. The effective discharge area is obtained from the following relation,

$$\left[j(r=0) \times A^* \right] = \int_0^R 2\pi r j(r) dr \,, \tag{28}$$

where $j(r)$ is the local current density. As shown in Ref. [13], $j(r)$ is approximately proportional to $n_e(r)$. Thus, A^* can be calculated as

$$\mathrm{A}^* = \left(\int_0^R n_e(r) 2\pi r dr \right) \Big/ n_e(r=0) \ . \tag{29}$$

In separate discharge experiments conducted with a nitrogen plasma [57], the electron number density profile n_e was measured using various techniques (from H_β Stark broadening and N_2 1st positive emission spectra) to calculate A^* using Equation (29). The discharge area A^* was also estimated from the full width at half maximum (FWHM) of the N_2 $C-B$ (0,0) bandhead intensity profile. In these nitrogen discharge experiments, the effective area A^* obtained with Equation (29) and the measured n_e profile was found to be equal to the effective area obtained from the N_2 $C-B$ (0,0) emission intensity measurement. Thus for the present air plasma discharge experiments, we estimate the effective discharge area from the spatially resolved optical measurements of N_2 C state emission. Spectroscopic measurements of N_2 $C-B$ (0,0) emission with the applied discharge are shown in Figure 42. It can be seen from the figure that the diameter (FWHM) of the discharge is approximately 3.2 mm. This diameter was monitored and found to be constant for all discharge currents ranging from 5 to 250 mA. The discharge diameter was therefore taken to be 3.2 mm and assumed constant along the axis of the discharge.

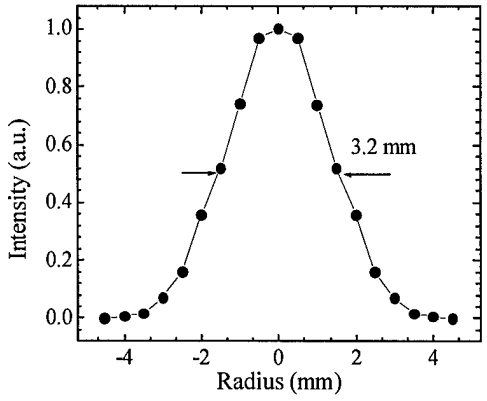

Figure 42. Spatial extent of the plasma produced by the discharge.

4.4.5. Electric Field Measurements

Electrode and pin potentials were measured as a function of the applied discharge current which was varied from 0 to 250 mA. The cathode current was measured from the voltage drop across the 12 kΩ ballast resistor placed in series with the discharge (see Figure 30). There is a small difference of 7 mA between the anode and the cathode currents that was found to be due to a current leak through the water cooling circuit of the anode. All results reported below are based on the measured cathode current, which is not affected by current losses to the cooling circuit.

Figure 43 shows the measured pin voltage as a function of the applied current along the axis of the discharge. The potential varies approximately linearly along the axis of the discharge, indicating that the electric field is approximately uniform in the discharge region. The electric field measurements reported here were determined from the slope of a linear fit of the pin potentials. In the vicinity of the cathodes, voltage falls of up to several hundred volts were observed. These values are typical of the cathode fall voltage in glow discharges [58].

The total voltage across the discharge was also measured as a function of electrode separation, by translating the top electrode (anode) vertically. The voltage-length characteristic for a discharge current of 150 mA is shown in Figure 44. The lowest voltage reading as the electrodes are brought within less than 0.2 mm from one another provides an approximation to the discharge voltage at zero gap length [59, 60]. The value of this voltage is found to be 285 V and is independent of the current in the current range investigated (10 – 250 mA). This value agrees with the cathode fall voltage reported in the literature [7, 61] for glow discharges in air with a platinum cathode. The voltage gradient in the positive column, given by the slope of the voltage-length characteristic, is constant as the discharge length is increased. For a discharge current of 150 mA, the gradient is about 1400 V/cm (see Figure 44) and is consistent with the electric field value determined from the pin measurements.

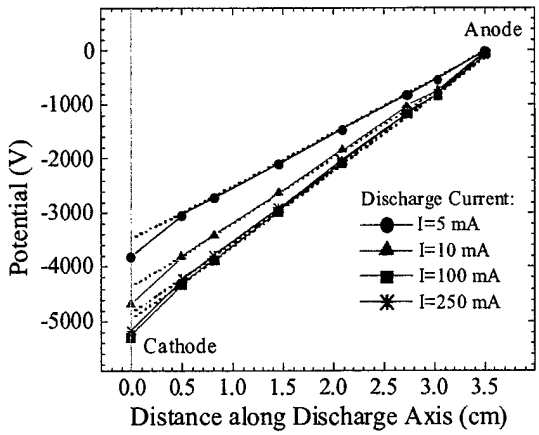

Figure 43. Measured potentials as a function of applied current in the discharge section.

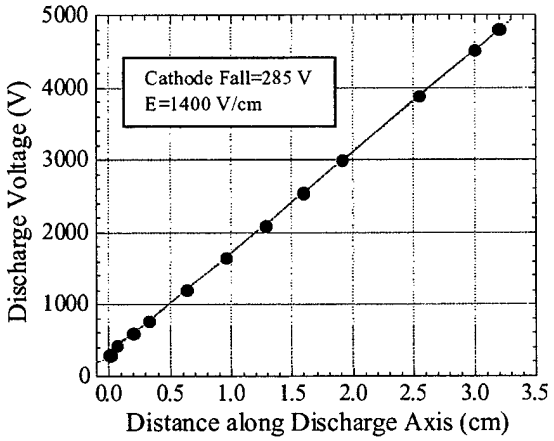

Figure 44. Voltage-length characteristic in the discharge region.

4.5. Electrical Characteristics and Power Requirements of DC Discharges in Air

The experimental discharge characteristics presented in Section 4.4 for plasma temperatures ranging from 1800 to 2900 K are shown in Figure 45. They are also compared with the predicted characteristics at the corresponding gas temperatures. The method employed to predict the discharge characteristics was discussed in Section 4.3. As can be seen from Figure 45, good agreement is obtained between the measured and predicted discharge characteristics over a range of experiments spanning over three orders of magnitude in current density.

Figure 45 also shows (dashed curve) the resistive characteristic of equilibrium air at 2900 K, given by the relation:

$$E = \frac{j}{\sigma_{equilibrium,2900K}}, \tag{30}$$

where $\sigma_{equilibrium,2900\,K}$, the electrical conductivity of equilibrium air at 2900 K, is calculated as:

$$\sigma_{equilibrium,2900K} = \frac{n_e^{equil,2900K} e^2}{m_e \bar{\nu}_{e-air}}, \tag{31}$$

where $n_e^{equil,2900K} = 4\times10^{10}$ cm^{-3} and the collision frequency $\bar{\nu}_{e-air}$ is well approximated by

$$\bar{\nu}_{e-air} = \left(\frac{p}{kT_g}\right) g_e \left(1.5\times10^{-15}\left[cm^2\right]\right), \tag{32}$$

where p is the pressure (1 atm), $T_g = 2900$ K is the gas temperature, and $g_e = \sqrt{8kT_e/\pi m_e}$ is the electron thermal velocity. For $T_g = 2900$ K, as can be seen from Figure 45 the predicted E vs. j characteristic is close to the resistive equilibrium characteristic for current densities below 0.2 A/cm^2. In this current density range, the predicted electron temperature remains below approximately 8000 K and electron-impact reactions are inefficient in ionizing the plasma. Thus the electron number density increases only by a few percent. As the electron temperature increases, the frequency of collisions increases with $\sqrt{T_e}$, resulting in a decrease of the electrical conductivity of the plasma. This explains why the E vs. j characteristic is higher than the resistive equilibrium characteristic for j below ~0.2 A/cm^2. At higher values of the current density, where the discharge produces a significant increase in the electron density, the conductivity increases dramatically and the slope of the E vs. j characteristic decreases. Thus the region to the right of the resistive equilibrium characteristic is where the discharge increases the electron number density. The experimental data at T_g between 1800 K and 2900 K all show the turning trends of the non-resistive discharge characteristics. We note however that the predicted resistive part appears to be shifted to lower current densities relative to the experimental curves. This difference may be due to the fact that the electron number density was slightly above the equilibrium value in the incoming air stream. We recall that the "equilibrium" air was produced by cooling of an air stream initially heated to high temperatures. Slow electron recombination could therefore explain the differences at low current densities.

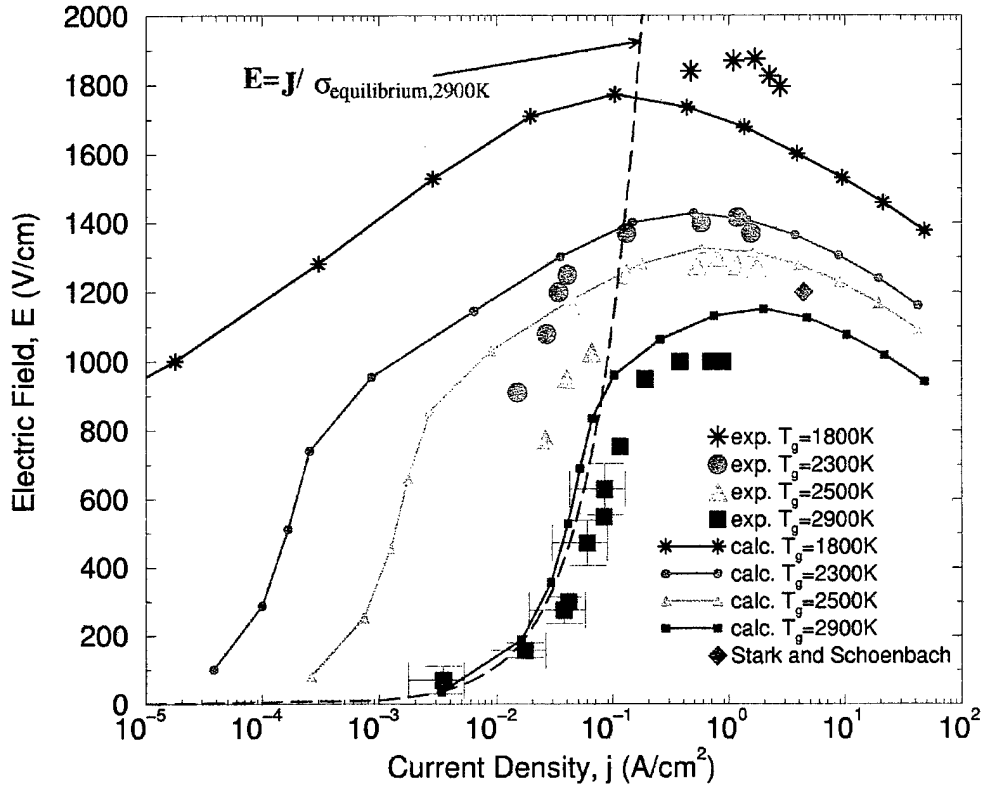

Figure 45. Measured (symbols) and predicted (solid lines) electrical discharge characteristics in atmospheric pressure air plasmas generated by DC electric discharges.

Figure 45 also shows experimental data obtained by Stark and Schoenbach [62] in an atmospheric pressure glow discharge in air. The discharge was produced between a microhollow cathode and a positively biased electrode, as described in Ref. [63]. The gas temperature was measured to be around 2000 K, and the center electron number density is reported to be above 10^{12} cm^{-3} [62, 64]. This measurement adds further support to the kinetic mechanism predictions.

We conclude this section with the power required to produce a given electron density in air at 2000 K by means of DC glow discharges. The results are shown in Figure 46. We predict that the production of 10^{13} electron/cm^3 in air at 2000 K requires about 14kW/cm^3. The corresponding electric field is ~1.35kV/cm, and the current density is ~10.4A/cm^2, as shown earlier in Figure 29.

This level of Joule heating may not lead to significant overall gas heating in small scale stationary DC discharges where conduction to ambient air and to the electrodes is high. This was the case for instance in Gambling and Edels's experiments [60] where the positive column was a few

millimeters in length and approximately 0.2 mm^2 in area. In larger volume DC discharges, however, it is necessary to control the effect of Joule heating of the gas, for instance by flowing the gas through the discharge at high velocities. For air at 2000 K flowing through a 1 cm diameter region of length 3.5 cm at a velocity of 450 m/s, the residence time is 78 μs. The vibrational relaxation times τ reported by Park [10] indicate that the fastest vibrational relaxation rate of molecular N_2 is through collisions with atomic oxygen. The rate constant is given by $p_0\tau = 10^{-6}$ (atm.s), where p_0 is the partial pressure of atomic oxygen. In our discharge experiments, the atomic oxygen mole fraction is less than 1%, according to our two-temperature kinetic model predictions. Thus, the vibrational relaxation time τ (> 100 μs) is larger than flow time (78 μs). This is consistent with the observation that we observed little gas heating in the experiments. To limit gas heating to acceptable levels for a given volumetric power, it is desirable to flow the plasma at high velocity through the discharge region.

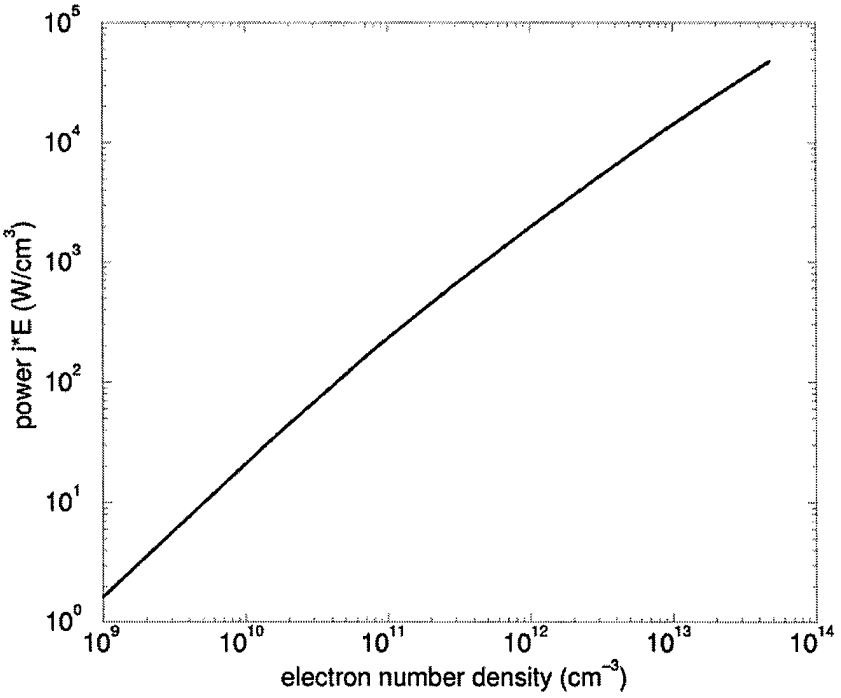

Figure 46. Power required to produce an elevated electron density in atmospheric pressure air at 2000 K by means of DC discharges.

4.6. DC Discharges in Nitrogen

Discharge experiments were also conducted with atmospheric pressure nitrogen either at room temperature or preheated to temperatures between 1800-2250 K [57]. For the room temperature experiments, nitrogen is injected between the electrodes at a velocity of about 2 m/s. The gas heats up to temperatures between 2200 and 2800 K as a result of discharge-induced Joule heating. For the experiments with preheated nitrogen, the gas is injected at about 450 m/s. Owing to the relatively fast flow rate, the gas temperature remains practically constant in the discharge region. The discharge diameter is about 1.7 mm in the room temperature nitrogen experiments, and 5 mm in preheated nitrogen. The difference in discharge diameters is due to the larger radial thermal gradients in cold nitrogen than in the preheated flow. In all cases the measured cathode fall is about 300 V , which is typical of a glow discharge. The measured discharge characteristics are shown in Figure 47, along with the characteristics calculated with the nitrogen CR model. As shown in Figure 47, the measured characteristics support the results of the chemistry and discharge models.

The foregoing calculations were performed using Maxwellian distribution functions for the translational energies of the electrons and heavy particles. To investigate the limitations of this simplification, the electron Boltzmann equation was solved for nitrogen plasmas in conjunction with a somewhat simplified form of the collisional-radiative model [57]. The results, shown in Figure 48, do not differ significantly from those with the Maxwellian version.

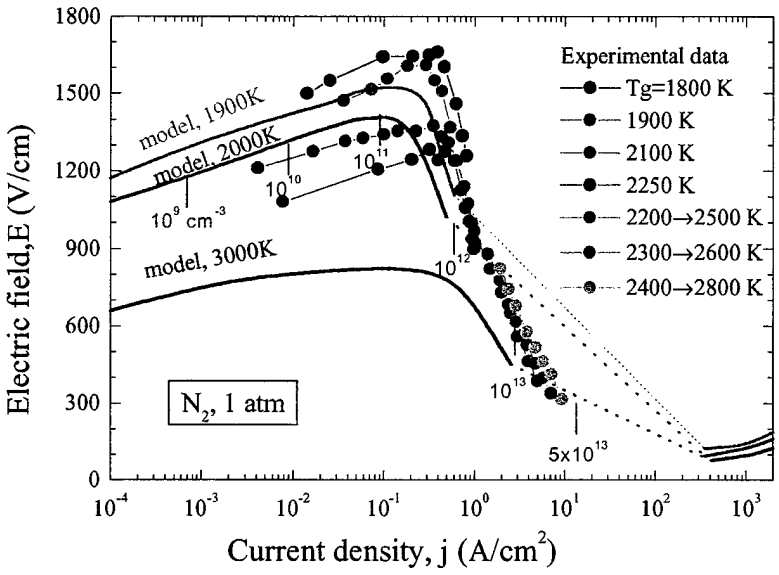

Figure 47. Measured (symbols) and predicted DC discharge characteristics in nitrogen at 1 atm.

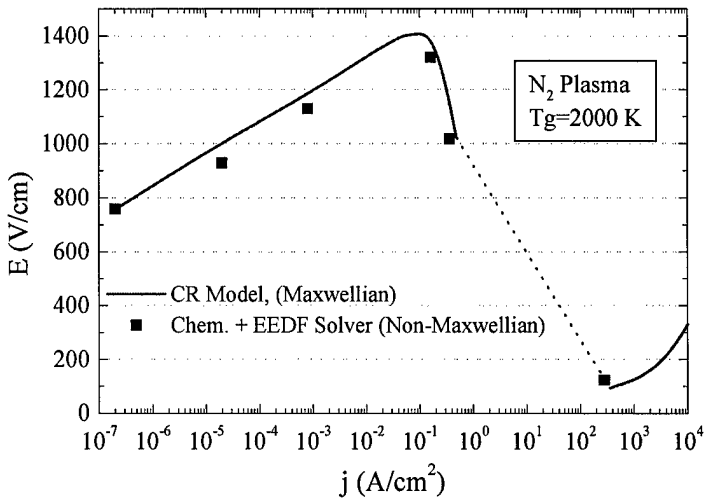

Figure 48. Predicted discharge characteristics in atmospheric pressure nitrogen at 2000 K.

4.7. Conclusions

Investigations have been made of the mechanisms of ionization in two-temperature air plasmas with electron temperatures elevated with respect to the gas temperature. Numerical simulations of these mechanisms yield the notable result that the electron number density exhibits an S-shape dependence on the electron temperature at fixed gas temperature. This S-shaped behavior is caused by competing ionization and charge transfer reactions. The characteristic of electric field vs. current density also exhibits a non-monotonic dependence.

Discharge experiments were conducted in air at atmospheric pressure and temperatures ranging from 1800 to 3000 K. In these experiments, a DC electric field was applied to flowing air plasmas with electron concentrations initially close to equilibrium. These experiments have shown that it is possible to obtain stable diffuse glow discharges in atmospheric pressure air with electron number densities of up to 2.5×10^{12} cm^{-3}, which is up to six orders of magnitude higher than in the absence of the discharge The value of 2.5×10^{12} cm^{-3} corresponds to the maximum current that can be drawn from the 250 mA power supply used in these experiments. The diffuse discharges are approximately 3.5 cm in length and 3.2 mm in diameter. No significant degree of gas heating was noticed as the measured gas temperature remained close to its value without the discharge applied. Results from these experiments are in good agreement with the predicted E vs. j characteristics. Additional comparisons were made with results from glow discharge experiments in atmospheric pressure ambient air by Gambling and Edels [60] and Stark and Schoenbach [62]. The measurements of these authors are also consistent with the predicted E vs. j characteristics. As these meas-

urements were made in the reactive region of the E vs. j curve, they support our proposed mechanism of ionization for two-temperature air.

As the power budget for DC electron heating is higher than desired for the practical use of air plasmas in many applications, methods to reduce the power budget were explored in our laboratory. Based on the predictions of our chemical kinetics and electrical discharge models, we have found that a repetitively pulsed electron heating strategy can provide power budget reductions of several orders of magnitude with respect to DC electron heating. Repetitively pulsed discharges are the object of Section 5 of this report.

5. Repetitively Pulsed Discharges in Air

5.1. Introduction

As the power required to sustain elevated electron densities with DC discharges is large, a power reduction strategy based on pulsed electron heating, proposed in our 1999 MURI Annual Progress Report, was explored. This strategy is illustrated in Figure 49. Short voltage pulses are applied to increase the electron number density. After each pulse, n_e decreases according to electron recombination processes. When n_e reaches the minimum desired value, a second pulse is applied. The average electron density obtained with this method depends on the pulse duration, pulse voltage, and the interval between pulses. Since power is not expended during the recombination period, the time averaged power will be greatly reduced if the pulse time is much smaller than the recombination time.

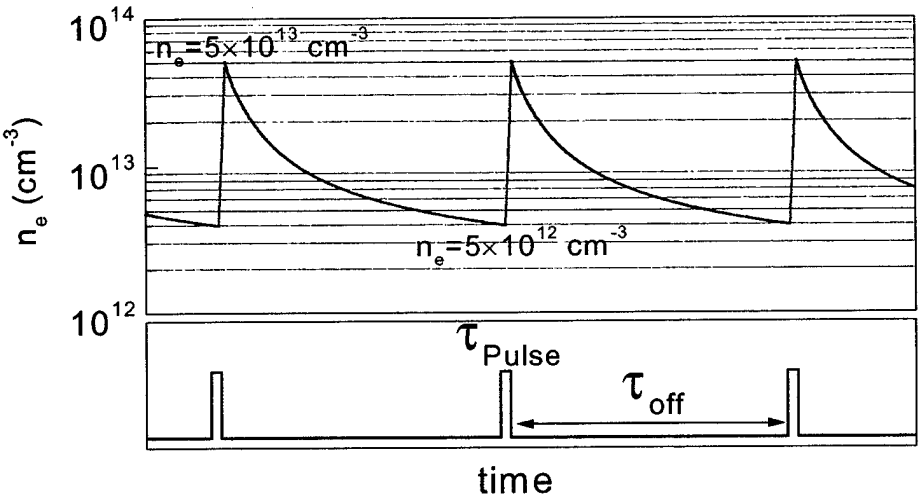

Figure 49. Repetitively pulsed strategy.

As seen in Section 4, DC discharges can maintain $n_e \geq 10^{12}$ cm^{-3} in atmospheric pressure air with electric fields producing an electron temperature on the order of 1eV. To produce the same average electron density with short (1-10ns)-pulsed discharges, a higher electron temperature of about 3-5 eV is required. Although the corresponding field is higher than for a DC discharge, the ionization efficiency is larger in the pulsed case than in the DC case because the energy lost to nitrogen molecules, per electron created, is smaller at T_e=3-5 eV than at 1 eV. This coupled with the finite electron recombination time allows the power budget to be dramatically reduced with pulsed discharges.

Figure 50 shows the predicted inelastic energy losses of electrons by collisions with N_2, per unit number density of N_2 and electrons. The losses to nitrogen represent the main fraction of the losses in air. This is because at electron temperatures below ~20,000 K the resonant e-V transfer in ground state N_2 is by far the dominant loss channel (there is no such resonant channel for O_2 or NO). At electron temperatures above 30,000 K, the inelastic losses are dominated by electron-impact electronic excitation, dissociation, and ionization, and the total losses per unit number density of N_2 and electrons are about the same as the total losses per unit number density of O_2 and electrons. Nitrogen losses dominate at $T_e > 20{,}000$ K because the density of N_2 is much higher than the density of O_2. Figure 50 shows that the power into ionization represents an increasingly large fraction of the total power as the electron temperature is increased.

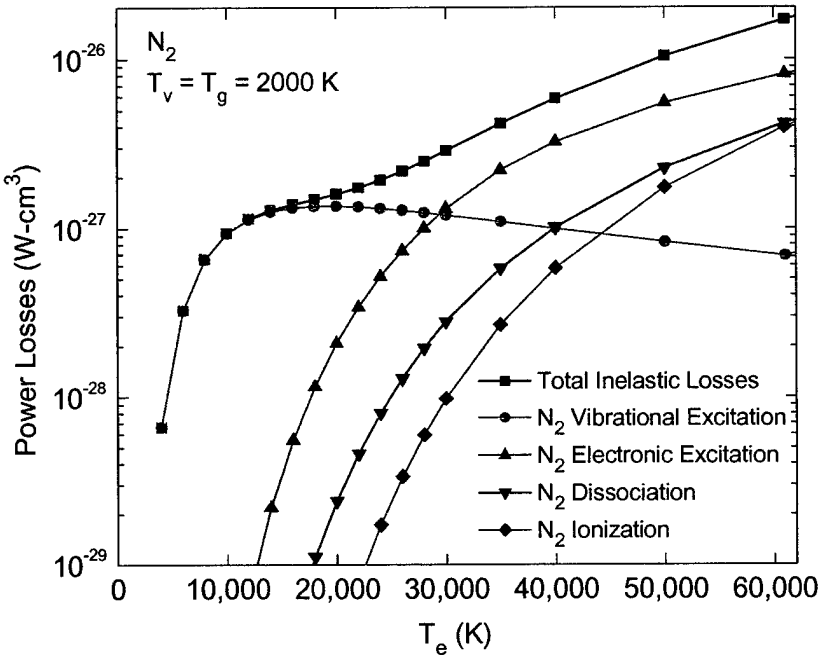

Figure 50. Inelastic power losses by electron-impact vibrational excitation, electronic excitation, dissociation, and ionization of N_2. In these calculations, the vibrational temperature is fixed equal to the gas temperature (T_v=T_g =2000 K), and the electronic temperature of internal energy levels is fixed equal to the electron temperature.

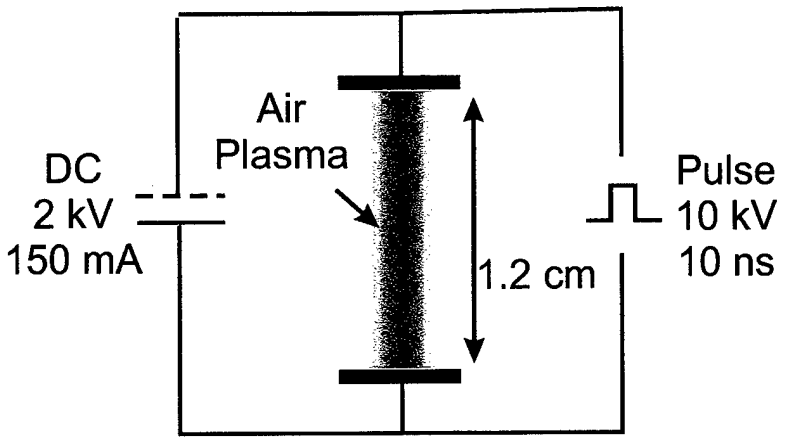

Figure 51. Schematic of the combined pulsed and DC discharge experiments.

5.2. Experiments with a Single Pulse

To test the pulsing scheme, experiments were conducted [65] in atmospheric pressure, 2000 K air using a pulse forming line capable of generating a 10 ns rectangular pulse with peak voltage up to 16 kV. To experimentally simulate the conditions of a repetitively pulsed discharge, the initial elevated electron number density generated by the "previous" pulse is created by means of a DC discharge in parallel with the pulser. The circuit schematic is shown in Figure 51. With a DC voltage of 2 kV and current of 150 mA, the initial electron density is 6.5×10^{11} cm^{-3}. A 10 kV, 10 ns pulse is superimposed to further increase the electron density. The measured discharge diameter of about 3 mm is comparable with the diameter of the DC discharge (Figure 52). The temporal variation of plasma conductivity was measured from the voltage across the electrodes and the current density through the plasma. The electron density increases from 6.5×10^{11} to 9×10^{12} cm^{-3} during the pulse, then decays to 10^{12} cm^{-3} in about 12 μs (Figure 53). The average measured electron density over the 12 μs duration is 2.8×10^{12} cm^{-3}.

Figure 53 shows a comparison of the measured electron number density with the predictions of our two-temperature model. The predictions agree well with the measured electron decay time of 12 μs. This decay time is consistent with the dissociative recombination time of NO^+ predicted to be 8.7 μs without the DC background. Thus these results provide validation of our chemical kinetic model of the recombination phase.

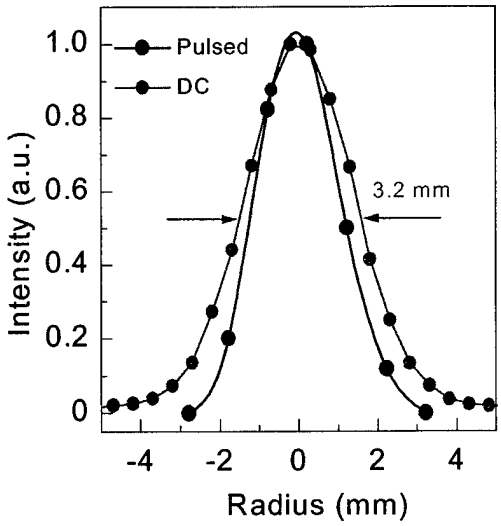

Figure 52. Spatial extent of the plasma produced with pulsed and DC discharges.

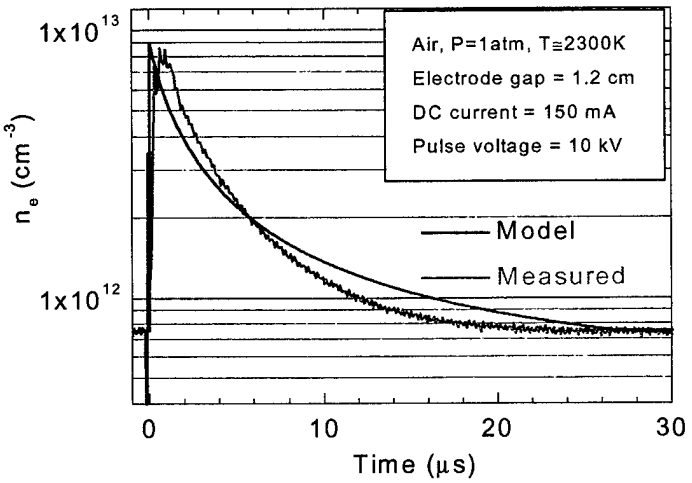

Figure 53. Temporal electron density profile in the 10 ns pulsed discharge

5.3. Experiments with 100 kHz Repetitive Discharge

The success of the proof-of-concept experiments conducted with the single pulse discharge led us to investigate the generation of air plasmas with a repetitively pulsed discharge. A repetitive pulser capable of generating 10 ns pulses, with peak voltages of 3-12 kV and pulse repetition frequencies up to 100 kHz was acquired from Moose-Hill/FID Technologies. This pulser operates with a solid-state opening switch or Drift-Step Recovery Diode (DSRD). The experimental set-up is shown in Figure 54 and the electric circuit in Figure 55. The discharge is applied to preheated, LTE air at atmospheric pressure and about 2000 K. The DC circuit in parallel with the pulser was used

only to determine the electron number density from the plasma conductivity. In regular operation, the DC circuit is disconnected and the discharge operated with the pulser only.

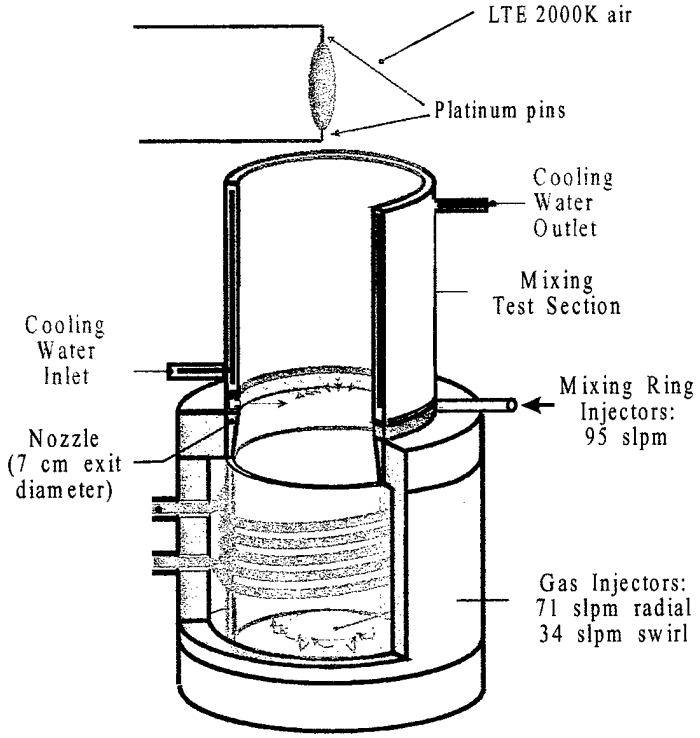

Figure 54. Set-up for repetitive pulse discharge in air at 2000 K, 1 atm.

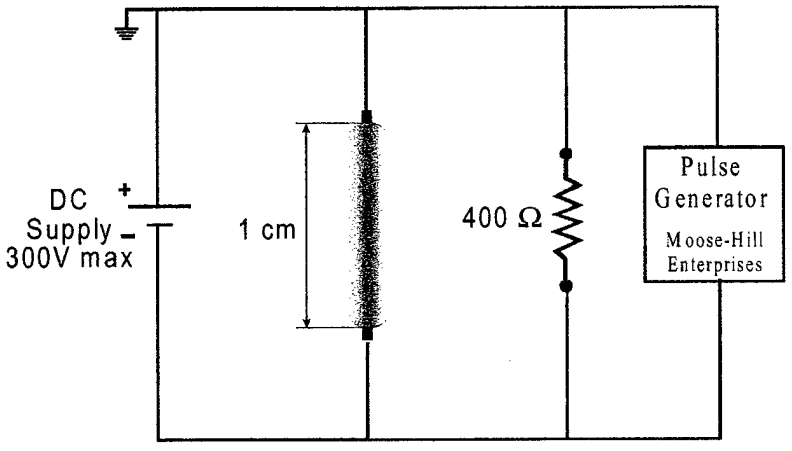

Figure 55. Repetitive pulse discharge circuit schematic (DC circuit applied only for conductivity measurements).

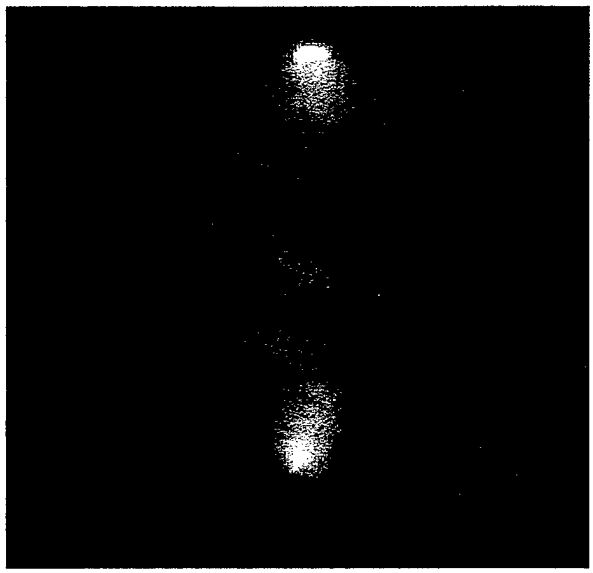

Figure 56. Photograph of 10 ns, 100 kHz repetitive pulse discharge in air at 2000 K, 1 atm.

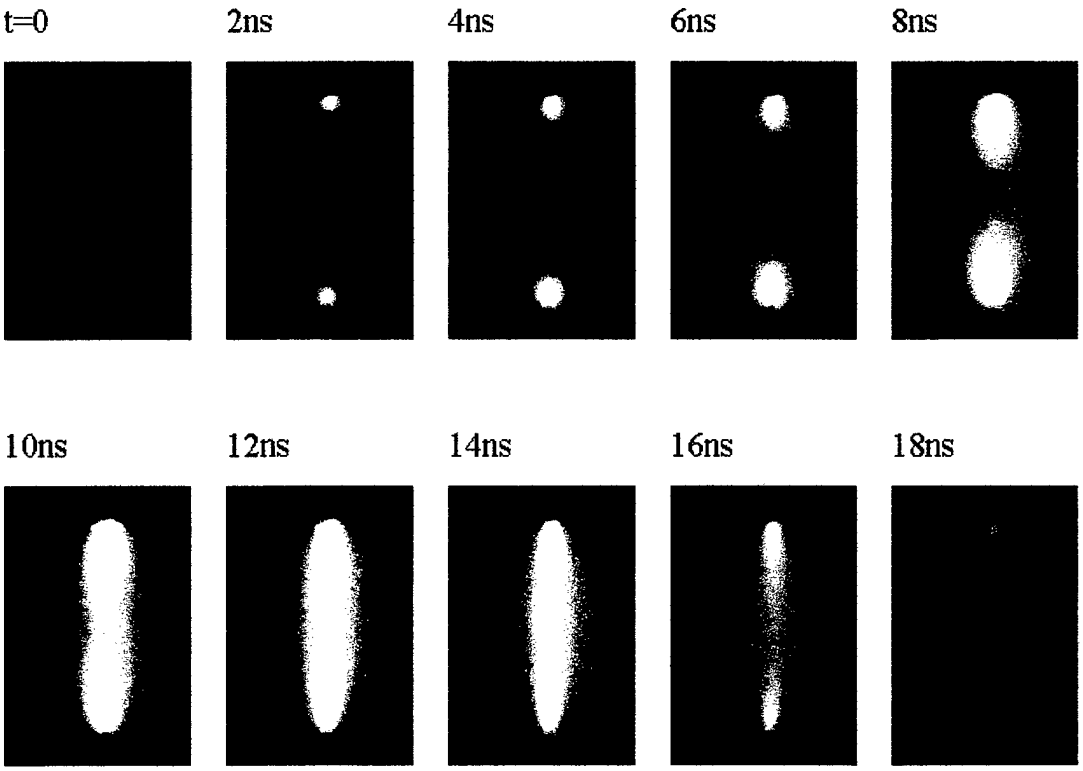

Figure 57. Time-resolved images of 10 ns pulsed discharge in air at 2000 K, 1 atm.

A photograph of the repetitively pulsed discharge in operation in atmospheric pressure pre-heated (2000 K) air is shown in Figure 56. The diffuse character of the discharge was confirmed with time-resolved (1.5 ns frames every 2 ns) measurements of plasma emission during the pulse (see Figure 57). These measurements were made with a high-speed intensified camera, Roper Scientific PI-MAX1024. The diameter of the discharge is approximately 3.3 mm. Additional time- and spectrally-resolved measurements of emission during the pulse and the recombination phase show that the pulse excites the C state of N_2 and the A state of NO. After the pulse, emission from the C state of N_2 decays to a constant value within 30 ns, and emission from the A state of NO shows a two-step decay, with first an abrupt decrease by over four orders of magnitude from the end of the pulse until 320 ns after the pulse, and then a slower decrease by one order of magnitude until the next pulse.

Figure 58 shows the measured temporal variations of the electron density during three cycles of the pulsed discharge. The electron number density varies from 7×10^{11} to 1.7×10^{12} cm^{-3}, with an average value of about 10^{12} cm^{-3}. The power deposited into the plasma by the repetitive discharge was determined from the pulse current (measured with a Rogowski coil), the voltage between the electrodes (6 kV peak) minus the cathode fall voltage (measured to be 1525 V by varying the gap distance), and the measured discharge diameter. The peak pulse current was 240 mA. The power deposited is found to be 12 W/cm^3, consistent with the theoretical value of 9 W/cm^3 for an optimized pulsed discharge producing 10^{12} electrons/cm^3. It is lower, by a factor of 250, than the power of 3000 W/cm^3 required to sustain 10^{12} electrons/cm^3 with a DC discharge.

More details about these experiments and modeling can be found in Ref. [66]. In this reference, a study was made of the effect of the pulse repetition frequency. Experiments were conducted with repetition frequencies of 30 and 100 kHz. In both case the power requirements were close to 10 W/cm^3 for about 10^{12} electrons/cm^3. The main difference between the plasmas produced is the amplitude of electron density variations. In the 30 kHz discharge, the amplitude varies by about a factor of 10, whereas in the 100 kHz the amplitude varies by a factor of two only.

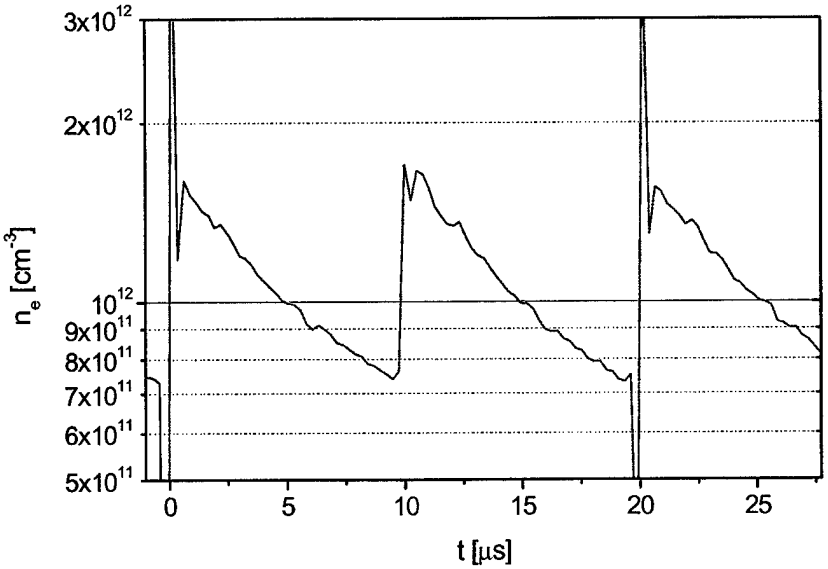

Figure 58. Electron number density measurements in the repetitive pulse discharge in air at 1 atm, 2000 K.

The results of our research on DC and pulsed electrical discharges are summarized in Figure 59, which shows the power required to generate elevated electron number density in 2000 K, atmospheric pressure air, with DC and pulsed discharges. The experimental point represents the measured power requirement of our repetitively pulsed discharge experiment. Power budget reductions by an additional factor of about 5 are possible with repetitive pulses of 1 nanosecond duration. Such repetitive pulsers are already commercially available. Therefore, power budget reductions by a factor of 1000 relative to the DC case at 10^{12} electrons/cm^3 can be readily obtained with a repetitively pulsed technique.

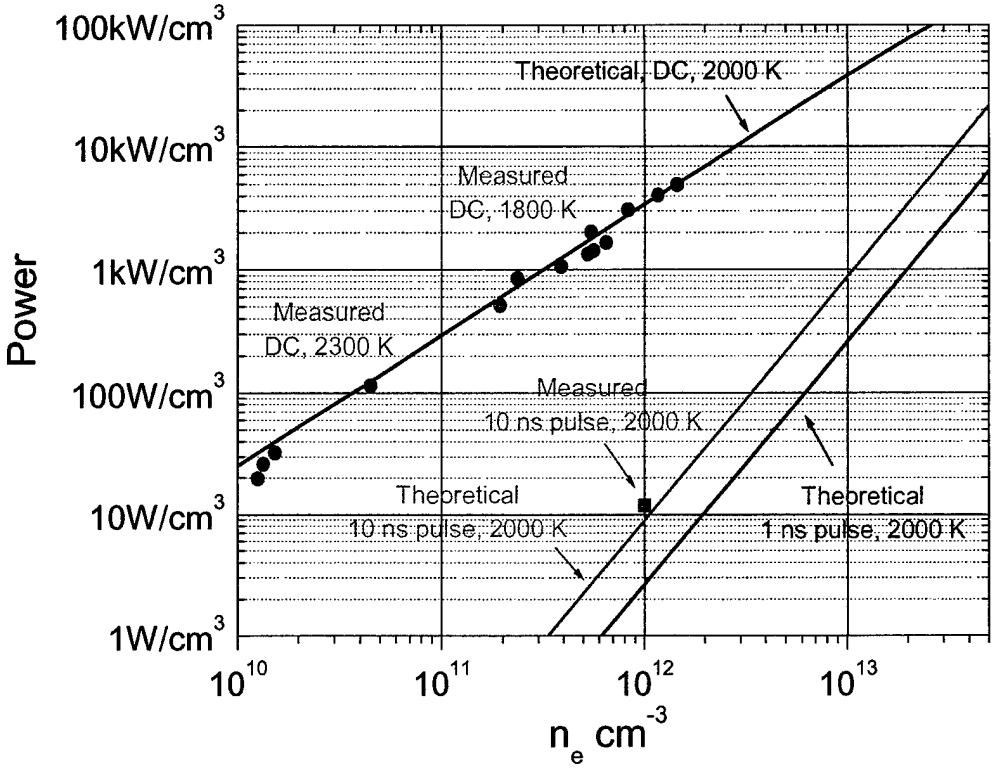

Figure 59. Power budget requirements vs. electron number density for DC and pulsed discharges in air at 1 atm, 2000 K.

6. Computational Analysis of Diffuse Discharges in Atmospheric Pressure Air

6.1. Introduction

In this part of the report, we use computational simulations to study the mechanisms that determine the size and stability of the DC discharges described in Section 4 of this report. The CFD models the gas flow coupled to the Joule heating of the electrons. A three-temperature model for the plasma energetics is used in conjunction a two-temperature chemical kinetics model for 11-species air. Finite-rate coupling between the energy modes and all of the relevant transport processes are included. We use this code to simulate the Stanford University DC and pulsed plasma torch experiments. We find that turbulent mixing in the torch jet appears to affect the discharge behavior, and a simplified flow model produces results consistent with those obtained in experiments.

6.2. Flow Field and Discharge Model

The flow within the plasma torch experiment test section is described by the Navier-Stokes equations that have been extended to include the effects of nonequilibrium thermochemistry and the applied electric field. Thus, we solve a separate mass conservation equation for each of the chemical species to allow the finite-rate formation and destruction of all relevant chemical species. In our simulations of the air plasmas, we use an 11-species model that accounts for all air species as well as their ions (N_2, O_2, NO, N, O, N_2^+, O_2^+, NO^+, N^+, O^+, e). The chemical kinetics of the multi-temperature plasma are described by the model developed at Stanford under the APRP. Additional details of the model are given in this report and in [65] and [13].

The velocity field is described by solving conservation equations for the radial, axial, and swirl direction momenta. Under typical torch operating conditions, about half of the test gas is injected into the torch with a component of velocity in the swirl direction, resulting in a medium to high degree of swirl at the entrance to the test-section. The swirl was thought to be instrumental for explaining the poor agreement of the previous simulations with experimental results as far as the radial profiles of individual variables are concerned. The effect of swirl is properly accounted for in the present simulations.

When an electric field is applied to the plasma, the rate of energy transfer between the different energy modes largely determines the steady-state electron concentration in the plasma. Thus, a complete model of the plasma energetics is required. We solve a total energy conservation equation, a separate mass-averaged vibration-electronic energy conservation equation, and an electron

translational energy equation. The vibration-electronic energy of a given species is defined to be the difference between that species' internal energy computed from the Gordon and McBride data [67] and the sum of its translational-rotational energy and heat of formation. This approach is taken by Gnoffo [68]. The rate of electrical energy input and the rate of energy transfer between the modes are modeled as detailed below.

In our model, the DC discharge adds energy to the plasma through the electrons via the Joule heating term. As a result, the electron temperature increases, causing electron-impact ionization and the further production of electrons, thus cooling the electron gas. At the same time, the electrons transfer their energy to the heavy particles through collisions and inelastic losses. We represent model these processes with the following energy conservation equations. In general, the change of energy = divergence of energy flow + energy source terms.

$$\frac{\partial E}{\partial t} = -\nabla \cdot \left((E + p)\vec{u} + \vec{q} + \vec{u} \cdot \tilde{\tau} \right) + \frac{j^2}{\sigma}$$

$$\frac{\partial E_v}{\partial t} = -\nabla \cdot \left(E_v \vec{u} + \vec{q}_v \right) + Q_{T-v} + Q_{v-e} + \sum_s w_s e_{vs}$$

$$\frac{\partial E_e}{\partial t} = -\nabla \cdot \left(E_e \vec{u} + \vec{q}_e \right) + \frac{j^2}{\sigma} - Q_{h-e} - Q_{v-e} + w_e e_e$$

Note that the total energy, E, has a source term due to the Joule heating, as well as the usual viscous transport and pressure-work terms. The vibrational energy, E_v, has the source terms representing energy transfer to vibration from the V-T relaxation and the electron-vibration energy transfer. In addition, the last term on the right-hand side represents the addition and loss of vibrational energy due to chemical reactions. The electron energy equation has the same form, but also includes the Joule heating term. The heat flow vectors $\vec{q}$, $\vec{q}_v$, and $\vec{q}_e$, contain heat conduction and heat carried by mass diffusion. The semi-empirical formula of Blottner *et al.* [69] and curve fits provided by Gupta *et al.* [70] are used to obtain the energy transport properties. Unfortunately, for flows with bulk phenomena such as turbulent mixing, a general multi-component approach for transport properties is not available. This limitation will be discussed later in the report.

The energy transfer terms $Q_{T\text{-}v}$, $Q_{h\text{-}e}$, and $Q_{v\text{-}e}$, the translation-vibration energy transfer rate, the heavy-particle-electron energy transfer rate, and the vibration-electron energy transfer rate, respectively, are taken from this report, as well as [13] and [71]. The diffusional mass fluxes carry energy and are calculated per species using the explicit expression derived by Ramshaw [72] in his self-consistent effective binary diffusion approximation. The driving forces in this formulation are

the species concentration gradients and the body forces acting on the charged species due to the ambipolar electric field. Ambipolar diffusion is included because concentration gradients of charged particles exist in regions of no current flow and their diffusion is curbed by the presence of neighboring charged particles. The first expansion of the binary diffusion coefficient, utilizing the weighted averages of the pair cross sections, is used.

The discharge is assumed to be axisymmetric, with no Lorentz force and a coincident axial electric current. As shown in the energy conservation equations, the electric field influences the total energy and the electron energy through the Joule heating source term. The current carried by the plasma is controlled experimentally, and is thus a prescribed parameter. Therefore, the current must be conserved at each axial location between the electrodes. A flux of electrons is introduced at the cathode location. It is calculated from the total current in the discharge and the effective area of the cathode. Sheath details are not resolved, and the current is considered to be entirely carried by the electrons. Between the electrodes the charged particles are acted upon by the electric field. The flux of electrons passing through a unit area per unit time is

$$\Gamma_e = \rho_e \vec{\bar{u}}_e$$

where $\vec{\bar{u}}_e$ is the mean drift velocity and is related to the kinetic energy acquired by the electrons under the influence of the electric field. The mean drift velocity of the electrons depends on the electric field and the electron mobility, μ_e

$$\vec{\bar{u}}_e = \mu_e \vec{E}$$

The electron mobility is related to the collision frequency, ν_e, between electrons and heavy particles.

$$\mu_e = \frac{e}{m_e \nu_e}$$

For the experimental conditions, the ions have negligible concentrations and the collision frequency is approximated by

$$\nu_e = n \nu_{the} Q_{en}$$

where n is the number density and ν_{the} is the thermal velocity of the electrons,

$$\nu_{the} = \sqrt{\frac{8kT_e}{\pi m_e}}$$

and the average cross-section Q_{en} is the average momentum transfer cross section taken to be 10^{-15} cm^{-3}.

The most critical issue of the discharge modeling is how to enforce current conservation between the electrodes. It is possible to solve some form of a Poisson equation for the electrical potential as a function of the local plasma properties. However, this approach has a number of draw-

backs, including many numerical difficulties, expense of solving the Poisson equation, and difficulty with enforcing total current conservation at each axial location between the electrodes. Also, because the region of the discharge is well defined, a simpler more direct approach may be used. The basic concept is to directly enforce total current conservation at each axial location between the electrodes.

To formulate the discharge model, we start with the current density, j, from

$$j \approx j_e = -en_e\bar{\bar{u}}_e$$

where again $\bar{\bar{u}}_e$ is the mean drift velocity. If we assume that there is no variation in the drift velocity in the radial direction, we can then write the total current, I, as

$$I = \int_A jdA \cong -e\bar{\bar{u}}_e(x)\int_A n_e dA$$

where the integral is taken in the radial direction, and again we assume that the mean drift velocity is only a function of the axial distance, x. We can then compute $\bar{\bar{u}}_e(x)$ from the above equation. We then obtain the local value of j for use in the Joule heating source term, j^2/σ. The electrical conductivity is defined using the calculated particle mobility and electron number density

$$\sigma = \mu_e e n_e$$

This approach is essentially equivalent to the classical channel model discussed in Ref. [73]. The radial extent of the discharge is then determined by the local electron number density in relation to the total electron number density at each axial location. Thus, the rate of ionization, energy transfer between modes, and the rate of radial diffusion of the electrons reach a balance to define the extent of the elevated electron concentration region.

This discharge model will be accurate in regions where the equipotential lines are not curved, which is a good approximation for most of the discharge. However, near the cathode the discharge radius visually appears to expand rapidly, and the potential lines tend to wrap around the cathode. But this is a localized effect (confined to about a discharge diameter) and does not appear to have an important influence on the predicted discharge characteristics.

6.3. Numerical Method

The conservation equations discussed above and discussed in more detail in [65] and [74], may be written as

$$\frac{\partial U}{\partial t} + \frac{\partial F}{\partial x} + \frac{1}{r}\frac{\partial rG}{\partial r} = W$$

where U is the vector of conserved variables, F and G are the flux vectors, and W is the source vector. The equations may be solved using many different computational fluid dynamics methods. We

choose to use a finite-volume formulation and evaluate the fluxes with an upwind modified Stegger-Warming flux vector splitting approach [75].

Under the conditions of the DC discharge experiments, the energy relaxation processes are very fast relative to the fluid motion time scales and the chemical kinetic processes. To handle this large disparity in characteristic time scales, we would usually use an implicit time integration method [75]. However, for this problem a complete linearization of the problem is itself very expensive. We solve 17 conservation equations, and the cost of evaluating the Jacobians and inverting the system scales with the square of the number of equations. Therefore, we linearize only those terms that are relatively fast, which results in a simple and inexpensive semi-implicit method that very substantially reduces the cost of the calculations.

The relatively fast terms are the internal energy relaxation and the Joule heating terms in the source terms for the three energy equations. Therefore, we split the source vector, W, into those "fast" terms, W_{fast}, and all of the other terms, W_{slow}. The conservation equations are then written as

$$\frac{\partial U}{\partial t}+\frac{\partial F}{\partial x}+\frac{1}{r}\frac{\partial rG}{\partial r}=W_{fast}+W_{slow}$$

We then linearize W_{fast} in time

$$W_{fast}^{n+1}=W_{fast}^{n}+C_{fast}^{n}\delta U^{n}+O(\Delta t^{2})$$

where C_{fast} is the Jacobian of W_{fast} with respect to U and $\delta U^{n}=U^{n+1}-U^{n}$. Because of the form of W_{fast}, C_{fast} is a simple matrix that can be inverted analytically. Then the solution is integrated in time using

$$U^{n+1}=\left(I-\Delta tC_{fast}^{n}\right)^{-1}\left(\Delta t(W_{fast}^{n}+W_{slow}^{n})-\Delta t\left(\frac{\partial F^{n}}{\partial x}+\frac{1}{r}\frac{\partial rG^{n}}{\partial r}\right)\right)$$

This approach increases the stable time step by a factor of at least 50 compared to an explicit Euler method at essentially no additional computational time per time step. This results in a very large reduction in the computer time required to obtain a steady-state solution and enables the simulation of the Stanford plasma experiments. This numerical method has also been used to simulate the pulsed discharge experiments performed at Stanford University [65]. We find that the time step must be reduced during the duration of the pulse, but then the time step may be increased significantly as the plasma cools between pulses.

A two-block grid is used to facilitate the implementation of the boundary conditions. The first grid block represents a portion of the plasma torch, the nozzle and the test section, and the second grid block acts as a large constant-pressure exhaust reservoir at one atmosphere. A schematic

of the computational grid is shown in Figure 60. Grid block 1 has 35 points in the axial direction and 35 points in the radial direction, with exponential clustering near the test section surface. The second block is 110×75, with an exact matching of the radial spacing at the block interface.

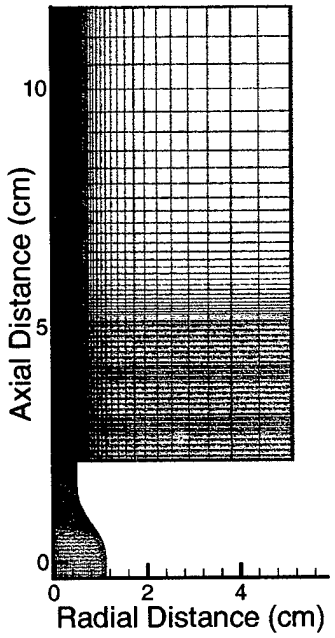

Figure 60. Schematic of two-block grid used to model the Stanford discharge experiments.

The inflow boundary conditions are set by varying the assumed inflow static pressure until we obtain the experimental gas mass flow rate of 4.9 g/s. The inflow is assumed to be in LTE at the measured temperature profile. This results in a consistent representation of the inflow conditions. The boundary conditions along the test-section surface are straight-forward. The velocity is zero at the surface, the temperature is specified, and the normal-direction pressure gradient is zero. We assume that the metallic surface is highly catalytic to ion recombination. Otherwise, the surface is assumed to be non-catalytic to recombination for neutrals.

The computation is initialized as follows: first, the inflow conditions are specified as above. Then the test-section and reservoir are all initialized at atmospheric pressure, and at each axial location the temperature profiles and chemical concentration profiles are set identical to the inflow boundary profiles. Once a converged solution is obtained for the flow in LTE, the discharge is ignited by injecting a flux of electrons at the cathode and applying the Joule heating source term to the energy equations. Then a steady-state solution for the DC discharge is obtained.

6.4. Results

Let us first consider the flow of the torch jet into the atmosphere without electrical energy addition. Figure 61 plots contours of velocity magnitude and density, overlaid with instantaneous streamlines. Clearly the jet is unstable, with the shear layer rolling up into vortices. This results in an unsteady flow field, with the vortical structures propagating downstream at approximately the shear layer mean convective speed. Simulations have been carried out to many characteristic times, and these structures persist in the calculations.

Previous results [65, 74, 76] did not demonstrate this unsteadiness, but those calculations used an artificially high reservoir temperature of 800 K, rather than the 300 K used here. Thus, the present results have a reservoir density that is nearly three times larger and a significantly lower viscosity in the shear layer. These differences greatly enhance the jet instability. Additionally, the roll-up of vortical structures in a shear layer is greatly affected by the dissipation of the numerical method. In our results, we have taken care to reduce the numerical error by using a second-order accurate with low dissipation and by clustering the grid at the jet interface. These high-quality numerics increases the propensity of the jet to form vortical structures.

The flow field described by the Navier-Stokes equations assumes that the flow from the nozzle to the open atmosphere is laminar. The flow at the end of the nozzle section has a Reynolds number of about 10^4, suggesting that the flow in the nozzle is likely transitional or turbulent. The cold gas mixing upstream of the nozzle also enhances the turbulent motion in the nozzle. Thus it is highly likely that the jet flow is transitional or turbulent. The effect of turbulence is to increase the mixing across the jet shear layer, which tends to enhance its stability and reduce the formation of the organized vortical structures seen in Figure 61.

With the background flow described above, we now include electrical energy addition. For computational reasons, we establish the discharge by propagating the electron flux from the cathode downstream to the anode before "igniting" the discharge. This provides an initial channel of electrons to carry the current. These electrons absorb the electrical energy, are boosted to high temperature, and rapidly produce more electrons until a balance between the energy addition and losses is established.

Once the discharge is ignited, it is impossible to obtain a steady-state solution for the discharge. Figure 62 plots contours of vibrational temperature and electron number density 6.4 μsec after the energy addition is started. Note the non-uniformity in the discharge, with substantial

tions in n_e along the axis. In particular, the elevated region of n_e corresponds to the narrowing of the jet by the vortical structures. The discharge is not robust, and as the cycle of vortical motion occurs in the shear layer, the discharge is pinched and transforms into an arc.

It should be noted that the time scale of the vortical motion is *much* larger than that of the discharge formation. The vortices are convected downstream at the mean convective speed, which for this case is about 200 m/s. Thus, the time required for a vortex to propagate between the electrodes is about 200 μs. This is obviously much larger than the time required for the discharge to collapse into an arc. Therefore, it is highly unlikely that the modifications to the flow field by the electrical energy addition would prevent arc formation.

In spite of these numerical results, the experimentally observed discharge is stable, and the obvious question is: Why does arcing happen in the computations, but not in the experiments?

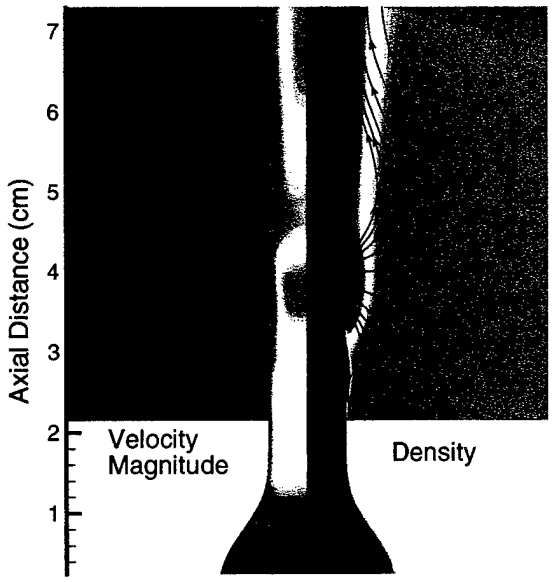

Figure 61. Contours of velocity magnitude and density at the experimental conditions without the discharge.

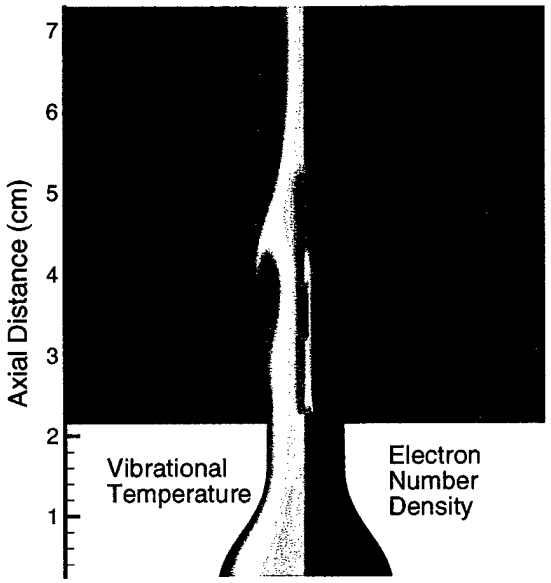

Figure 62. Contours of vibrational temperature and electron number density, 6.4 μsec after discharge initiation.

One important mechanism to stabilize the discharge is radial heat conduction. If the flow is transitional or turbulent, the heat flux must have a component due to turbulent motion. There is no adequate model for predicting turbulence in gas discharges or plasmas. Huang [77] introduced a two-fluid turbulence model for thermal plasma sprays that qualitatively reproduces the large-scale transport. He showed that pockets of heated gas move away from the shear layer, convectively transporting large amounts of heat. This mechanism would also inhibit the formation of large-scale vortical structures.

Unfortunately, without additional information about the properties of the experimental jet, it is very difficult to make *predictive* simulations for turbulent flows. We could include a turbulence model, but this would involve a tedious and unrewarding game of parameter adjustment (tuning) to get reasonable results. We have therefore resorted to an approximate approach to better understand the role of mixing in the discharge stability.

6.5 Approximate Discharge Model

The jet shown in Figure 61 and Figure 62 grows primarily by mixing across the shear layer. This mixing is slow, with the jet size remaining (at least visually) constant for the 3.5 cm length of

the discharge. We can exploit this slow growth rate of the jet, and develop a simple and cost-effective jet/discharge model.

If we assume that the growth of the jet is simply due to diffusive processes (viscous dissipation, thermal conduction, and mass diffusion), then the flow gradients that drive these processes are negligible in the axial, x, direction. Then the above conservation equation becomes

$$\frac{\partial U}{\partial t} = W - \frac{1}{r}\frac{\partial rG}{\partial r}$$

and the two-dimensional steady-state equation is converted to a one-dimensional time-dependent problem that is *much* easier to solve. Within the limitations of our assumptions, this approach is useful to study the discharge growth mechanisms.

To implement this model, we start at the cathode plane where a known flux of electrons is imposed on the inflow velocity and temperature profile. We then integrate the above equation in time. Since the axial velocity, u, varies only with r, we can construct the entire flow field by simply using $x=ut$.

Figure 63 plots contours of temperature and electron number density in the flow field computed with the approximate method at the experimental conditions. Note that because we have neglected the streamwise gradients, there is no mechanism to promote instability of the jet. Interestingly, if the calculation is run without the diffusive transport terms included, the discharge immediately collapses to an arc. The jet grows very slowly because the thermal diffusivity is extremely low in the cold quiescent gas.

Figure 64 and Figure 65 plot the discharge properties along the centerline and at one axial location. A close examination of the plot shows that the electron temperature increases to very high values near the cathode (at $x=0$) where the electrical energy is added to a small number of electrons. The high T_e causes the rapid production of electrons, which then lowers the electron temperature, and a balance between the electron density and temperature is reached. This figure shows that the heavy particle and vibrational temperatures do not increase significantly, but the coupling between these modes and the electrons is responsible for limiting the electron temperature. The electron temperature is approximately 10,000 K, which is somewhat lower than the 12,000 K inferred from the experiments. The vibrational and translational temperatures closely match the measured values. The predicted electron number density for most of the discharge is about 4×10^{11} cm^{-3}, which is considerably below the value of 2×10^{12} cm^{-3} measured in the experiments. The lower value of n_e is consistent with the lower value of T_e predicted by the simulations because the electron concentra-

is very sensitive to the electron temperature. The reason for this difference is unknown at the present time, though the electron number density depends on the details of the ionization and energy transfer rates. In addition, the turbulent spreading of the jet would likely affect the discharge properties by cooling the edges of the jet more efficiently, resulting in more of the current being carried near the jet centerline. This would result in an increased centerline electron temperature and concentration.

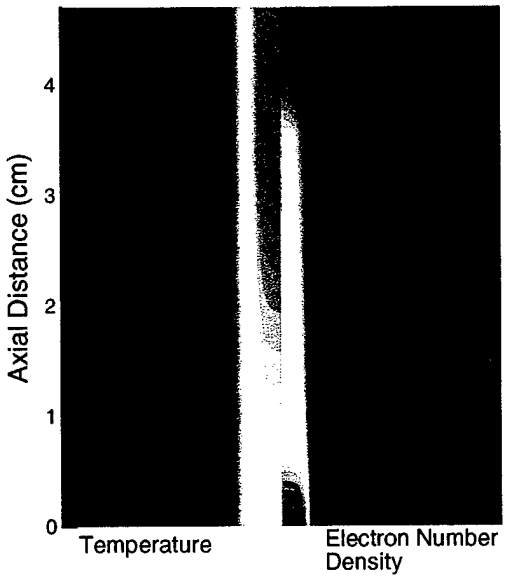

Figure 63. Contours of temperature and electron number density computed using the approximate method at experimental conditions.

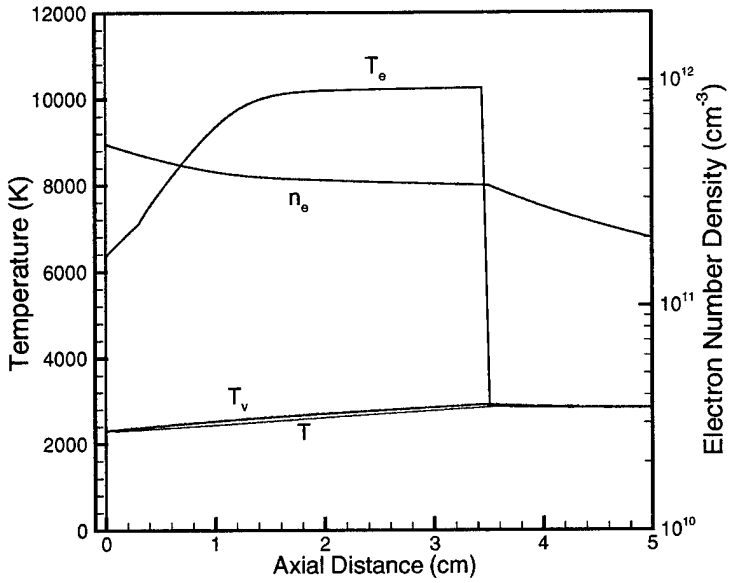

Figure 64. Centerline temperatures and electron number density computed using the approximate method at experimental conditions.

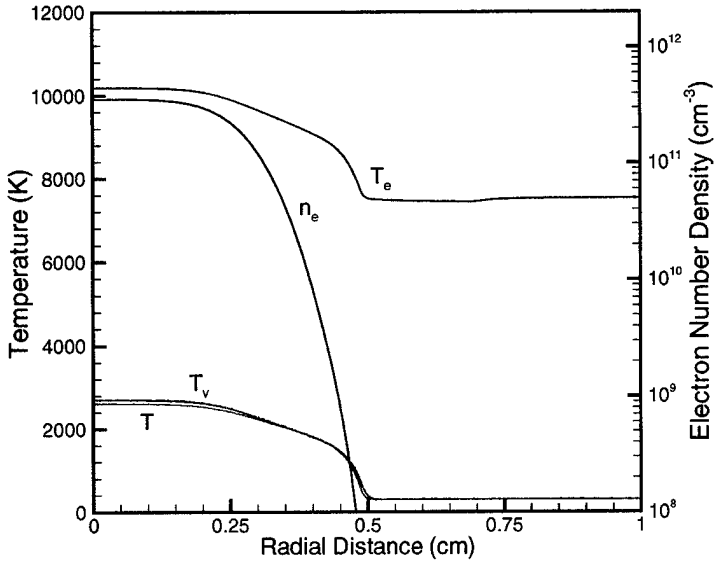

Figure 65. Cross-section of the computed discharge 2 cm from the cathode at experimental conditions.

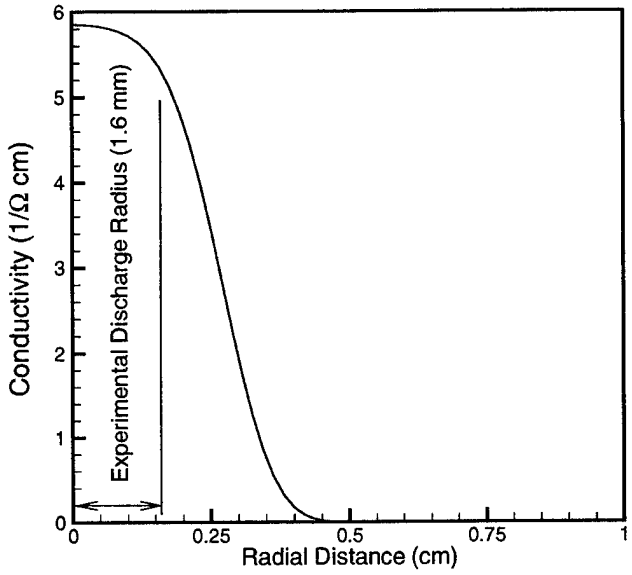

Figure 66. Electrical conductivity 2 cm from the cathode at experimental conditions.

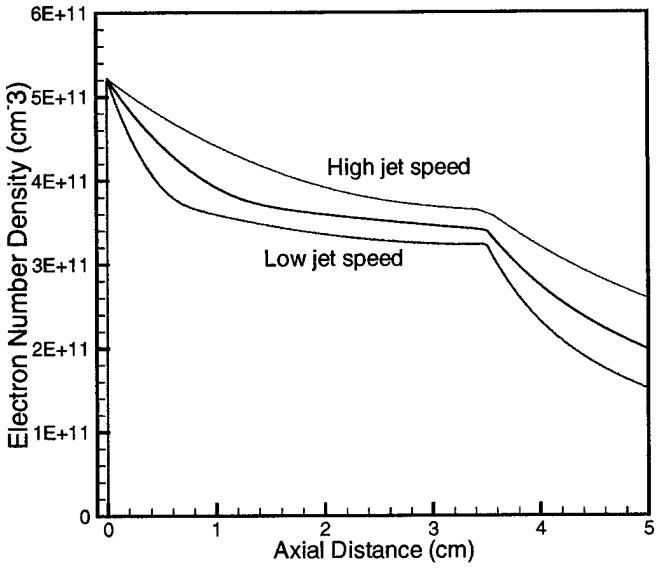

Figure 67. Variation of centerline electron number density with jet speed.

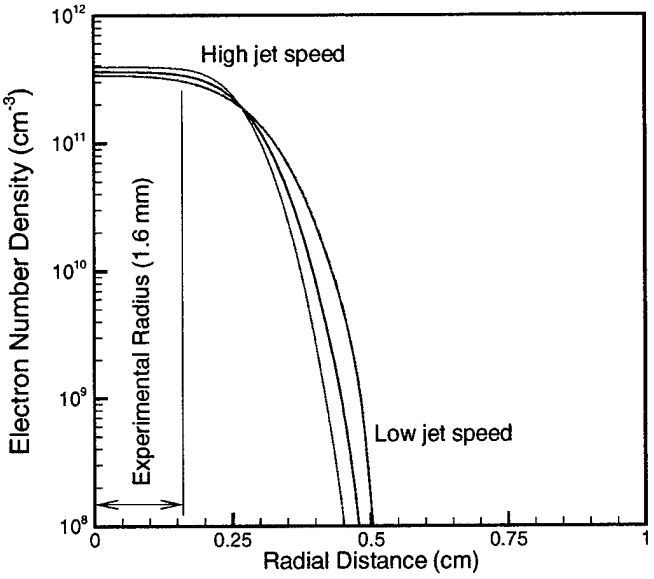

Figure 68. Radial variation of electron number density with jet speed 2 cm from the cathode.

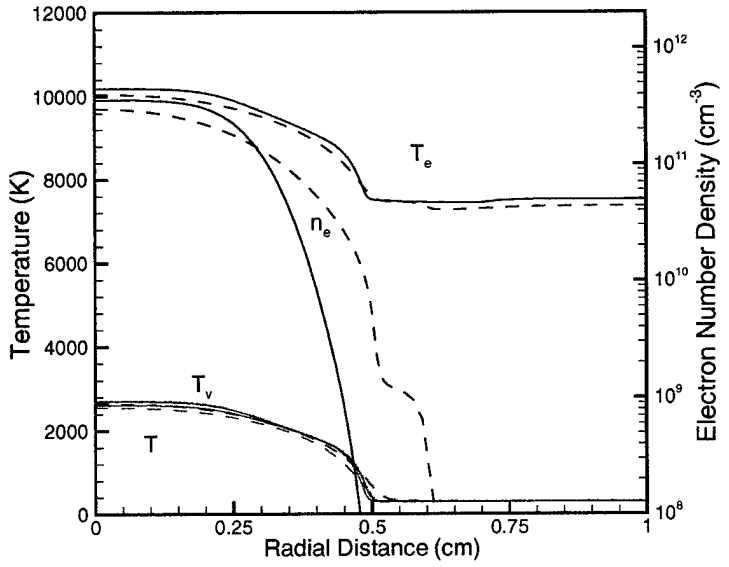

Figure 69. Radial variation of discharge properties. Solid lines: nominal transport properties; dashed lines: transport properties increased by a factor of 10.

The discharge diameter was measured to be approximately 3.2 mm. Figure 66 plots the electrical conductivity at a location 2 cm from the cathode. Although the edge of the discharge is not precisely defined, this plot shows that the computations produce a conducting channel of approximately the same dimension.

Figure 67 and Figure 68 summarize how the centerline and radial electron number density depend on the jet speed. Here, we have increased and decreased the jet speed by a factor of two from the measured 440 m/s. The higher jet speed reduces the rate of spreading of the jet, and therefore increases the centerline electron number density. However, this increase is minimal and is a result of the very slow mixing at the jet edge. The radial plot is consistent with the centerline results, showing an increased spreading at low jet speed. Again, the effect is small.

Based on the preceding arguments, we expect turbulent mixing to increase the spreading rate of the jet. We therefore performed additional simulations with the transport properties increased by a factor of 10 to mimic increased mixing. Figure 69 compares the radial variation of the temperatures and electron number density. The jet radius increases only minimally. Clearly, this simple approach of increasing the molecular transport properties does not produce substantial increased jet spreading. This is because turbulent mixing is a large-scale convective phenomenon. A more complete characterization of the jet is required to incorporate turbulent mixing into the model.

6.6. Conclusions

We have developed a computational methodology to analyze Stanford University DC and pulsed discharge experiments. A complete axisymmetric simulation including an 11-species finite-rate air kinetics model and a three-temperature energy formulation was used. A three-temperature model is used to allow separate heavy-particle, vibrational and electron translation temperatures of the plasma. The self-consistent effective binary diffusion model is used for the molecular transport properties. The discharge is modeled as a conducting channel, allowing a direct enforcement of total current conservation.

The governing equations are solved with a semi-implicit finite-volume method. The "fast" source terms are linearized in the time integration, resulting in a method that at least 50 times faster than an explicit method. A fully implicit method is about 100 times more expensive per time step, and does not significantly increase the stable time step size. Thus, for this problem that is dominated by very fast (order of nanosecond) time-scales, our semi-implicit approach is optimal and enables simulations of this type. The convective fluxes are represented by standard second-order accurate upwind fluxes, and the viscous fluxes use a central difference formulation.

The plasma torch simulations using this CFD model produced an unstable jet with large-scale vortical structures. Contrary to the experiments, the non-uniformities pinch the discharge and

transition to an arc occurs. We postulate that turbulent mixing in the experiments stabilizes the jet and prevents arcing.

To study the discharge spreading, we reformulated the model, freezing the gradients in the axial direction. This prevents formation of large vortical structures, and we obtain a stable diffuse discharge. The size of the computed electrically conducting channel matches the experiments, and the electron number densities are fairly well predicted considering that they are highly sensitive to the electric field or equivalently to the electron temperature. The vibrational and translational temperatures also agree well.

Using the approximate formulation, we varied the jet speed and transport properties to study how the jet spreads. We find that the very low thermal diffusivity in the cold external gas makes the jet spreading essentially insensitive to these changes. The lack of turbulent mixing in our model is a major limitation and future work should address this issue.

The effect of turbulent mixing appears to be to stabilize the jet under the high flow rate cases simulated. However, we expect that at lower flow rates where the jet does not roll up into vortical structures, the discharge will be stable. Under these conditions, the flow is very closely represented by the approximate discharge model, which produces a stable diffuse discharge. Thus although our simulations result in arc formation at the experimental conditions, this does not imply that our full axisymmetric simulations are unstable at all flow conditions.

The modeling of turbulent mixing in these flows is very challenging. We are investigating the approach of Huang as one means of increasing the heat transfer across the jet interface. However, this approach is largely empirical and will not result in a truly predictive capability to simulate this type of flow. Other turbulence modeling approaches for free jets can be used that may result in a more accurate and general model. This should be supported by a systematic study of varying the torch flow properties in experiments to better characterize the role of turbulence in these flows.

7. Measurements of Ion Concentration by Cavity Ring-Down Spectroscopy

7.1. Introduction

Measurements of ion and/or electron number density are needed to characterize experiments and validate models for the atmospheric pressure air and nitrogen plasmas presented in this report. The ionization fraction in these atmospheric pressure plasmas is of the order of 10^{-5}, so that sensitive measurement techniques are required. Physical probes tend to disturb the system, and techniques such as Thomson scattering and interferometry do not readily provide results with high spatial resolution. Optical techniques that measure ion concentrations are widely used. Of these, emission provides information only on excited species, fluorescence suffers from quenching effects and optical interference that complicate interpretation, and absorption often lacks sensitivity. Cavity ring-down spectroscopy (CRDS), on the other hand, is a sensitive line-of-sight laser absorption technique that has been used to measure species concentrations in low-pressure plasmas [78-82]. In particular, the N_2^+ ion has been studied in low-pressure hollow cathode sources [83, 84]. We have selected CRDS as our primary diagnostic tool to characterize ion concentrations. In this section, we describe the use of CRDS to measure ion concentrations in atmospheric pressure discharges. By implementing CRDS in its "standard" form, we perform spatially resolved ion concentration measurements. We also develop a temporally resolved variant of CRDS, which we used to study ion recombination in pulsed plasmas. Measurements have been performed in both air and nitrogen plasmas. In nitrogen plasmas, CRDS measurements of the dominant N_2^+ ion enable characterization of plasma ionization. In the air plasmas, CRDS measurements of the NO^+ ion were performed.

An overview of the CRDS technique is provided in Section 7.2, including a discussion of temporally resolved CRDS. Section 7.3 presents the experimental schemes used for spatially resolved ion concentration measurements of the N_2^+ ion in DC discharges, as well as temporally resolved N_2^+ ion concentration measurements in pulsed discharges. Measurement results, and discussion, are provided. To aid in interpreting results, a collisional radiative (CR) model is used to compute population fractions and to relate the measured ion concentrations to electron number densities. The inferred electron number density profiles are compared with electrical measurements, and the nonequilibrium nature of the plasma is discussed. Section 7.4 discusses CRDS measurements of the NO^+ ion in air plasmas. The experimental scheme and a discussion of results are presented. Conclusions are provided in Section 7.5.

7.2. Cavity ring-down spectroscopy

Cavity ring-down spectroscopy has become a widely used method in absorption spectroscopy owing primarily to its high sensitivity. Detailed reviews of the technique may be found in References [85, 86]. Essentially, a laser beam is coupled into a high-finesse optical cavity containing a sample, where it passes many times between the mirrors. As the light bounces back and forth inside the cavity, its intensity decays (rings down) owing to sample absorption, particle scattering loss (generally negligible), and mirror transmission loss. A photodetector is used to measure the ring-down signal, which is fitted to yield the sample loss. The technique affords high sensitivity owing to a combination of long effective path length and insensitivity to laser energy fluctuations, and therefore is well suited to the detection of trace species in plasmas. Under appropriate conditions, the laser lineshape may be neglected, and the ring-down signal $S(t)$ decays exponentially [87, 88] as:

$$\begin{aligned} S(t) &= S_0 \exp\left[-t/\tau\right] \\ 1/\tau &= \frac{c}{l}\left[l_{abs}k(\nu_L)+(1-R)\right] \end{aligned} \tag{33}$$

where τ is the 1/e time of the decay (termed the ring-down time), c is the speed of light, l is the cavity length, l_{abs} is the absorber column length, $k(\nu)$ is the absorption coefficient, ν_L is the laser frequency, and 1-R is the effective mirror loss (including scattering and all cavity losses). Generally, the measured ring-down signal is fit with an exponential, and the ring-down time τ is extracted. Combining τ with the ring-down time τ_0 measured with the laser detuned from the absorption feature allows a determination of the sample absorbance, and hence absorption coefficient:

$$Abs \equiv l_{abs}k(\nu_L) = \frac{l}{c}\left[\frac{1}{\tau} - \frac{1}{\tau_0}\right] \tag{34}$$

We minimize any potential laser lineshape dependence by tuning the laser frequency across an absorption line, and measuring the frequency-integrated absorption coefficient [88].

The prior discussion of CRDS has implicitly assumed that the sample concentration (and associated absorption loss) is independent of time, as would be the case in the DC discharge. However, a more complex approach is required to measure time dependent concentrations in pulsed discharges, since the ion concentration varies over the duration of the optical ring-down (decay of light in the cavity). It might be tempting to consider using lower reflectivity mirrors with shorter ring-down times so that the losses may be treated as constant over the ring-down, but the sensitivity of such an approach is inferior [87]. Although a number of kinetics studies have been performed with CRDS, nearly all of these experiments study processes that are slow compared to experimental

ring-down times. An exception is the work of Brown et al. [89], who perform gas-phase measurements in cases where the populations do change over the duration of the ring-down. We follow a related approach to measure ion recombination in a plasma over time-scales comparable to the ring-down time (microseconds). For the case of a time-dependent absorption, the ring-down signal S(t) may be written as [89]:

$$S(t) = S_0 \exp\left[-\frac{c}{l}\left[\int_0^t k(\nu,t)\,l_{abs}\,dt + (1-R)t\right]\right] \tag{35}$$

where the absorption coefficient now has a time dependence. Rearranging equation (35) leads to an expression for the absorbance as a function of time:

$$\begin{aligned} Abs(t) &\equiv k(\nu,t)\,l_{abs} \\ &= -\frac{l}{c}\frac{d}{dt}\left[ln\left(\frac{S(t)}{S_0}\right)\right] - (1-R) \end{aligned} \tag{36}$$

The derivative (local slope) of the logarithm of the ring-down signal is proportional to the loss (sample plus empty cavity) at that time. To directly obtain time-dependent concentrations, Brown et al. analyzed their data with this method. We choose to follow an alternative approach in which the ring-down signal is divided into a series of time-windows, each of which is fit to an exponential decay (ring-down time). We believe that this approach is less noisy because it avoids differentiation.

7.3. N_2^+ Measurements

7.3.1. Experimental Setup

7.3.1.a. Atmospheric Pressure Discharge

We have developed a compact atmospheric pressure plasma source for diagnostic development. The discharge may be operated with both nitrogen and air. A photograph of the nitrogen discharge with a schematic representation of the ring-down cavity is shown in Figure 70. Nitrogen is injected through a flow straightener and passes through the discharge region with a velocity of about 20 cm/s. The discharge is formed between a pair of platinum pins (separation 0.85 cm) that are vertically mounted on water-cooled stainless-steel tubes. The discharge is maintained by a DC current supply (i_{max}=250 mA) in a ballasted circuit (R_b=9.35 kΩ). The pins are brought together to ignite the discharge, and are then separated using a translation stage. The position of the discharge is observed to be stable and reproducible. The discharge is contained within a Plexiglas cylinder

through the top to avoid accumulation of undesirable by-products of the discharge (such as ozone or oxides of nitrogen), and enable passage of the laser beam through the discharge. A second translation stage is used to displace the entire discharge cylinder relative to the optical axis in order to obtain spatial profiles.

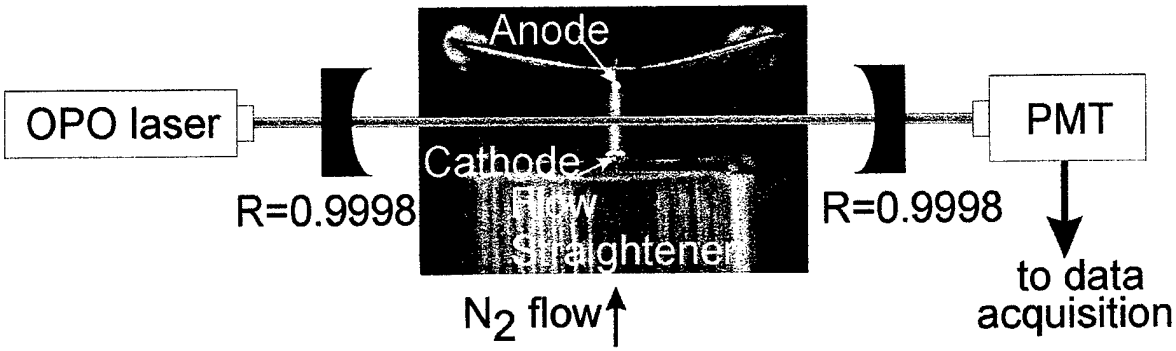

Figure 70 Photograph of the atmospheric pressure nitrogen discharge and schematic diagram of the ring-down cavity. Electrode separation: 0.85 cm. Discharge current: 187 mA.

To explore the repetitively pulsed approaches, we connect a high-voltage pulser in parallel to the DC discharge circuit. The pulser is capacitively coupled to the discharge so that it is isolated from the DC supply. The DC field serves to give a baseline of ionization, and to heat the gas. We operate the high-voltage pulser (pulse width~10ns, pulse voltage~8 kV) at 10 Hz so that it may be synchronized relative to the laser. At this repetition rate the plasma equilibrates between high-voltage pulses so that the behavior during and following each pulse is not affected by the presence of other pulses.

7.3.1.b. CRDS Measurements.

We study the N_2^+ ion by probing the (0,0) band of its first negative system ($B\ ^2\Sigma_u^+ - X\ ^2\Sigma_g^+$) in the vicinity of 391 nm. We select this spectral feature because it is comparatively strong and optically accessible. The optical layout is shown in Figure 71. An OPO system (doubled idler) is used as the light source (repetition rate = 10 Hz, pulse width ~ 7 ns, pulse energy ~ 3 mJ, linewidth ~ 0.14 cm^{-1}). The output from the OPO passes through a Glan-Taylor polarizer to attenuate the energy, and several beam shaping optics to approximately mode-match the beam into the cavity. We use a linear cavity of 75-cm length with 50-cm radius-of-curvature (ROC) mirrors. The selection of cavity geometry is discussed below. Typically, about 100 μJ per pulse is incident on the back face of the entrance ring-down mirror. The ring-down signal is collected behind the output mirror with a fast photomultiplier tube (Hammamatsu-R1104), which we filter against the pump

mirror with a fast photomultiplier tube (Hammamatsu-R1104), which we filter against the pump laser and other luminosity with two narrow-band interference filters (CVI-F10-390-4-1). The PMT signals are passed to a digitizing oscilloscope (HP 54510A, 250 MHz analog bandwidth, 8-bit vertical resolution) and are read to computer with custom data acquisition software. In a typical ring-down spectrum, 16 or 32 decay curves are averaged at each wavelength, and the resulting waveform is fitted with an exponential to yield the ring-down time τ. For the DC measurements, the portion of the ring-down signal used in the fit is that in between 90% and 10% of the peak (initial) signal amplitude. The detuned ring-down time τ_0 is determined with the laser tuned off the absorption features. Spectral scans use a step-size of 0.001 nm. When performing spatial scans, we use step-sizes of 0.2 mm.

The CRDS set-up used for the pulsed measurements differs only in terms of data fitting and timing. Because sample absorption loss is no longer constant during the measurement, the time dependent equation (36) is used to fit the data. Rather than computing derivatives we fit a series of line segments to the logarithm of the ring-down signal. The fitting windows are 1-μs in length. This time interval represents a good compromise in making the window short compared to the timescale of the process studied yet affording an acceptable signal-to-noise level. Because our time windows are long compared to the pulse length (~ 10 ns), we do not resolve the build-up of ionization that occurs during the time the pulse is on; yet we are able to resolve the subsequent recombination. We synchronize the laser relative to the firing of the discharge with an external timing circuit. In order to obtain concentration information at different times relative to the firing of the high voltage pulse, we vary the delay time between the firing of the laser and the firing of the high voltage pulser. Delay times (T_{Pulse}-T_{Laser}) of –10,-8,-6,-4,-2,-1,0,1,2 μs are used.

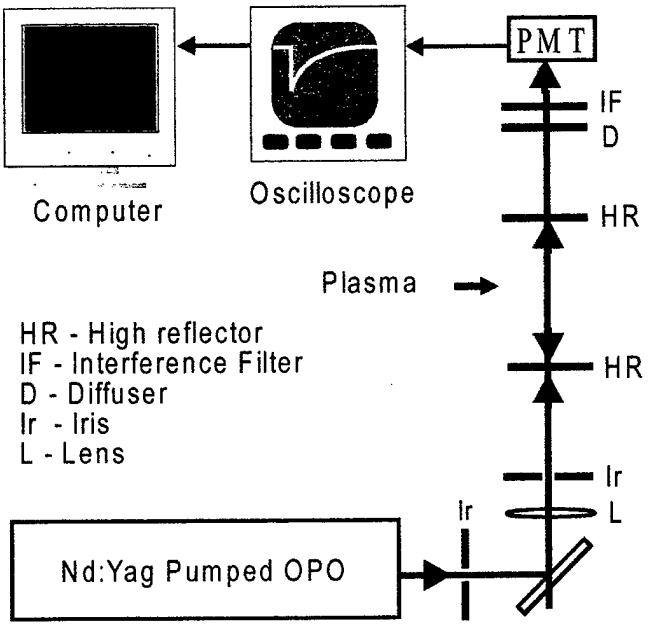

Figure 71 Schematic diagram of CRDS set-up. The ring-down cavity has a length of 0.75 m, and uses 0.5-m radius of curvature mirrors. An OPO is used as the light source, and a photomultiplier tube (PMT) detects the light exiting the cavity.

Implementing CRDS in the atmospheric plasma requires special care in the choice of cavity geometry. For a linear cavity formed with mirrors of equal radius-of-curvature, the cavity geometry is determined by the dimensionless g-parameter, defined as unity minus the cavity length divided by the mirror radius of curvature [90]. Initial attempts to form a ring-down cavity with g= 0.875 (length 75 cm, 6-m ROC mirrors), resulted in distorted and irreproducible profiles, owing to beam steering from index-of-refraction gradients (similar to a mirage). Recent work by Spuler et al. [91] simulates the effect of cavity geometry on beam propagation in CRDS experiments. Their results indicate that a g-parameter of about -0.5 represents a good compromise between beam waist and beam walk in environments where beam steering may be present. Accordingly, we form a cavity of length 75 cm, with 50-cm ROC mirrors (Research Electro Optics). No beam steering is detected with this geometry. Qualitatively, this geometry tends to recenter deviated beams, whereas the more planar geometry is not as effective.

7.3.1.c. Electrical Measurements.

We also determine the electron number density in the discharge by an electrical conductivity approach. For the DC discharge, we measure the time independent discharge current and electric field, and use Ohm's law to compute the product of the average electron number density and column area. The electric field is found as the slope of the discharge voltage versus electrode separation. We write Ohm's law as $j=i/area=(n_e e^2/m_e \Sigma \nu_{eh})E$ where ν_{eh} is the average collision frequency between electrons and heavy particles. Because of the low ionization fraction ($<\sim 10^{-5}$), ν_{eh} is domi-

dominated by collisions with neutrals, so we can write $\nu_{eh} \cong n_n g_e Q_{en}$, where $n_n = P/kT_g$ is the number density of neutrals, $g_e = (8kT_e/\pi m_e)^{0.5}$ is the thermal electron velocity, and Q_{en} is the average momentum transfer cross-section for electron-nitrogen collisions. We determine T_e by means of a collisional radiative model [5], with input parameters (vibronic ground state population and rotational temperature) obtained from the CRDS measurements. Q_{en} is determined as a function of T_e from tabulated values [15].

We follow an analogous approach to determine the time varying electron number density in the pulsed discharge. In this case we measure the time-dependent current and electric field, and use these to determine temporally resolved electron number densities.

7.3.2. N_2^+ Measurements - Results and Discussion

7.3.2.a. N_2^+ Ring-Down Spectra.

N_2^+ ring-down spectra are recorded as a function of discharge current and position. We discuss the spectra in terms of measurement accuracy and detection sensitivity.

Figure 72 shows measured and simulated absorption spectra in the vicinity of the (0,0) bandhead of the first negative system. Rotationally resolved lines from the P and R branches are visible. The lines are identified using tabulated line locations [92, 93], and are labeled with the angular momentum quantum number N" of the lower state. The displayed spectrum is recorded along the discharge centerline, at a current of 187 mA, and averages 16 shots at each wavelength. The experimental spectrum is plotted in terms of single-pass cavity loss and illustrates the high sensitivity attainable with the CRDS technique. The cavity loss is the sum of mirror reflective loss and sample absorptive loss. (The Rayleigh scattering losses are computed to be negligible.) Near the bandhead, the signal is ~ 280 ppm/pass, the baseline reflective loss is ~ 200 ppm/pass, and the baseline noise is ~ 5 ppm/pass, so that the signal-to-noise (S/N) ratio is ~ 56. The S/N ratio suggests an absorbance-per-pass sensitivity of about 1 ppm, which corresponds to a detection limit of about 7×10^{10} cm^{-3} for N_2^+ ions at our experimental conditions. The baseline reflective loss of ~ 200 ppm/pass corresponds to a mirror reflectivity of ~ 0.9998 which is in accord with the manufacturer's specifications.

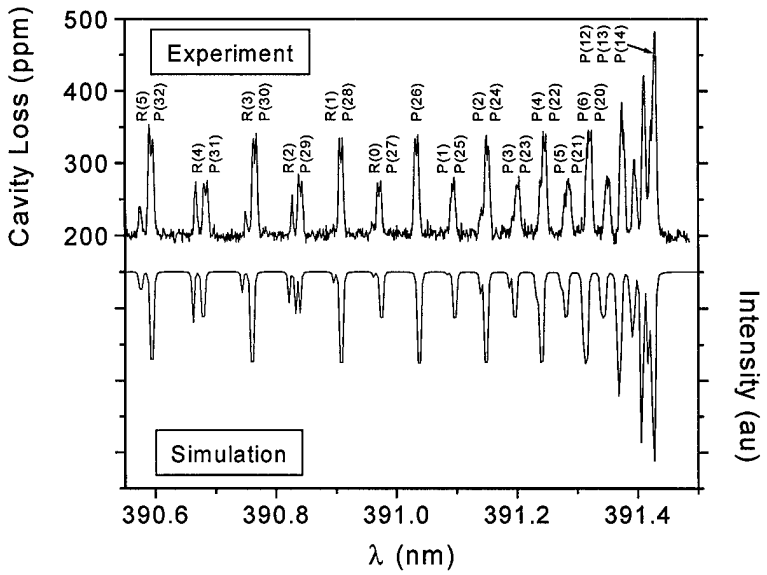

Figure 72 Measured and simulated N_2^+ absorption spectra near the (0,0) bandhead of the first negative system. Lines from the P and R branches are identified.

Figure 73 shows an expanded view of the P(28) and R(1) lines after baseline subtraction. Fitted Voigt peaks (constrained to have the same shape and width) are shown with solid lines, and their sum is shown with a dotted line. For the P(28) lines, the doublet structure due to the unpaired electron is apparent. The fit yields a doublet spacing of 0.005 nm, in good agreement with the literature [92, 93]. The R(1) lines are close to the detection limit and correspond to a N_2^+ X state population of about 10^{10} cm^{-3}. Their splitting is much less than the linewidths and is not resolved. The fitted FWHM of each peak is 0.0042 nm, or 7.9 GHz, which is consistent with an expected thermally broadened linewidth of ~ 7 GHz and a measured laser linewidth of ~ 4 GHz. Our calculations indicate that for these linewidths and absorption parameters, a measurement of the area of an absorbing feature will be negligibly affected by finite laser bandwidth [88]. Note that unlike in conventional absorption, such an assumption is not always correct in CRDS. The assumption was verified in the present work by fitting progressively earlier parts of the ring-down signal and confirming that the apparent absorbance remains constant.

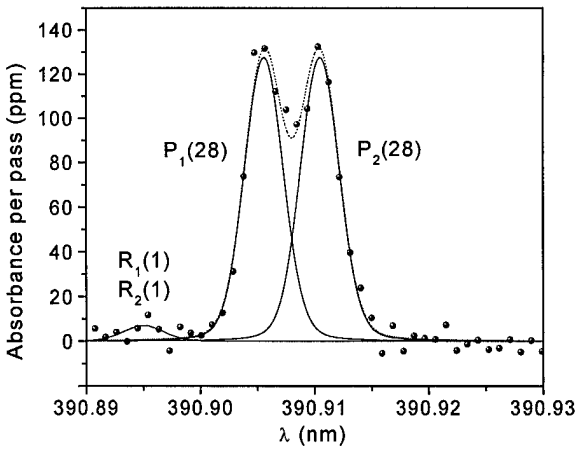

Figure 73 Expanded view of P(28), and R(1) lines from Fig. 3. Background absorption has been subtracted. Voigt peaks fitted to the doublet are shown with solid lines, while their sum is shown with a dotted line.

7.3.2.b. Spatial Profiles of Ion Concentration and Electron Number Density.

We obtain spatial profiles of the N_2^+ concentration by displacing the discharge perpendicularly to the optical axis. CRDS is a path-integrated technique and the discharge has axial symmetry. We verify the symmetry of the discharge by performing measurements with the plasma rotated by 90 degrees, and find that the cases have <2% deviation. We use an Abel inversion to recover the radial N_2^+ concentration profile. The concentration measurements are based on the (frequency integrated) area of the lines P(9)-P(17) in the (0,0) bandhead vicinity. We use tabulated line strengths from References [92, 93]. Figure 74 shows concentration profiles determined for different values of current (i=52, 97, 142, and 187mA). We find peak (centerline) N_2^+ concentrations of 7.8×10^{11}, 1.5×10^{12}, 2.4×10^{12}, and 3.6×10^{12} cm^{-3} for i=52, 97, 142, and 187 mA respectively. The shape of the concentration profile remains approximately uniform at the different conditions, though we observe that the radial half-maximum values increase slightly with current. We find radial half-maximums of 0.80, 0.82, 0.93, and 1.05 mm for i=52, 97, 142, and 187 mA respectively.

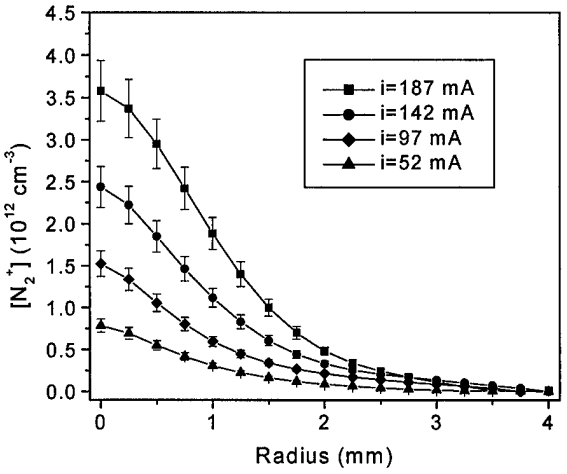

Figure 74 Radial concentration profiles of N_2^+ measured by CRDS in an atmospheric pressure glow discharge. Experimental data points are joined with line segments for visual clarity.

The error bars on N_2^+ concentration represent one standard deviation (1σ). They primarily arise from the uncertainties in relating the measured population of several rotational levels in the ground vibronic state, to the overall population of N_2^+. Because the discharge is out of equilibrium, this relationship depends on the how the rotational, vibrational, and electronic energy levels are populated. The rotational levels are equilibrated at the gas temperature owing to fast collisional relaxation. The rotational temperatures used in the analysis are obtained from Boltzmann plots, and are T_r=3100, 3600, 4150, and 4700 K for currents of i=52, 97, 142, and 187 mA respectively. The vibrational and electronic energy levels are out of equilibrium, and a collisional-radiative (C-R) model [5] is used to determine the fraction of the population in the ground vibronic state, and predicts 0.37±0.02, 0.35±0.02, 0.33±0.02, and 0.31±0.02 for i=52, 97, 142, and 187 mA respectively. Combining the rotational temperature uncertainties with those from the C-R model and those from the Abel inversion (~4%), results in an overall experimental uncertainty in concentration of ~10%.

The spatial resolution of our measurements is determined by the spatial step-size (0.2 mm). To justify this claim, we need to verify that the dimension of our laser beam waist does not influence the measured spatial profiles. The simulations by Spuler et al. [91] indicate that our expected beam waist is approximately 160-320 microns, depending on the level of mode matching achieved. Deconvoluting the broader case has an effect of only about 1% (0.02 mm) on the measured profiles, which is negligible compared to the spatial step-size. Therefore the resulting spatial resolution is about 0.2 mm.

We incorporate the electrical measurements by comparing the electron number density inferred from the CRDS ion measurements, to the electron number density from the electrical conductivity approach. To infer electron number densities from the CRDS, we need to know the fraction of positive ions that are N_2^+. At our conditions, the C-R model predicts that 96, 93, 89 and 85% of ions are N_2^+, and the remainder is N^+, for i=52, 97, 142, and 187 mA respectively. By charge balance, the sum of the N_2^+ and N^+ concentrations equals the electron number density. We convert the N_2^+ concentration profiles (found by CRDS) to electron number density profiles using these percentages. In order to determine electron number densities from the conductivity measurements (which yield the product of average electron number density with area), we assume that the shape of the electron number density profile is the same as that for the ions. The electron number densities (at the radial half-maximum) found in this way from electrical measurements are compared with those inferred from the CRDS ion measurements in Table 4. The values are plotted in Figure 75. The uncertainty in the electrical measurement (10%) is primarily from uncertainties in the momentum transfer cross-section (5%), the discharge area (4%), and the average gas temperature (8%). Column 4 of Table 4 shows that the electron number densities found from optical and electrical measurements overlap within their error bars. This excellent agreement gives us confidence in our results for the electron number density.

Table 4 Comparison of electron number densities (at the radial half-maximum) inferred by CRDS to those found by electrical measurement, for the DC discharges. The last column is the ratio of the electron number density inferred by CRDS to that found from electrical measurement.

i(mA)	$n_{e\text{-}CRDS}$ (cm^{-3})	$n_{e\text{-}Elec}$ (cm^{-3})	CRDS/Elec
52	$4.1\pm0.4 \times 10^{11}$	$3.8\pm0.4 \times 10^{11}$	1.08±0.16
97	$8.2\pm0.8 \times 10^{11}$	$7.8\pm0.8 \times 10^{11}$	1.05±0.16
142	$1.4\pm0.1 \times 10^{12}$	$1.4\pm0.1 \times 10^{12}$	0.96±0.14
187	$2.1\pm0.2 \times 10^{12}$	$2.0\pm0.2 \times 10^{12}$	1.06±0.16

7.3.2.c. Temporal Profiles of Ion Concentration and Electron Number Density.

Figure 76 shows ring-down traces obtained with and without firing the high voltage pulse, and with the laser tuned to the N_2^+ bandhead. In the absence of the high-voltage pulse (dashed line) the absorption losses are constant in time, and the signal decays as a single-exponential. In the trace with the pulse (solid line), the light decays more steeply after the pulse, reflecting an increased concentration of N_2^+. The spike in the latter trace coincides with the firing of the pulse, and is caused by RF interference generated by the pulser. To verify that we are observing changes in the N_2^+ concentration, we examine the analogous traces but with the laser detuned from the absorption band - Figure 77. These traces confirm that the only effect of the high voltage pulse on the ring-down system is to generate the interference spike. We analyze these traces to determine over what

region the interference spike affects the data. We vary the delay of the high-voltage pulse relative to the laser shot so that we can obtain ion concentrations at different times.

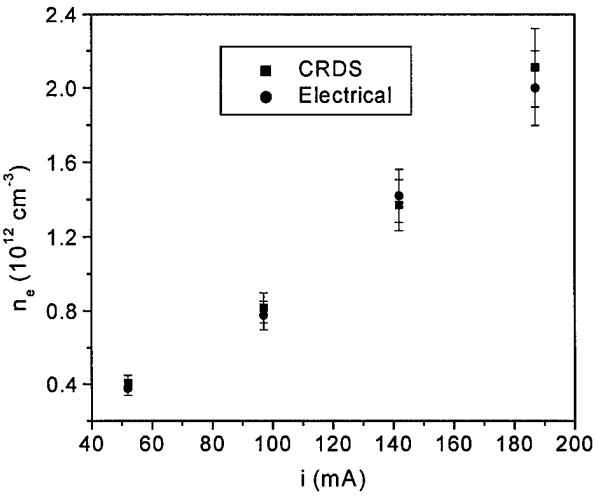

Figure 75 Electron number densities (at the radial half-maximum) as a function of discharge current. Number densities are derived from CRDS ion measurements (squares), and from electrical measurement (circles).

We quantify the time-varying N_2^+ concentration using equation (36) with a 1-μs window. This time interval represents a good compromise in making the window short compared to the time-scale of the process studied yet affording an acceptable signal-to-noise level. The empty-cavity losses (mirror reflectivity) are found from the ring-down signals with the laser detuned, and are subtracted in the analysis. Using tabulated linestrengths and the discharge dimensions, we find the absolute N_2^+ centerline concentrations as a function of time. Figure 78 presents the time varying concentrations (symbols). The error bars reflect uncertainties in the population fractions, as well as uncertainty associated with a possible change in shape of the concentration profile. The latter uncertainty is estimated by chemical kinetic considerations. One microsecond after the pulse, the N_2^+ concentration is ~1.5 x 10^{13} cm^{-3}, and then N_2^+ recombines to the DC level in about 10 μs. The DC level is found by analyzing the pulsed data at sufficiently long time delays after the pulse, and is consistent with that found in the DC plasma without the pulser.

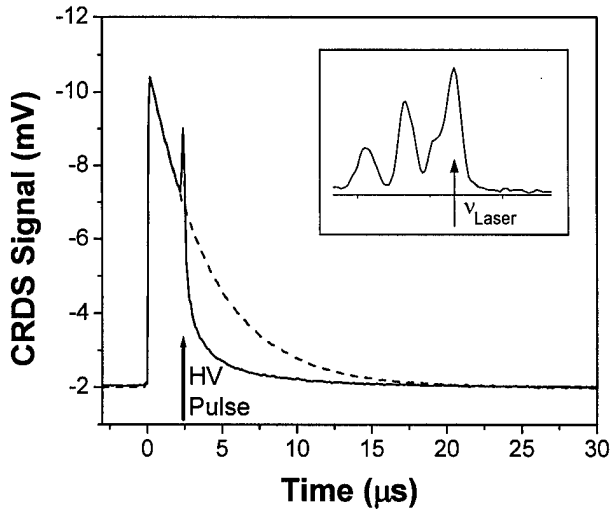

Figure 76 Experimental ring-down traces with the laser tuned to the N_2^+ absorption bandhead (inset) with the high-voltage pulse (solid line) and without the high-voltage pulse (dashed line).

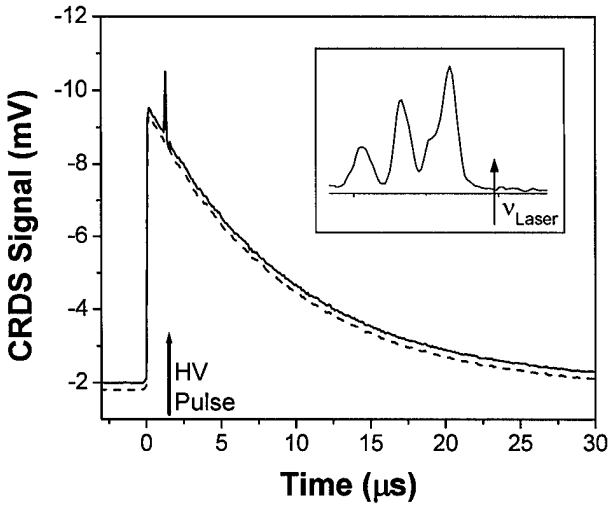

Figure 77 Experimental ring-down traces with the laser tuned away from the N_2^+ absorption (inset). We slightly scale (<5%) the amplitude of the traces for visual clarity. The detuned trace (dashed line) is offset by 0.2 mV to make it more visible.

For the pulsed discharge, we also determine the electron concentration by measuring the electrical conductivity. The temporally resolved electron concentrations are shown with a swath in Figure 78. The uncertainty in the DC electron concentration reflects uncertainties in the profile

shape, the momentum transfer cross-section, and the gas temperature. The collisional-radiative model predicts that N_2^+ is the dominant ion produced by the pulse. Thus, the agreement between the time-dependent electron and N_2^+ concentrations during plasma recombination verifies the temporally resolved CRDS measurement. The measured recombination time is consistent with reported [10] dissociative recombination rate coefficients for N_2^+ (approximately 5 x 10^{-8} cm^3/s).

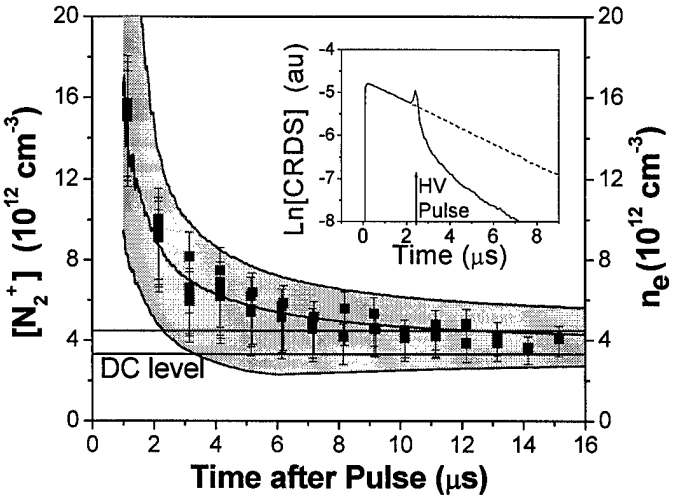

Figure 78 CRDS measurements of N_2^+ concentrations (circles) and conductivity measurements of electron densities (swath) versus time following the firing of a high-voltage pulse in an atmospheric pressure nitrogen DC plasma. The DC level of N_2^+ concentration found by CRDS is shown with a hatched bar. The inset shows the ring-down signals (plotted on a semi-log scale) with the HV pulse (solid), and without the HV pulse (dotted).

7.3.2.d. Discharge Nonequilibrium

To have a measure of the degree of non-equilibrium in the DC discharges, we examine the ratio of the measured electron number density (at the radial half-maximum) to the LTE electron number density at the corresponding gas temperature. These ratios are given in column 3 of Table 5 for the four conditions studied in the DC discharge. The measured ion and electron concentrations in the discharge are significantly higher than those corresponding to LTE conditions at the same gas temperature. The results quantify the degree of ionizational nonequilibrium in the discharges. At higher values of discharge current the LTE concentration of charged species rises steeply, so that the ratio of measured concentration to LTE concentration reduces. Related work in our laboratory has shown that by flowing the gas more quickly, comparable electron densities may be achieved with lower gas temperatures. Clearly, additional non-equilibrium is generated in the pulsed discharge. The high voltage pulse has a negligible effect on the gas temperature (and hence

corresponding LTE number density) yet the measured electron number density in the discharge increases by a factor of at least 4 immediately following the high voltage pulse.

Table 5 Ratio of the measured DC electron number density to the concentration corresponding to an LTE plasma at the same gas temperature.

i (mA)	T_g (K)	$n_{e\text{-CRDS}} / n_{e\text{-LTE}}$
52	3100	2.8×10^4
97	3600	980
142	4200	48
187	4700	5.6

7.4. NO^+ Measurements

7.4.1. Experimental Setup

7.4.1.a. RF Air Plasma

The experimental set-up is shown schematically in Figure 1. Atmospheric pressure air plasmas are generated with a 50 kW radio-frequency inductively-coupled plasma torch operating at a frequency of 4 MHz. The torch is operated with a voltage of 8.9 kV and a current of 4.6 A. The torch has been extensively characterized at similar conditions, and the plasma is known to be near LTE with a temperature of about 7000 K [1].

7.4.1.b. CRDS Measurements

Unlike the N_2^+ ion, the NO^+ ion does not have optically accessible electronic transitions. To perform CRDS measurements, the ion must be probed by accessing its infrared vibrational transitions. The strongest vibrational transitions are the fundamental bands, and for these transitions one finds that the absorbance per NO^+ ion is about 20000 times less than that of the electronic transitions of the N_2^+ ion. Figure 79 shows the modeled absorbance, as a function of wavelength, for the air plasma at the conditions used. The simulation is performed with Specair and assumes a pathlength of 5 cm, and LTE conditions at a temperature of 7000 K ($T_g=T_r=T_v=T_{electronic}=7000$ K). The simulation includes the IR absorption features of NO, OH, and NO^+. The absorption by NO and OH is relatively weak, while the various fundamental bands of NO^+ have stronger predicted absorbances.

It is evident that the NO^+ absorption begins at a wavelength of about 3950 nm, and is a maximum at about 4100 nm. Accessing these infrared wavelengths is challenging in terms of available laser sources. The current measurements have been performed using a Continuum-Mirage

OPO system. The Mirage laser is designed to operate at a maximum wavelength of 4000 nm, however we optimized the alignment in a manner that enabled operation in the vicinity of 4100 nm, in order to be nearer to the peak NO^+ absorption. Ring-down cavity alignment at these wavelengths is challenging, since the beam (and its back-reflections) are not readily observable. The ring-down cavity was aligned using a combination of LCD (liquid crystal display) paper to locate the beam, and a Helium-Neon laser to act as a reference. With the plasma off, ring-down times of about 1.2 us were obtained, corresponding to mirror reflectivities of about 0.998 (approximately an order of magnitude worse than the mirrors used for the N_2^+ experiments).

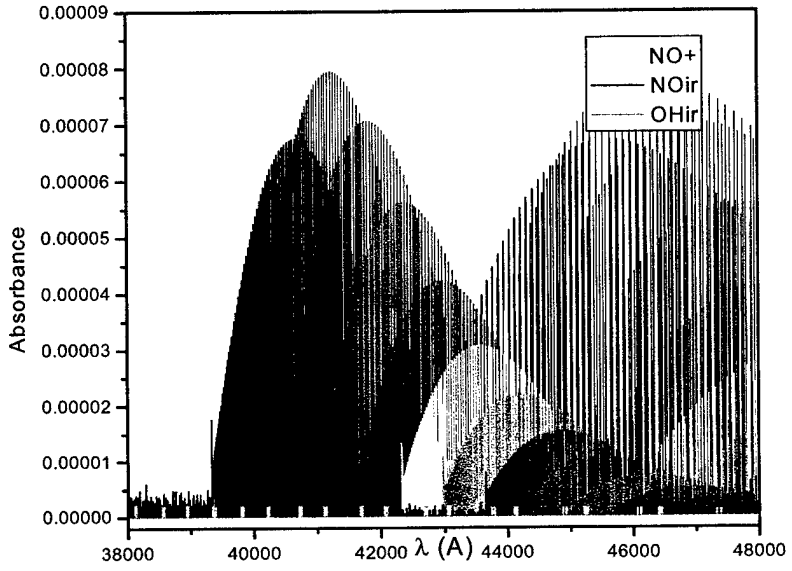

Figure 79 Modeled absorbance of the air plasma at LTE temperature of 7000 K, and path length of 5 cm. Absorption by NO, OH, and NO^+ are included. Rotationally-resolved lines of the vibrational transitions are shown.

Our initial attempts to perform CRDS measurements in the plasma torch used the same cavity-geometry as was used in the N_2^+ experiments – a g-parameter of 0.5. With the plasma off, this geometry yielded excellent stability in the ring-down times: 1% standard deviation in ring-down time for single shot ring-down signals. However, with the plasma on, the beam steering reduced the stability significantly. In the RF plasma, as compared to the smaller nitrogen plasma, the cavity-geometry considerations are different. In the smaller nitrogen plasma we wanted to simultaneously minimize the cavity beam-waist, and the beam-walk, leading to a g-parameter of –0.5 (see discussion above). On the other hand in the RF plasma, the plasma dimension (about 5 cm) is significantly larger than the beam dimension (about 1 mm). Therefore, the exact beam dimension is not critical, and the cavity-geometry may be selected solely to minimize beam-walk. The numerical modeling of Spuler et al. [91] indicate that minimizing the beam-walk may be accomplished with a g-parameter of about 0.25, which we implemented by using a cavity of length 75 cm, and mirrors of

radius-of-curvature of 1 m. This geometry did indeed reduce the beam-walk and enabled improved stability (about 2% standard deviation in empty cavity ring-down times).

As will be discussed, the identification of spectral lines in the analysis of the air plasma spectra is challenging. In order to assist in identifying NO^+ spectral features, we also collected CRDS spectra with the plasma running with argon and nitrogen (as opposed to ari), conditions that are not expected to have any significant NO^+ concentration.

7.4.2. Results and Discussion

Figure 80 shows a measured absorbance spectrum along the centerline of the air plasma. The experimental data was obtained by averaging 16 laser shots at each spectral position. The plotted CRDS data has been converted to absorbance, and fitted with a peak-fitting program. (Fitted peaks are shown in black, while raw-data is shown with blue symbols.) Also shown is the modeled NO absorbance assuming the expected plasma conditions of path length 5 cm, and LTE at 7000 K. The modeled contributions from OH and NO absorption are negligible on this scale. Comparing the CRD spectrum in the air plasma to the CRD spectrum in the argon/nitrogen plasma provides information as to line identities. The largest spectral feature (at ~4127.7 nm) is present in both spectra, and therefore is presumed to be not from NO^+. Comparing the other observed spectral features with the model does not yield good agreement. To the best of your knowledge, the spectroscopic constants used in our modeling are the most recent and accurate ones available [94]. The exact locations of the rotationally resolved lines are largely determined by the B parameter, and the quoted uncertainty on the B parameters in this work is +/- 0.005 cm^{-1} (or about 0.25%). Based on the quoted uncertainty we performed an uncertainty analysis, and found that with this level of precision it is not possible to accurately predict the locations of the rotational lines. Therefore, any match between the experimental data and model would be fortuitous. Our experimental features are repeatable (to within experimental uncertainty) and have approximately the correct integrated area, so that we do believe they are due to NO^+.

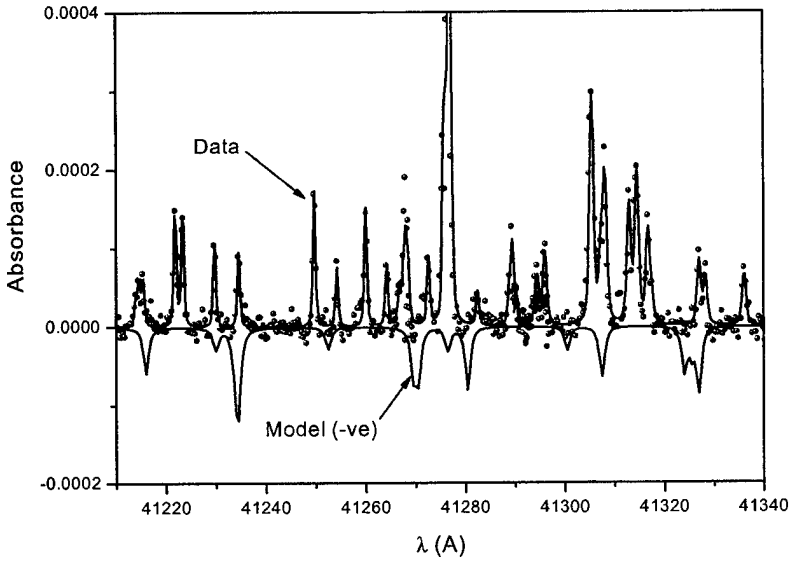

Figure 80 Experimental and modeled absorbance spectrum from the air plasma in the vicinity of 4100 nm. Raw data (blue symbols) as well as fitted peaks (top black line) are shown, as well as the modeled NO^+ lines (plotted negative for visual clarity). The precision of the spectroscopic constants used in the model is insufficient to accurately predict the location of the rotational lines.

7.5. Conclusions

Spatial and temporal profiles of N_2^+ concentration have been measured in DC and pulsed atmospheric pressure nitrogen glow discharges by cavity ring-down spectroscopy. Special care in the selection of cavity geometry is needed in the atmospheric pressure plasma environment. Sub-millimeter spatial resolution, microsecond temporal resolution, and sub-ppm concentration sensitivity have been achieved. The signal-to-noise ratio suggests a DC detection limit of about $7x10^{10}$ cm^{-3} for N_2^+ ions at our experimental conditions. Using a collisional-radiative model we infer electron number densities from the measured ion profiles. The values of electron number density found in this way are consistent with those found from spatially integrated electrical measurements. The spectroscopic technique is clearly favorable, because it offers spatial resolution and does not require knowledge of other discharge parameters. The measurements verify that the atmospheric pressure discharges studied here are two-temperature plasmas with electron number densities elevated with respect to equilibrium, which is characteristic of glow-discharge plasmas. The measurements also demonstrate the feasibility of repetitively pulsing the discharge as a means to elevate the time-averaged ionization fraction.

Measurements of the NO^+ ion in air plasmas have also been demonstrated. The accessible spectral features of NO^+ are vibrational transitions, are considerably weaker than the UV electronic

transitions used to probe N_2^+. Nevertheless, CRDS data from air plasmas was obtained, and spectral features attributed to NO^+ were observed. More precise knowledge of the spectroscopic constants of NO^+ is needed to match the experimental data with modeled spectra.

8. Summary and Conclusions

Two-temperature ($T_e > T_g$) kinetic models accounting for ionizational, chemical, vibrational and electronic nonequilibrium, and incorporating a collisional-radiative model with over 11,000 transitions have been developed to understand the mechanisms of ionizational nonequilibrium in atmospheric pressure air and nitrogen electrical discharges. These models predict that (even) at atmospheric pressure energetic electrons driven by the discharge can establish and maintain electron-density nonequilibrium of over six orders of magnitude. An unexpected result is an "S-shaped" dependence of n_e on T_e at steady-state for a given gas temperature. This behavior results from a transition between predominately molecular ions to atomic ions at a critical value of T_e and values of n_e above about 10^{14} cm^{-3}. Above this critical value of T_e, the electron density increases dramatically so that three-body recombination can maintain a steady state. Departures from a Maxwellian distribution of the free-electrons were found to have a negligible effect on the predicted steady-state characteristics, at least for the case of a nitrogen plasma.

The feasibility of such nonequilibrium discharges was demonstrated in atmospheric-pressure nitrogen and air at both room temperature and around 2000K with electrode spacing of cm scale. Stable, diffuse DC discharges have been achieved at atmospheric pressure for a range of gas flow and temperature conditions including those which produce n_e of 10^{12} to 10^{13} cm^{-3} without significant gas heating. Good agreement between theoretical and measured discharge characteristics has been obtained for both air and nitrogen discharges over a wide range of conditions including electron densities greater than 10^{12} in air and 10^{13} in nitrogen.

To reduce the power required to maintain such nonequilibrium, the finite electron recombination time (~10μs) has been exploited by means of pulsed discharges of 10 ns duration. Both single-shot and repetitively pulsed diffuse discharges at 100 kHz have been demonstrated, with power reductions of over two orders of magnitude for average electron densities greater than 10^{12} cm^{-3}. Power reductions of approximately three orders of magnitude are possible with a 1 ns repetitive pulsing technique.

A computational fluid dynamics code for the simulation of flowing nonequilibrium air plasmas including the presence of a DC discharge was developed and compared to the DC experiments conducted at Stanford University. The code uses a detailed two-temperature chemical kinetic mechanism, along with appropriate internal energy relaxation mechanisms. The discharge region was modeled by generalizing the channel model of Steenbeck, and a new semi-implicit time inte-

gration method was developed to reduce the computational cost. The results of a simplified approximate computational model are in general agreement with the experimental data. Initial simulations of the pulsed discharges have been carried out.

The CRDS technique has been used as a means to probe the population of the N_2^+ ion. CRDS allows ground state species measurements, and thus offers the most direct possible measurement of electron number density. We have performed spatially resolved measurements in a DC atmospheric pressure nitrogen discharge. We find a peak concentration of $2.6\times10^{12}/cm^3$ and a column diameter of approximately 2.2 mm, consistent with electrical measurements. We have also extended the CRDS technique to perform temporally resolved measurements appropriate for diagnostics in pulsed plasmas. Measurements of N_2^+ recombination in a pulsed nitrogen discharge have been performed with a temporal resolution of 1 microsecond. The measurements show significant ($>\sim10$) enhancement of the ionization following the pulse, and indicate that recombination occurs over about 5 microseconds. Measurements of the NO^+ ion in air plasmas have also been demonstrated. The accessible spectral features of NO^+ are vibrational transitions, are considerably weaker than the UV electronic transitions used to probe N_2^+. Nevertheless, CRDS data from air plasmas was obtained, and spectral features attributed to NO^+ were observed. This technique shows great promise for the measurement of NO^+ concentrations once more accurate spectroscopic constants of NO^+ become available.

9. Personnel

Stanford Mechanical Engineering Department

- Professor Charles H. Kruger, Vice-Provost, Dean of Research and Graduate Policy.
- Dr. Christophe O. Laux, Senior Research Scientist (Ph.D. Mechanical Engineering, Stanford University, 1993).
- Dr. Thomas G. Owano, Senior Research Scientist (Ph.D. Mechanical Engineering, Stanford University, 1991).
- Dr. Richard G. Gessman, Graduate Research Assistant (Ph.D. Mechanical Engineering, Stanford University, 1999).
- Dr. Denis M. Packan, Graduate Research Assistant (Ph.D. Mechanical Engineering,. Stanford University, 2002).
- Dr. Lan Yu, Graduate Research Assistant (Ph.D. Mechanical Engineering, Stanford University, 2001).
- Dr. Laurent Pierrot, Postdoctoral Fellow (Ph.D. Mechanical Engineering, Ecole Centrale Paris, 1997).
- Dr. Sophie Chauveau, Postdoctoral Fellow (Ph.D. Mechanical Engineering, Ecole Centrale Paris, 2001).
- Dr. J. Daniel Kelley, Visiting Scholar (since April 2001). Dr. Kelley is also a consultant to Boeing, from where he retired in March 2001.
- Dr. Zdenko Machala, Postdoctoral Fellow (Ph.D. Plasma Physics, University of Orsay, France, 2000).
- Dr. Xavier Duten, Postdoctoral Fellow (Ph.D. Plasma Physics, University of Orsay, France, 2000).
- Mr. Thomas Guillaume, Graduate Research Assistant (M.S. Ecole Polytechnique, France, 2001).
- Mr. Damien Jouvent, Graduate Research Assistant (M.S. Ecole Centrale Paris, France, 2001).
- Ms. Urvi Parekh, Undergraduate Research Assistant (B.S. Mechanical Engineering, Stanford University, Dec. 2002).
- Mr. Atukwe Newell, Undergraduate Research Assistant (B.S. Mechanical Engineering, Stanford University).

Stanford Chemistry Department

- Professor Richard N. Zare
- Dr. Azer Yalin, Postdoctoral Fellow (PhD., Mechanical Engineering, Princeton University, 2000).
- Dr. Thomas G. Spence, Postdoctoral Fellow.
- Dr. Uwe Lommatzsch, Postdoctoral Fellow (Ph.D., Department of Chemistry, Johann Wolfgang Goethe-Universitaet, Frankfurt am Main, 1998).

University of Minnesota

- Professor Graham V. Candler.
- Dr. Manoj Nagulapally, Graduate Research Assistant (Ph.D., Mechanical Engineering, University of Minnesota 2001).

- Dr. David Kolman, Postdoctoral Research Associate (Ph.D. Deparment of Mechanical Engineering, University of Minnesota, 1997)
- Dr. Camille George, Postdoctoral Research Associate (Ph.D. Department of Mechanical Engineering, University of Minnesota, 2000)
- Brian Mader, Graduate Research Assistant (B.S. Aerospace Engineering, University of Minnesota, June 2001).

Boeing-St. Louis

- Philip Smereczniak, Program Manager.

10. Refereed Publications

- Kruger, C.H., Owano, T.G., and Laux, C.O., "Experimental Investigations of Atmospheric Pressure Nonequilibrium Plasma Chemistry," *High Pressure Arcs and High Frequency Thermal Plasmas, IEEE Transactions on Plasma Science*, Vol. 25, No. 5, pp. 1042-1051, 1997.
- Kruger, C.H., Owano, T.G., Laux, C.O., and Zare, R.N., "Nonequilibrium in Thermal Plasmas," *Journal de Physique IV*, Vol. 7, pp. C4-77–C4-92, 1997.
- Pierrot, L., Laux, C.O., and Kruger, C.H., "Consistent Calculation of Electron-Impact Electronic and Vibronic Rate Coefficients in Nitrogen Plasmas," *Progress in Plasma Processing of Materials*, pp. 153-159, Begell House, Inc., NY, 1999.
- Levin, D.A., Laux, C.O, and Kruger, C.H., "A General Model for the Spectral Calculation of OH Radiation in the Ultraviolet," *Journal of Quantitative Spectroscopy and Radiative Transfer*, Vol. 61, No. 3, pp. 377-392, 1999.
- Yu, L, Pierrot, L., Laux, C.O., and Kruger, C.H., "Effects of Vibrational Nonequilibrium on the Chemistry of Two-Temperature Nitrogen Plasmas," *Plasma Chemistry and Plasma Processing*, Vol. 21, No. 4, pp. 483-503, 2001.
- Laux, C.O., Gessman, R.J., Kruger, C.H., Roux, F., Michaud, F., and Davis, S.P., "Rotational Temperature Measurements in Air and Nitrogen Plasmas Using the First Negative System of N_2^+," *Journal of Quantitative Spectroscopy and Radiative Transfer*, Vol. 68, No. 4, pp. 473-482, 2001.
- Duten, X., Packan, D., Yu, L., Laux, C.O., and Kruger, C.H., "DC and Pulsed Glow Discharges in Atmospheric Pressure Air and Nitrogen," *IEEE Transactions on Plasma Science Special Issue on "Images in Plasma Science"*, Vol. 30, No. 1, pp. 178-179, 2002.
- Yu, L., Packan, D.M., Laux, C.O., and Kruger, C.H., "Direct-Current Glow Discharges in Atmospheric Pressure Air Plasmas," *Journal of Applied Physics*, Vol. 91, No. 5, 2678-2686, 2002.
- Kruger, C.H., Laux, C.O., Yu, L., Packan, D.M., Pierrot, L., "Nonequilibrium Discharges in Air and Nitrogen Plasmas at Atmospheric Pressure," *Pure and Applied Chemistry*, Vol. 74, No. 3, pp. 337-347, 2002.
- Yalin, A.P. Laux, C.O., Kruger, C.H., and Zare, R.N., Spatial Profiles of N_2^+ Concentration in an Atmospheric Pressure Nitrogen Glow Discharge, *Plasma Sources Science and Technology*, Vol. 11, No. 3, pp. 248-253, 2002.
- Yalin, A.P., Zare, R.N, Laux, C.O., and Kruger, C.H., "Temporally Resolved Cavity Ring-Down Spectroscopy in a Pulsed Nitrogen Plasma", *Applied Physics Letters*, Vol. 81, No. 8, pp. 1408-1410, 2002.

- Laux, C.O., Kruger, C.H., Spence, T.G., and Zare, R.N., "Optical Diagnostics of Atmospheric Pressure Air Plasmas," submitted to *Plasma Sources Science and Technology*, Nov. 2001.
- Gessman, R.J., Laux, C.O., and Kruger, C.H., "Experimental Assessment of the Kinetic Mechanisms of Recombining Atmospheric Pressure Air Plasmas," submitted to *AIAA Journal*, August 2002.
- Yalin, A.P. and Zare, R.N., "Effect of Laser Lineshape on the Quantitative Analysis of Cavity Ring-Down Signals," submitted to *Laser Physics*, 2001.

11. Interactions/Transitions

11.1. Participations at meetings, conferences, seminars

- Candler, G.V., Laux, C.O., Gessman, R.J., and Kruger, C.H., "Numerical Simulation of a Nonequilibrium Nitrogen Plasma Experiment," AIAA 97-2365, 28th AIAA Plasmadynamics and Lasers Conference, Atlanta, GA, June 23-25, 1997.
- Gessman, R.J., Laux, C.O., and Kruger, C.H., "Kinetic Mechanisms of Recombining Atmospheric Pressure Air Plasmas," AIAA 97-2364, 28th AIAA Plasmadynamics and Lasers Conference, Atlanta, GA, June 23-25, 1997 (awarded 1998 Plasmadynamics and Lasers Best Technical Paper Award).
- Kruger, C.H., Owano, T.G., Laux, C.O., and Zare, R.N., "Nonequilibrium in Thermal Plasmas," Proceedings of the 23rd International Conference on Phenomena in Ionized Gases, Toulouse, France, July 17-22, 1997 (invited). Also in Journal de Physique IV, Vol. 7, pp. C4-77–C4-92, October 1997.
- Owano, T.G., Laux, C.O., and Kruger, C.H., "Experimental Investigation of Nonequilibrium Plasma Chemistry at Atmospheric Pressure," Proceedings of the 13th International Symposium on Plasma Chemistry, pp. 82-87, Beijing, China, August 18-22, 1997.
- Laux, C.O., Gessman, R.J., Owano, T.G., and Kruger, C.H., "Experimental Investigation of Nonequilibrium Plasma Chemistry at Atmospheric Pressure," 13th International Symposium on Plasma Chemistry, Beijing, China, August 18-22, 1997.
- Laux, C.O., Gessman, R.J., Packan, D.M., Yu, L., Kruger, C.H., and R.N. Zare, "Experimental Investigations of Ionizational Nonequilibrium in Atmospheric Pressure Air Plasmas," Proceedings of the 25th IEEE International Conference on Plasma Science (ICOPS), p. 302, Raleigh, NC, June 1-4, 1998 (invited).
- Schoenbach, K.H., Kunhardt, E.E., Laux, C.O., and Kruger, C.H., "Measurement of Electron Densities in Weakly Ionized Atmospheric Pressure Air," Proceedings of the 25th IEEE International Conference on Plasma Science (ICOPS),p. 283, Raleigh, NC, June 1-4, 1998.
- Nagulapally, M., Kolman, D., Candler, G.V., Laux, C.O., Gessman, R.J., and Kruger, C.H., "Simulation of Nonequilibrium Plasma Experiments," Proceedings of the 25th IEEE International Conference on Plasma Science (ICOPS), p. 303, Raleigh, NC, June 1-4, 1998.
- Spence, T.G., Paldus, B., Wahl, E.H., Aderhold, D.D., Xie, J., Owano, T.G., Laux, C.O., Kruger, C.H., and Zare, R.N., "Employing Cavity Ring-Down Spectroscopy to Probe Dilute Species in Hostile Environments," Proceedings of the 25th IEEE International Conference on Plasma Science (ICOPS), p. 122, Raleigh, NC, June 1-4, 1998.
- Nagulapally, M., Kolman, D., Candler, G.V., Laux, C.O., Gessman, R.J., and Kruger, C.H., "Numerical Simulation of a Nonequilibrium Air Plasma Experiment," AIAA Paper 98-2665, 29th AIAA Plasmadynamics and Lasers Conference, Albuquerque, NM, June 15-18, 1998.

- Pierrot, L., Laux, C.O., and Kruger, C.H., "Vibrationally-Specific Collisional-Radiative Model for Nonequilibrium Nitrogen Plasmas," AIAA 98-2664, 29th AIAA Plasmadynamics and Lasers Conference, Albuquerque, NM, June 15-18, 1998.
- Pierrot, L., Laux, C.O., and Kruger, C.H., "Consistent Calculation of Electron-Impact Electronic and Vibronic Rate Coefficients in Nitrogen Plasmas," 5th European Congress on Thermal Plasma Processes, Saint-Petersburg, Russia, July 13-16, 1998.
- Laux, C.O., "Air Plasma Research at Stanford: from Atmospheric reentry to Plasma Processing," Thermosciences Division Seminar Series, Mechanical Engineering Department, Stanford, CA, February 10, 1999.
- Laux, C.O., Yu, L., Packan, D.M., Gessman, R.J., Pierrot, L., Kruger, C.H., and Zare, R.N., "Ionization Mechanisms in Two-Temperature Air Plasmas," AIAA 99-3476, 30th AIAA Plasmadynamics and Lasers Conference, Norfolk, VA, June 28-July 1, 1999 (invited).
- Stark, R.H., Ernst, U., El-Bandrawy, M., Laux, C.O., and Schoenbach, K.H., "Direct Current Glow Discharges in Atmospheric Air," AIAA 99-3666, 30th AIAA Plasmadynamics and Lasers Conference, Norfolk, VA, June 28-July 1, 1999.
- Pierrot, L., Yu, L., Gessman, R.J., Laux, C.O., and Kruger, C.H., "Collisional-Radiative Modeling of Nonequilibrium Effects in Nitrogen Plasmas," AIAA 99-3478, 30th AIAA Plasmadynamics and Lasers Conference, Norfolk, VA, June 28-July 1, 1999.
- Spence, T.G., Xie, J., Zare, R.N., Packan, D.M., Yu, L., Laux, C.O., Owano, T.G., Kruger, C.H., "Cavity Ring-Down Spectroscopy Measurements of N_2^+ in Atmospheric Pressure Air Plasmas," AIAA 99-3433, 30th AIAA Plasmadynamics and Lasers Conference, Norfolk, VA, June 28-July 1, 1999.
- Nagulapally, M., Kolman, D., Candler, G.V., Laux, C.O., and Kruger, C.H., "Numerical Simulation of a Constant Current Density Discharge in a Flowing Air Plasma," AIAA 99-3477, 30th AIAA Plasmadynamics and Lasers Conference, Norfolk, VA, June 28-July 1, 1999.
- Yu, L, Pierrot, L., Laux, C.O., and Kruger, C.H., "Effects of Vibrational Nonequilibrium on the Chemistry of Two-Temperature Nitrogen Plasmas," Proceedings of the 14th International Symposium on Plasma Chemistry, pp. 1079-1085, Prague, Czech Republic, August 2-6, 1999.
- Candler, G.V., Nagulapally, M., Laux, C.O., and Kruger, C.H., "Numerical Simulation of a Constant Current Density Discharge in a Flowing Plasma," Gaseous Electronics Conference, Norfolk, VA, October 5-8, 1999.
- Laux, C.O., Yu, L., Packan, D.M., Pierrot, L., Kruger, C.H., and Zare, R.N., "Experimental and Theoretical Investigations of Ionization Mechanisms in Air Plasma Discharges at Atmospheric Pressure," Gaseous Electronics Conference, Norfolk, VA, October 5-8, 1999.
- Nagulapally, M, Candler, G.V., Laux, C.O., Yu, L., Packan, D., Kruger, C.H., Stark, R., Schoenbach, K.H., "Experiments and Simulations of DC and Pulsed Discharges in Air Plasmas," AIAA 2000-2417, 31st AIAA Plasmadynamics and Lasers Conference, Denver, CO, June 19-22, 2000.
- Laux, C.O., "Glow Discharges in Atmospheric Pressure Air," Gordon Research Conference on Plasma Processing Science, Tilton, NH, August 13-18, 2000 (invited).
- Laux, C.O., Packan, D.M., Yu, L., Pierrot, L., Gessman, R.J., and Kruger, C.H., "Generation of Super-ionized Diffuse Atmospheric Pressure Air Plasmas," Axcelis Inc., Rockville, MD, October 2, 2000.
- Yalin, A.P., Lommatzsch U., Zare, R.N., Laux, C.O., Kruger, C.H., "Cavity Ring-Down in Atmospheric Pressure Plasmas," Western Spectroscopy Conference, Jan 31.-Feb.2, 2001.

- Laux, C.O., Kruger, C.H., and Zare, R.N., "Diagnostics of Atmospheric Pressure Air Plasmas," Arbeitsgemeinschaft Plasmaphysik (APP) Spring Meeting, Bad Honnef, Germany, February 18-21, 2001 (invited)..
- Yalin, A.P., Lommatzsch U., Zare, R.N., Laux, C.O., Kruger, C.H., "Cavity Ring-Down Spectroscopy of N_2^+ in Pulsed and DC Atmospheric Pressure Discharges," Proceedings of the 28th IEEE International Conference on Plasma Science, p. 9, Las Vegas, NV, June 17-22, 2001.
- Nagulapally, M., Candler, G.V., Laux, C.O., Kruger, C.H., "Numerical Modeling of Repetitively Pulsed Discharges in Flowing Atmospheric Pressure Plasmas," Proceedings of the 28th IEEE International Conference on Plasma Science, p. 351, Las Vegas, NV, June 17-22, 2001.
- Yu, L., Packan, D.M., Laux, C.O., Kruger, C.H., "Direct-Current Glow Discharges in Atmospheric Pressure Air and Nitrogen Plasmas," Proceedings of the 28th IEEE International Conference on Plasma Science, p. 350, Las Vegas, NV, June 17-22, 2001.
- Kruger, C.H., Laux, C.O., Packan, D.M., Yu, L., Yalin, A.P., Zare, R.N., Nagulapally, M., Candler, G.V., Kelley, J.D., "Nonequilibrium Discharges in Atmospheric Pressure Air," Proceedings of the 28th IEEE International Conference on Plasma Science, p. 348, Las Vegas, NV, June 17-22, 2001.
- Packan, D., Yu, L., Laux, C.O., Kruger, C.H., "Repetitively Pulsed DC Glow Discharge in Atmospheric Pressure Air: Modeling and Experiments with a 12 kV, 10 ns, 100 kHz Pulse Generator," Proceedings of the 28th IEEE International Conference on Plasma Science, p. 259, Las Vegas, NV, June 17-22, 2001.
- Kruger, C.H., Laux, C.O., Yu, L., Packan, D.M., Pierrot, L., "Nonequilibrium Discharges in Air and Nitrogen Plasmas at Atmospheric Pressure," 15th International Symposium on Plasma Chemistry, Orléans, France, July 9-13, 2001 (invited).
- Laux, C.O., "DC and Pulsed Discharges in Atmospheric Pressure Air and Nitrogen Plasmas," 43rd Annual Meeting of the Division of Plasma Physics, Long Beach, CA, Oct. 29- Nov. 2, 2001. Bulletin of the American Physical Society, Vol. 46, No. 8, pp. 99-100, October 2001 (invited).
- Laux, C.O., "Air Plasma Ramparts Research," ONERA/DGA/ Industry Workshop, ONERA, Palaiseau, France, March 27, 2002 (invited).
- Kelley, J.D., Packan, D.M., Yu, L., Laux, C.O., and Kruger, C.H., "Repetitively pulsed glow discharge in atmospheric pressure air: modeling and experiments," Fourth Workshop on Magneto- and Plasma Aerodynamics for Aerospace Applications, Moscow, Russia, April 9-11, 2002.
- Laux, C.O., "Nonequilibrium Air Plasmas for Scramjet Ignition, Bio-Decontamination, and other Engineering Applications," Thermosciences Seminar Series, Stanford University, April 17, 2002.
- Laux, C.O., "Nonequilibrium Air Plasmas for Scramjet Ignition, Aerodynamic Flow Control, Bio-Decontamination, and other Engineering Applications," Joint Electrical Engineering/Mechanical Engineering Seminar, Old Dominion University, April 26, 2002.
- Chauveau, S.M., Laux, C.O., Kelley, J.D., and Kruger, C.H., "Vibrationally Specific Collisional-Radiative Model for Nonequilibrium Air Plasmas," AIAA 2002-2229, 33rd AIAA Plasmadynamics and Lasers Conference, Maui, HW, May 20-23, 2002.
- Yalin, A.P., Laux, C.O., Kruger, C.H., and Zare, R.N, "Spatially and Temporally Resolved Concentration Measurements of the N_2^+ Ion in Nitrogen Discharges by Cavity Ring-Down Spectroscopy," AIAA 2002-2245, 33rd AIAA Plasmadynamics and Lasers Conference, Maui, HW, May 20-23, 2002.

- George, C., Candler, G.V., Laux, C.O., and Kruger, C.H., "Computational Analysis of Diffuse Discharges in Atmospheric Pressure Air," AIAA 2002-2223, 33rd AIAA Plasmadynamics and Lasers Conference, Maui, HW, May 20-23, 2002.
- Laux, C.O., "Radiation and Nonequilibrium Collisional-Radiative Models," von Karman Institute Special Course on Physico-Chemical Modeling of High Enthalpy and Plasma Flows, Rhode-Saint-Genèse, Belgium, June 4-7, 2002 (invited).
- Machala, Z., Laux, C.O., and Kruger, C.H., "Nonequilibrium Microwave and DC-Discharge Plasmas in Atmospheric Pressure Air," poster presented at the Gordon Research Conference on Plasma Processing Science, Tilton, NH, July 21-26, 2002.
- Yalin, A.P., Machala, Z., Laux, C.O., Kruger, C.H., and Zare, R.N., "Optical Emission and Cavity Ring-Down Spectroscopy Measurements in Atmospheric Pressure Nitrogen Glow Discharge," poster presented at the Gordon Research Conference on Plasma Processing Science, Tilton, NH, July 21-26, 2002.
- Yalin, A.P., Laux, C.O., Kruger, C.H., and Zare, R.N., "Temporally and Spatially Resolved Cavity Ring-Down Spectroscopy Measurements in Atmospheric Pressure Plasmas," OSA Annual Meeting and Exhibit 2002 and Laser Science XVIII, Orlando, FL, Sept. 29- Oct.3, 2002.
- Laux, C.O., Machala, Z., Duten, X., Packan, D.M., Yu, L., Kruger, C.H., "Scaled-up Nonequilibrium Air Plasmas," to be presented at the 5th Weakly Ionized Gases AIAA Workshop, Reno, NV, January 6-9 2003.
- Chauveau, S.M., Kelley, J.D., Laux, C.O., Kruger, C.H., "Vibrationally Specific Collisional-Radiative Model for Nonequilibrium Air Plasmas," to be presented at the 41st AIAA Aerospace Sciences Meeting and Exhibit, Reno, NV, January 6-9, 2003.

11.2. Consultative and Advisory Functions to Other Laboratories and Agencies

- Prof. Candler currently serves on the DoE/Sandia ASCI Advisory Panel. He is a member of the NATO Research Technology Organization, Working group 10, Technologies for Hypersonic Flight. He also serves on the Thermophysics committee of the American Institute of Aeronautics and Astronautics.
- Dr. Laux serves on the Plasmadynamics and Lasers Committee of the American Institute of Aeronautics and Astronautics.

12. New Discoveries, Inventions, or Patent Disclosures

None

13. Honors/Awards

Prof. C.H. Kruger's group:

- 1997 Invited Plenary Lecture: Kruger, C.H., Owano, T.G., Laux, C.O., "Nonequilibrium Plasmas and Diagnostics," 23rd International Conference on Phenomena in Ionized Gases, Toulouse, France, July 17-22, 1997.

- 1998 Invited Lecture: Laux, C.O., Gessman, R.J., Packan, D.M., Yu, L., Kruger, C.H., and R.N. Zare, "Experimental Investigations of Ionizational Nonequilibrium in Atmospheric Pressure Air Plasmas," 25th IEEE International Conference on Plasma Science (ICOPS), Raleigh, NC, June 1-4, 1998.
- 1998 Best Paper Award, AIAA Plasmadynamics and Lasers: Gessman, R.J., Laux, C.O., and Kruger, C.H, "Experimental Study of Kinetic Mechanisms of Recombining Atmospheric Pressure Air Plasmas," award presented at the 29th AIAA Plasmadynamics and Lasers Conference, Albuquerque, NM, June 1998.
- 1999 Invited Lecture: Laux, C.O., Yu, L., Packan, D.M., Gessman, R.J., Pierrot, L., Kruger, C.H., and Zare, R.N., "Ionization Mechanisms in Two-Temperature Air Plasmas," *AIAA 99-3476*, 30th AIAA Plasmadynamics and Lasers Conference, Norfolk, VA, June 28-July 1, 1999.
- 2000 Invited Lecture: Laux, C.O., "Glow Discharges in Atmospheric Pressure Air," Gordon Research Conference on Plasma Processing Science, Tilton, NH, August 13-18, 2000.
- 2001 Invited Plenary Lecture: Laux, C.O., Kruger, C.H., and Zare, R.N., "Diagnostics of Atmospheric Pressure Air Plasmas," Arbeitsgemeinschaft Plasma Physik (APP) Spring Meeting, Bad Honnef, Germany, February 18-21, 2001.
- 2001 Invited Plenary Lecture: Kruger, C.H., Laux, C.O., Yu, L., Packan, D.M., Pierrot, L., "Nonequilibrium Discharges in Air and Nitrogen Plasmas at Atmospheric Pressure," 15th International Symposium on Plasma Chemistry, Orléans, France, July 9-13, 2001.
- 2001 Invited Lecture: Laux, C.O., "DC and Pulsed Discharges in Atmospheric Pressure Air and Nitrogen Plasmas," 43rd Annual Meeting of the Division of Plasma Physics, Long Beach, CA, Oct. 29- Nov. 2, 2001. Bulletin of the American Physical Society, Vol. 46, No. 8, pp. 99-100, October 2001.
- 2002 Invited Special Course: Laux, C.O., "Radiation and Nonequilibrium Collisional-Radiative Models," von Karman Institute Special Course on Physico-Chemical Modeling of High Enthalpy and Plasma Flows, Rhode-Saint-Genèse, Belgium, June 4-7, 2002.

Prof. R.N. Zare:

- 1997 Eastern Analytical Symposium Award for Outstanding Achievements in the Field of Analytical Chemistry.
- 1997 California Scientist of the Year.
- 1997 NASA Exceptional Scientific Achievement Award.
- 1997 Fischer Award in Analytical Chemistry given by the American Chemical Society.
- Allan V. Cox Medal for Faculty Excellence Fostering Undergraduate Research, Stanford University, 1998.
- ACS Award in Analytical Chemistry, 1998.
- Centennial Medal, Graduate School of Arts and Sciences, Harvard University, 1998.
- E.B. Wilson Award in Spectroscopy, American Chemical Society, 1999.
- Honorary Doctor of Science, Columbia University, 1999.
- The Welch Award in Chemistry, 1999.
- Doctor of Philosophy, *honoris causa*, Uppsala University, 2000.
- Arthur L. Schawlow Prize in Laser Science, American Physical Society, 2000.
- Nobel Laureate Signature Award for Graduate Education, American Chemical Society, 2000.

- Charles Lathrop Parsons Award, American Chemical Society, 2001, "to recognize outstanding public service by a member of the American Chemical Society."
- Faraday Medal & Lectureship, Royal Society of Chemistry, 2001.
- 2000-2001 Madison Marshall Award, American Chemical Society, North Alabama, 2001.
- Honorary Doctorate, State University of West Georgia, 2001.
- Honorary Doctorate, *D Univ*, The University of York, 2001.
- 2000-2001 CaSSS (California Separation Science Society) Scientific Achievement Award, 2002.
- Distinguished Chemist Award, American Chemical Society Sierra Nevada Section, 2002.

Prof. G.V. Candler's group:

- 1998 Invited Plenary Paper: Candler, G.V., "High Enthalpy Flow Simulation Challenges," 29th AIAA Plasmadynamics and Lasers Conference, Albuquerque, NM, June 1998.
- 1999 Invited Paper: Candler, G. V. and Kelley, J. D., "Supersonic Flow of Discharge-Excited Air Around Blunt Bodies," Workshop on Perspectives of MHD and Plasma Technologies in Aerospace Applications, Moscow, Russia, March 24-25, 1999.
- 1999 Invited paper: Campbell, C.H., and G.V. Candler, "Detailed Simulation of Nitrogen Dissociation in Shock Waves," 33rd AIAA Thermophysics Conference, Norfolk, VA, June 1999.
- 2001 Best Student Paper Award, AIAA Thermophysics Committee.
- 2002 George Taylor Distinguished Research Award: Candler, G.V.

Dr. J. D. Kelley:

- September 1998: named a Boeing Technical Fellow.
- 1999 Invited Paper: Candler, G. V. and Kelley, J. D., "Supersonic Flow of Discharge-Excited Air Around Blunt Bodies," Workshop on Perspectives of MHD and Plasma Technologies in Aerospace Applications, Moscow, Russia, March 24-25, 1999.

14. References

[1] C. O. Laux, "Optical Diagnostics and Radiative Emission of Air Plasmas," Ph.D. Thesis, *Mechanical Engineering*. Stanford, CA: Stanford University, 1993.

[2] L. Pierrot, C. O. Laux, and C. H. Kruger, "Vibrationally-Specific Collisional-Radiative Model for Nonequilibrium Nitrogen Plasmas," *AIAA 98-2664*, 29th AIAA Plasmadynamics and Lasers Conference, Albuquerque, NM, 1998.

[3] L. Pierrot, C. O. Laux, and C. H. Kruger, "Consistent Calculation of Electron-Impact Electronic and Vibrational Rate Coefficients in Nitrogen Plasmas," 5th International Thermal Plasma Processing Conference, St.-Petersburg, Russia, 1998.

[4] L. Yu, L. Pierrot, C. O. Laux, and C. H. Kruger, "Effects of vibrational nonequilibrium on the chemistry of two-temperature nitrogen plasmas," 14th International Symposium on Plasma Chemistry, Prague, Czech Republic, 1999.

[5] L. Pierrot, L. Yu, R. J. Gessman, C. O. Laux, and C. H. Kruger, "Collisional-radiative modeling of nonequilibrium effects in nitrogen plasmas," *AIAA 99-3478*, 30th AIAA Plasmadynamics and Lasers Conference, Norfolk, VA, 1999.

[6] L. Yu, L. Pierrot, C. O. Laux, and C. H. Kruger, "Effects of Vibrational Nonequilibrium on the Chemistry of Two-Temperature Nitrogen Plasmas," *Plasma Chemistry and Plasma Processing*, vol. 21, pp. 483-503, 2001.

[7] M. A. Lieberman and A. J. Lichtenberg, *Principles of Plasma Discharges and Materials Processing*. New York: John Wiley & Sons, 1994.

[8] P. M. Hierl, I. Dotan, J. V. Seeley, J. M. Van Doren, R. A. Morris, and A. A. Viggiano, "Rate Constants for the Reaction of O+ with N2 and O2 as a Function of Temperature (300-1800 K)," *J. Chem. Phys.*, vol. 106, pp. 3540-3544, 1997.

[9] I. Dotan and A. A. Viggiano, "Rate Constants for the Reaction of O^+ with NO as a function of Temperature (300-1400 K)," *J. Chem. Phys.*, vol. 110, pp. 4730-4733, 1999.

[10] C. Park, *Nonequilibrium Hypersonic Aerothermodynamics*. New York: Wiley, 1989.

[11] C. Park, "Review of Chemical-Kinetic Problems of Future NASA Missions, I: Earth Entries," *Journal of Thermophysics and Heat Transfer*, vol. 7, pp. 385-398, 1993.

[12] R. J. Kee, F. M. Rupley, and J. A. Miller, "Chemkin-II: A Fortran Chemical Kinetics Package for the Analysis of Gas Phase Chemical Kinetics," Sandia National Laboratories, Livermore, CA, Report SAND89-8009, 1989.

[13] C. O. Laux, L. Yu, D. M. Packan, R. J. Gessman, L. Pierrot, C. H. Kruger, and R. N. Zare, "Ionization Mechanisms in Two-Temperature Air Plasmas," *AIAA 99-3476*, 30th AIAA Plasmadynamics and Lasers Conference, Norfolk, VA, 1999.

[14] S. C. Brown, *Basic Data of Plasma Physics*: The M.I.T. Press, 1966.

[15] I. P. Shkarofsky, T. W. Johnston, and M. P. Bachynski, *The Particle Kinetics of Plasmas*: Addison-Wesley Pub. CO., 1966.

[16] W. Tsang and J. T. Herron, "Chemical kinetic data base for propellant combustion. I. Reactions involving NO, NO_2, HNO, HNO_2, HCN and N_2O," *Journal of Physical and Chemical Reference Data*, vol. 20, pp. 609-663, 1991.

[17] M. Mitchner and C. H. Kruger, *Partially Ionized Gases*. New York: John Wiley & Sons, Inc., 1973.

[18] L. Pierrot, "Chemical Kinetics and Vibrationally-Specific Collisional-Radiative Models for Nonequilibrium Nitrogen Plasmas," Stanford University - Thermosciences Division 1999.

[19] S. M. Chauveau, C. O. Laux, J. D. Kelley, and C. H. Kruger, "Vibrationally Specific Collisional-Radiative Model for Nonequilibrium Air Plasmas," *AIAA 2002-2229*, 33rd AIAA Plasmadynamics and Lasers Conference, Maui, HW, 2002.

[20] Y. K. Kazansky and I. S. Yelets, "The Semiclassical Approximation in the Local Theory of Resonance Inelastic Interaction of Slow Electrons with Molecules," *J. Phys. B*, vol. 17, pp. 4767-4783, 1984.

[21] P. V. Kozlov, V. N. Makarov, V. A. Pavlov, A. V. Uvarov, and O. P. Shatalov, "Use of CARS spectroscopy to study excitation and deactivation of nitrogen molecular vibrations in a supersonic gas stream," *Tech. Phys.*, vol. 41, pp. 882-889, 1996.

[22] W. D. Breshears and P. F. Bird, "Effect of oxygen atoms on the vibrational relaxation of nitrogen," *J. Chem. Phys.*, vol. 48, pp. 4768-4773, 1968.
[23] R. J. McNeal, M. E. J. Whitson, and G. R. Cook, "Quenching of vibrationally excited N_2 by atomic oxygen," *Chem. Phys. Lett.*, vol. 16, pp. 507-510, 1972.
[24] D. J. Eckstrom, "Vibrational relaxation of shock-heated N_2 by atomic oxygen using the ir tracer method," *J. Chem. Phys.*, vol. 59, pp. 2787-2795, 1973.
[25] R. L. Taylor, *Chemical Kinetics Data Survey. VII. Tables of Rate and Photochemical Data for Modeling of the Stratosphere*, 1974.
[26] S. J. Lukasik and J. E. Young, "Vibrational relaxation times in nitrogen," *J. Chem. Phys.*, vol. 27, pp. 1149-1155, 1957.
[27] M. C. Henderson, *J. Acoust. Soc. Amer.*, vol. 34, pp. 349, 1962.
[28] R. C. Millikan and D. R. White, "Systematics of Vibrational Relaxation," *J. Chem. Phys.*, vol. 39, pp. 3209-3213, 1963.
[29] I. R. Hurle, "The thermal energy transfer between free electrons and molecular vibration," *J. Chem. Phys.*, vol. 41, pp. 3592-3603, 1964.
[30] I. R. Hurle, "Line-reversal studies of the sodium excitation process behind shock waves in N_2," *J. Chem. Phys.*, vol. 41, pp. 3911-3920, 1964.
[31] J. P. Appleton, *J. Chem. Phys.*, vol. 47, pp. 3231, 1967.
[32] M. A. Kovacs and M. E. Mack, "Vibrational relaxation measurements using 'transient' stimulated Raman scattering," *Appl. Phys. Lett.*, vol. 20, pp. 487-490, 1972.
[33] E. E. Nikitin, A. I. Osipov, and S. Y. Umanskii, "Vibrational-translational energy exchange in collisions of homonuclear diatomic molecules," in *Reviews of plasma chemistry*, Smirnov, Ed. New York, London: Consultants Bureau, 1994, pp. 1.
[34] K. N. C. Bray, "Vibrational relaxation of anharmonic oscillator molecules: relaxation under isothermal conditions," *J. Phys. B. (Proc. Phys. Soc.)*, vol. 1, pp. 705-717, 1968.
[35] J. Keck and G. Carrier, "Diffusion theory of nonequilibrium dissociation and recombination," *J. Chem. Phys.*, vol. 43, pp. 2284-2298, 1965.
[36] V. B. Podobedov, 1979, . *Multichannel velocity method for recording weak optical spectra and its application to spectroscopy*. Troitsk: Institute of spectroscopy. Academy of sciences of the USSR, 1979.
[37] S. I. Valyanskii, K. A. Vereshchagin, A. Y. Volkov, P. P. Pashinin, V. V. Smirnov, V. I. Fabelinskii, and L. Holtz, "Determination of the rate constant for vibrational-vibrational exchange in nitrogen under biharmonic excitation conditions," *Soviet Journal of Quantum Electronics*, vol. 14, pp. 1229-1231, 1984.
[38] S. I. Valyanskii, K. A. Vereshchagin, W. Wernke, A. Y. Volkov, P. P. Pashinin, V. V. Smirnov, V. I. Fabelinskii, and P. L. Tshapovskii, "Studies of the kinetics of the vibrational and rotational distribution functions of nitrogen excited by a pulsed discharge," *Soviet Journal of Quantum Electronics*, vol. 14, pp. 1226-1228, 1984.
[39] A. F. Suchkov and Y. N. Shebeko, "Kinetics of vibrational exchange in nonequilibrium nitrogen. A comparison of theory and experiment," *High Energy Chemistry (English translation of Khimiya Vysokikh Energii)*, vol. 15, pp. 213-216, 1981.
[40] Y. S. Akishev, A. V. Demyanov, I. V. Kochetov, A. P. Napartovich, S. V. Pashkin, V. V. Ponomarenko, V. G. Pevgov, and V. B. Podobedov, "Determination of vibrational exchange constants in N_2 from heating of gas," *High Temperature*, vol. 20, pp. 658-666, 1982.
[41] O. A. Gordeev and V. A. Shakhatov, "Determination of the Rate Constants for VV Exchange in a Nitrogen Glow Discharge by CARS Spectroscopy," *Tech. Phys.*, vol. 40, pp. 656-661, 1995.
[42] G. D. Billing and E. R. Fischer, "VV and VT Rate Coefficients in N2 by a Quantum-Classical Model," *Chemical Physics*, vol. 43, pp. 395-401, 1979.
[43] A. V. Bogdanov, Y. N. Zhuk, K. S. Klopovskii, and V. A. Pavlov, "Quasiclassical Calculation of Cross Sections and Rate Constants for VRT-Exchang in Diatomic Molecules," *Soviet Physics: Technical Physics*, vol. 35, pp. 145-149, 1990.
[44] A. S. Kirillov, "Rates of plasma-chemical processes involving vibrationally-excited molecules," *Cosmic Research*, vol. 35, pp. 144-152, 1997.

[45] A. S. Kirillov, "The calculation of TV, VT, VV, VV'- rate coefficients for the collisions of the main atmospheric components," *Annales Geophysicae*, vol. 16, pp. 838-846, 1998.
[46] W. Q. Jeffers and J. D. Kelley, "Calculation of VV transfer probabilities in CO-CO collisions," *J. Chem. Phys.*, vol. 55, pp. 4433-4437, 1971.
[47] D. R. White and R. C. Millikan, "Vibrational relaxation in air," *AIAA Journal*, vol. 2, pp. 1844-1846, 1964.
[48] D. R. White, "Shock-tube study of vibrational exchange in N_2-O_2 mixtures," *J. Chem. Phys.*, vol. 49, pp. 5472-5476, 1968.
[49] H.-J. Bauer and N. Roesler, in *Molecular Relaxation Processes*, vol. 20. London: The Chemical Society, Burlington House, 1966, pp. 245-252.
[50] G. J. Wilson, M. L. Turnidge, and C. J. S. M. Simpson, "Nonresonant (VV) transfer between molecules dissolved in liquid N_2, liquid Ar, and liquid N_2/Ar mixtures," *J. Chem. Phys.*, vol. 102, pp. 4093-4100, 1995.
[51] A. B. Callear, "Vibrational relaxation of nitric oxide," *Disc. Faraday Soc.*, vol. 33, pp. 28-36, 1962.
[52] R. L. Taylor, M. Camac, and R. M. Feinberg, "Measurements of vibration-vibration coupling in gas mixtures," 11th International Symposium on Combustion, 1967.
[53] J. C. Stephenson, "Vibrational relaxation of NO $X^2\Pi(v=1)$ in the temperature range 100-300 K," *J. Chem. Phys.*, vol. 60, pp. 4289-4294, 1974.
[54] L. Doyennette and M. Margottin-Maclou, "Vibrational relaxation of NO(v=1) by NO, N2, CO, HCl, CO2, and N2O from 300 to 600K," *J. Chem. Phys.*, vol. 84, pp. 6668-6678, 1986.
[55] M. Nagulapally, G. V. Candler, C. O. Laux, L. Yu, D. M. Packan, C. H. Kruger, R. Stark, and K. H. Schoenbach, "Experiments and simulations of DC and Pulsed Discharges in Air Plasmas," 31st AIAA Plasmadynamics and Lasers Conference, Denver, CO, 2000.
[56] D. A. Levin, C. O. Laux, and C. H. Kruger, "A General Model for the Spectral Radiation Calculation of OH in the Ultraviolet," *JQSRT*, vol. 61, pp. 377-392, 1999.
[57] L. Yu, "Nonequilibrium Effects in Two-Temperature Atmospheric Pressure Air and Nitrogen Plasmas," Ph.D. Thesis *Mechanical Engineering*. Stanford, CA: Stanford University, 2001.
[58] Y. P. Raizer, *Gas Discharge Physics*. Berlin: Springer, 1991.
[59] H. Thoma and L. Heer, *Z. Tech. Phys. (Leipzig)*, vol. 13, pp. 464, 1932.
[60] W. A. Gambling and H. Edels, "The High-Pressure Glow Discharge in Air," *British Journal of Applied Physics*, vol. 5, pp. 36-39, 1953.
[61] A. Von Engel, *Ionized Gases*. Oxford: Oxford University Press, 1965.
[62] R. H. Stark and K. H. Schoenbach, *Appl. Phys. Lett.*, vol. 74, pp. in press, 1999.
[63] R. H. Stark and K. H. Schoenbach, "Direct current high-pressure glow discharges," *J. Appl. Phys.*, vol. 85, pp. 2075-2080, 1999.
[64] F. Leipold, R. H. Stark, A. El-Habachi, and K. H. Schoenbach, "Electron density measurements in an atmospheric pressure air plasma by means of infrared heterodyne interferometry," *J. Phys. D.*, vol. 33, pp. 2268-2273, 2000.
[65] M. Nagulapally, G. V. Candler, C. O. Laux, L. Yu, D. Packan, C. H. Kruger, R. Stark, and K. H. Schoenbach, "Experiments and Simulations of DC and Pulsed Discharges in Air Plasmas," *AIAA 2000-2417*, 31st AIAA Plasmadynamics and Lasers Conference, Denver, CO, 2000.
[66] D. M. Packan, "Repetitively Pulsed Glow Discharge in Atmospheric Pressure Air," Ph.D. Thesis, *Mechanical Engineering*. Stanford, CA: Stanford University, 2002.
[67] S. Gordon and B. J. Mc. Bride, "Computer Program for Calculation of Complex Chemical Equilibrium Compositions, Rocket Performance, Incident and Reflected Shocks, and Chapman-Jouguet Detonations," NASA SP-273, 1971.
[68] P. A. Gnoffo, R. N. Gupta, and J. L. Shinn, "Conservation Equations and Physical Models for Hypersonic Air Flows In Thermal and Chemical Nonequilibrium," NASA TP-2867, 1989.

[69] F. G. Blottner, M. Johnson, and M. Ellis, "Chemically Reacting Viscous Flow Program for Multi-Component Gas Mixtures," Sandia Laboratories, Albuquerque, NM SC-RR-70-754, Dec. 1971 1971.

[70] R. N. Gupta, J. M. Yos, R. A. Thompson, and K.-P. Lee, "A Review of Reaction Rates and Thermodynamic and Transport Properties for an 11-Species Air Model for Chemical and Thermal Nonequilibrium Calculations to 30,000 K," NASA RP-1232, August 1990 1990.

[71] S. S. Lee, D. W. Minsek, D. J. Vestyck, and P. Chen, "Growth of diamond from atomic hydrogen and a supersonic free jet of methyl radicals," *Science*, vol. 263, pp. 1596-8, 1994.

[72] R. D. Ramshaw, "Self-Consistent Effective Binary Diffusion in Multicomponent Gas Mixtures," *J. Nonequilibrium Thermodynamics*, vol. 15, pp. 295-300, 1990.

[73] Y. P. Raizer, "Gas Discharge Physics." New York: Springer, 1991, pp. 278-279.

[74] M. Nagullapally, "Modeling of Discharges in Flowing Plasmas," in *Aerospace Engineering and Mechanics*. Minneapolis, MN: University of Minnesota, 2001.

[75] G. V. Candler and R. W. MacCormack, "The Computation of Hypersonic Ionized Flows in Chemical and Thermal Nonequilibrium," *J. Thermophysics Heat Transfer*, vol. 5, pp. 266-273, 1991.

[76] M. Nagulapally, D. Kolman, G. V. Candler, C. O. Laux, R. J. Gessman, and C. H. Kruger, "Numerical Simulation of Nonequilibrium Nitrogen and Air Plasma Experiments," *AIAA 98-2665*, 29th AIAA Plasmadynamics and Lasers Conference, 1998.

[77] P.-C. Huang, "A Turbulent Swirling Arc Model and a Two-Fluid Turbulence Model for Thermal Plasma Sprays," University of Minnesota, 1993.

[78] E. Quandt, I. Kraemer, and H. F. Dobele, "Measurements of Negative-Ion Densities by Cavity Ringdown Spectroscopy," *Europhysics Letters*, vol. 45, pp. 32-37, 1999.

[79] F. Grangeon, C. Monard, J.-L. Dorier, A. A. Howling, C. Hollenstein, D. Romanini, and N. Sadeghi, "Applications of the Cavity Ring-Down Technique to a Large-Area RF-Plasma Reactor," *Plasma Sources Science and Technology*, vol. 8, pp. 448-456, 1999.

[80] W. M. M. Kessels, A. Leroux, M. G. H. Boogaarts, J. P. M. Hoefnagels, M. C. M. van de Sanden, and D. C. Schram, "Cavity ring down detection of SiH_3 in a remote SiH_4 plasma and comparison with model calculations and mass spectrometry," *J. Vac. Sci. Technol. A*, vol. 19, pp. 467-476, 2001.

[81] A. Schwabedissen, A. Brockhaus, A. Georg, and J. Engemann, "Determination of the gas-phase Si atom density in radio frequency discharges by means of cavity ring-down spectroscopy," *J. Phys. D-Appl. Phys*, vol. 34, pp. 1116-1121, 2001.

[82] J. P. Booth, G. Cunge, L. Biennier, D. Romanini, and A. Kachanov, "Ultraviolet cavity ring-down spectroscopy of free radicals in etching plasmas," *Chem. Phys. Lett.*, vol. 317, pp. 631-636, 2000.

[83] M. Aldener, B. Lindgren, A. Pettersson, and U. Sassenberg, "Cavity Ringdown Laser Absorption Spectroscopy : Nitrogen cation," *Physica Scripta*, vol. 61, pp. 62-65, 2000.

[84] M. Kotterer, J. Conceicao, and J. P. Maier, "Cavity ringdown spectroscopy of molecular ions: A $^2\Pi_u$<–X $^2\Sigma_g^+$ (6-0) transition of N_2^+," *Chem. Phys. Lett.*, vol. 259, pp. 233-236, 1996.

[85] K. W. Busch and A. M. Busch, "Cavity-Ringdown Spectroscopy," *720*, ACS Symposium Series, 1999.

[86] G. Berden, R. Peeters, and G. Meijer, "Cavity Ring-Down Spectroscopy: Experimental Schemes and Applications," *Int. Reviews in Physical Chemistry*, vol. 19, pp. 565-607, 2000.

[87] P. Zalicki and R. N. Zare, "Cavity ring-down spectroscopy for quantitative absorption measurements," *Journal of Chemical Physics*, vol. 102, pp. 2708-17, 1995.

[88] A. P. Yalin and R. N. Zare, "Effect of Laser Lineshape on the Quantitative Analysis of Cavity Ring-Down Signals," *in press, Laser Physics*, 2002.

[89] S. S. Brown, A. R. Ravishankra, and H. Stark, "Simultaneous Kinetics and Ring-Down: Rate Coefficients from Single Cavity Loss Temporal Profiles," *J. Chem. Phys. A*, vol. 104, pp. 7044-7052, 2000.

[90] A. E. Siegman, *Lasers*. Mill Valley: University Science Books, 1986.

[91] S. Spuler and M. Linne, "Numerical analysis of beam propagation in pulsed cavity ring-down spectroscopy," *Appl. Optics*, vol. 41, pp. 2858-2868, 2002.

[92] F. Michaud, F. Roux, S. P. Davis, A.-D. Nguyen, and C. O. Laux, "High resolution Fourier spectrometry of the $^{14}N_2^+$ ion," *J. Molec. Spectrosc.*, vol. 203, pp. 1-8, 2000.

[93] C. O. Laux, R. J. Gessman, C. H. Kruger, F. Roux, F. Michaud, and S. P. Davis, "Rotational Temperature Measurements in Air and Nitrogen Plasmas Using the First Negative System of N_2^+," *JQSRT*, vol. 68, pp. 473-482, 2001.

[94] G. K. Jarvis, M. Evans, C. Y. Ng, and K. Mitsuke, "Rotational-resolved pulsed field ionization photoelectron study of NO^+ ($X^1\Sigma^+$, v^+=0-32) in the energy range of 9.24-16.80 eV.," *JCP*, vol. 111, pp. 3058-3069, 1999.